# Doctoral Dissertation

## Study on Laser-driven Neutron Source and its application to a single-shot and compact resonance spectroscopy

Zechen Lan

December 2023

Graduate School of Engineering,
Osaka University

# *Acknowledgements*

In this section I want to acknowledge all peoples without whom this thesis would never happens. I received a lot of support from many people in the Osaka Univ., Hokkaido Univ., Japan Atomic Energy Agency, Queen's Univ. Belfast and Tokamak Energy Ltd, which significantly improved the quality of current work and helped me with ideas of development and experiment performance.

First of all I would like to express my appreciation to my scientific advisor, Prof. A. Yogo, for his careful guidance of my research in the past three years, which greatly improved my understanding in a wide field of my study and research.

I am grateful to Prof. T. Hirose, Prof. M. Katayama, Prof. R. Katayama, Prof. K. Kojima, Prof. M. Kondow, Prof. M. Maruyama, Prof. N. Mori, Prof. Y. Mori, Prof. A. Oiwa, Prof. M. Ozaki, Prof. M. Tonouchi and Prof. J. Yamazaki for their guidance doctoral thesis review. And I would like to express my sincere thanks to Prof. K. Yamamoto, Prof. Y. Arikawa, Dr. Y.Abe, Prof. S. Fujioka and Prof. R. Kodama of Osaka Univ., Prof. T. Hayakawa of National Institutes for Quantum Science and Technology, Prof. T. Kamiyama and Prof. H. Sato of Hokkaido Univ., Prof. M. Koizumi, Dr. F. Ito, Dr. J. Lee, Dr. T. Takahashi and Dr. K. Hironaka of Japan Atomic Energy Agency, Prof. S. Kar of Queen's Univ. Belfast, Dr. S. R. Mirfayzi of Tokamak Energy Ltd for their selfless help in experiments and research. Also, I want to thank Mr. T. Wei, Mr. Y. Tatsumi, Mr. R. Yamada and other NP group members who have provided a lot of support and happiness in my daily life and research.

Finally, I want to thank my family for their selfless supports and loving considerations, which have been giving me great confidence all through these years. Thanks to everyone who have helped me in my scientific research during my doctoral course. This thesis can not be accomplished without any of you.

# Contents

**Acknowledgements** **iii**

**1 Introduction** **1**

1.1 Neutron resonance spectroscopy . . . . . 1

1.1.1 Neutron . . . . . 1

1.1.2 Background of neutron resonance spectroscopy . . . . . 2

1.1.3 Physics and methods of neutron resonance spectroscopy 4

Neutron-matter interactions . . . . . 4

Cross section . . . . . 5

Neutron resonance absorption . . . . . 8

1.1.4 Time-of-flight method for neutron detection . . . . . 10

1.1.5 Applications of neutron resonance spectroscopy . . . . . 12

1.2 Laser-driven Neutron Source . . . . . 13

1.2.1 Background of Laser-driven Neutron Source . . . . . 13

1.2.2 Applications of Laser-driven Neutron Source and comparison with other neutron sources . . . . . 14

1.3 The main topic of this work . . . . . 16

**2 Development of Short-Pulse Laser-driven Neutrons** **17**

2.1 Laser-driven ion acceleration . . . . . 17

2.1.1 Relativistic plasma generation using high-intensity laser beam . . . . . 17

2.1.2 Electron heating by laser-plasma interaction . . . . . 20

Inverse bremsstrahlung absorption . . . . . 20

Resonant absorption . . . . . 21

Vacuum heating . . . . . 22

Ponderomotive force and $J \times B$ heating . . . . . 22

2.1.3 Mechanisms of ion acceleration . . . . . 24

Target normal sheath acceleration . . . . . 24

2.1.4 Radiation pressure acceleration . . . . . 25

2.1.5 Collision-less shock acceleration . . . . . 26
2.2 Neutron generation . . . . . 27
2.2.1 Neutron generation methods . . . . . 27
Nuclear fusions . . . . . 27
Photon-nuclear reactions . . . . . 28
Ion induced low-energy nuclear reactions . . . . . 29
2.3 Neutron moderation . . . . . 30
2.3.1 Method of neutron moderation . . . . . 30
2.3.2 Development of neutron moderator . . . . . 31
2.4 Thomson parabola ion spectrometer . . . . . 32
2.4.1 The configuration of thomson parabola ion spectrometer 32
2.4.2 Imaging plate . . . . . 33
2.5 Neutron time-of-flight detectors . . . . . 37
2.5.1 Liquid scintillator for fast neutron detection . . . . . 37
2.5.2 $^{6}$Li-glass scintillator for epithermal neutron detection . . 38

**3 Development of Time-gated Neutron Detector and Beamline 43**
3.1 Problems of time-of-flight neutron detection in high-power laser experiments . . . . . 43
3.2 Development of time-gated photomultiplier driver circuit . . . . 45
3.2.1 Necessity and purpose of the development . . . . . 45
3.2.2 Design of a photomultiplier driver circuit with an electrical time-gating system . . . . . 47
3.2.3 Test for temporal characteristic of the electrical time-gating circuit . . . . . 48
3.2.4 Test for time-gated photomultiplier tube in high-power laser experiments . . . . . 51
3.3 Development of epithermal neutron beamline for laser-driven neutron source . . . . . 52
3.3.1 Necessity and purpose of the development . . . . . 52
3.3.2 The development of nickle epithermal neutron collimator 54
3.3.3 The design of background shield . . . . . 58
3.3.4 The experimental demonstration of the beamline development . . . . . 58

**4 Single-shot Neutron Resonance Spectroscopy using Laser-driven Neutron Source 61**

4.1 Experimental setups . . . . . 61
4.2 Experimental results and analysis . . . . . 62
4.2.1 Energy spectrum of laser-driven ion acceleration . . . . . 62
4.2.2 Fast neutron generation results . . . . . 64
4.2.3 Single-shot neutron resonance spectroscopy results . . . 67
4.2.4 Evaluation of neutron duration and energy resolution . . 70

**5 Temperature Dependency of Neutron Resonance 77**
5.1 Experimental setup . . . . . 77
5.2 Experimental results . . . . . 79
5.2.1 Ion and fast neutron spectrum . . . . . 82
5.2.2 Simulation of epithermal neutron pulse duration and broadening on detectors . . . . . 82
5.2.3 Single-shot analysis of neutron resonance . . . . . 83
5.2.4 Analysis of Doppler broadening . . . . . 86

**6 Conclusion 91**

**Accomplishments 103**

# List of Abbreviations

| | |
|---|---|
| **LDNS** | **L**aser-**D**riven **N**eutron **S**ource |
| **NRA** | **N**eutron **R**esonance **S**pectroscopy |
| **TOF** | **T**ime-**O**f-**F**light |
| **CPA** | **C**hirped **P**ulse **A**mplification |
| **PC** | **P**itcher-**C**atcher |
| **LFEX** | **L**aser (for) **F**usion **EX**periments |
| **ILE** | **I**nstitute (of) **L**aser **E**ngineering |
| **IP** | **I**maging **P**late |
| **TPIS** | **T**hompson **P**arabola **I**on **S**pectrometer |
| **PHITS** | **P**article (and) **H**eavy **I**on **T**ransport (code) **S**ystem |
| **TNSA** | **T**arget **N**ormal **S**heath **A**cceleration |
| **PSL** | **P**hoto **S**timulated **L**uminescence |
| **RPA** | **R**adiation **P**ressure **A**cceleration |
| **FWHM** | **F**ull **W**idth at **H**alf **M**aximum |
| **HDPE** | **H**igh-**D**ensity **P**oly**E**thylene |

# Chapter 1

# Introduction

## 1.1 Neutron resonance spectroscopy

Neutron resonance spectroscopy (NRS) is a method of observing the resonance phenomena when neutrons strikes the nuclei. The NRS method can be used to investigate the isotope composition, temperature and other information about the nucleus inside of the target sample. This chapter mainly introduces the background and physical theories of NRS.

### 1.1.1 Neutron

Neutrons are the nucleons that constitute nucleus. The concept of neutrons was proposed by Rutherford in 1920. Chadwick firstly confirmed the existence of neutrons via the experiment of bombarding nucleus with  -particles in 1932 [1]. Since it is electrically neutral, neutron can easily react with nucleus.

One neutron is composed of two down quarks and one up quark. Some properties of neutrons are shown in Table1.1. In all the properties of neutrons,

| | |
|---|---|
| Mass | $1.67492749804(95)\times10^{-27}$ kg |
| Electric charge | 0 e |
| Spin | 1/2 |
| Mean lifetime | 881.5(15) s (free in vacuum) |

Table 1.1: Properties of neutrons

the most important one is that they carry no charge. The coulomb barrier can not affect neutrons, which allows neutrons of almost any energy to react with any nuclide. On other hand, this property also makes it very difficult to accurately measure the neutron energy. In nuclear physics, the neutron energy is generally described as the neutron temperature. The unit of neutron energy is usually given in electron volts (eV). When a bunch of free neutrons are scattered

in the material, the energy distribution of neutrons is then adapted to the Maxwellian distribution know for thermal motion. If the neutrons is regarded as an ensemble, according to the theory of thermodynamics, the temperature of this ensemble is depended on the kinetic energy of neutron thermal motion. The neutron temperature corresponding to the neutron energy ranges is shown in Table1.2 [2]. Despite of such lots of range names, there are actually no standard

| Neutron energy | Neutron temperature |
|---|---|
| 0.0∼0.025 eV | Cold neutrons |
| 0.025 eV | Thermal neutrons |
| 0.025∼0.4 eV | Epithermal neutrons |
| 0.4∼0.5 eV | Cadmium neutrons |
| 0.5∼1 eV | EpiCadmium neutrons |
| 1∼10 eV | Slow neutrons |
| 10∼300 eV | Resonance neutrons |
| 300 eV∼1 MeV | Intermediate neutrons |
| 1∼20 MeV | Fast neutrons |
| >20 MeV | Ultrafast neutrons |

TABLE 1.2: Neutrons energy ranges and temperatures

specification for neutron energy range naming but a customary definition. For instance, a neutron has kinetic energy of 0.025 eV is named as "thermal" because of the kinetic energy of its thermal movement corresponding to the temperature of ∼300 K, which is the "thermal" temperature. In this paper, "thermal" represents the energy range of around 0.025 eV, and "epithermal" represents the energy higher than thermal and lower than fast neutrons.

### 1.1.2 Background of neutron resonance spectroscopy

Since the 1930s, with the improvement of understandings on nuclear reaction mechanism, the neutron resonance theory has been greatly developed[3]. The high transmittance of neutrons could realize the non-destructive analysis of opaque objects. In 1937, as the initiation of neutron resonance diagnosis research, Bethe used the single-level neutron resonance cross section formula proposed by Breit and Wigner [4] in his article to derive the influence of temperature-induced Doppler broadening on the resonance spectrum [5]. In the mid-1980s, P. H. Fowler conceived an experiment for temperature measurement of static samples using epithermal neutron resonance. At that time, P. H.

Fowler, A. D. Taylor [6] and others performed the temperature measurement experiments in Los Alamos laboratory in the United States, laying the foundation for the application of neutron temperature measurement in the future and also promoting the development of neutron resonance detectors and experimental technology [7]. In recent years, many researchers have used neutron resonance technology in experiments such as material analysis [8–10], spatially resolved thermometry [11, 12] and shock wave measurement [13].

There have been various methods to non-destructively investigate isotopic composition and density of materials, such as Energy Dispersive X-ray Fluorescence (ED-XRF), X-ray Photoelectron Spectroscopy (XPS), Particle Induced X-ray Emission (PIXE), Neutron Activation Analysis (NAA) and Prompt Gamma-ray Analysis (PGA). These methods have high detection accuracy and sensitivity to detect the presence of isotopes at ppm to ppb levels. In comparison, the detection limit of NRS is generally at the 0.1% level. However, NRS also provides some advantage such as 2D imaging, temperature and shock wave measurements and investigation of lattice structures. At present, the non-contact temperature measurements generally requires the infrared thermography (IRT) method. A thermal camera captures an image of an object by detecting the radiation in the long-infrared range that emitted from the surface of the object. The mechanism of the IRT limits it to only measure the temperature at the very surface of the object. On the other hand, NRS is one of the methods that can measure the temperature inside an object without any contact. By combining the isotopic density detection, the transmissive temperature measurement and the 2D imaging of NRS, a isotopic-sensitive temperature profiling system can be realized in the near future.

The measurement of neutron spectra use the time-of-flight (TOF) method being applied with the pulsed neutron sources. The TOF method is to obtain neutron energy by calculation with a known neutron flight distance and time. The energy resolution depends on the beamline (flight distance) and is limited by the pulse duration of the neutron sources (detailed introduction in Chapter3). Since the full width at half maximum (FWHM) of resonance peaks can be 0.1 eV to several eV, the energy resolution of the TOF measurement is required to be high enough for the NRS. Most of the NRS studies were using neutron sources which are based on large-scale particle accelerators. To obtain sufficient energy resolution, a long beamline must be set for the neutrons, which

is typically a few tens of metres for accelerator-based neutron sources. However, a long beamline reduces the spatial density of neutrons arriving at the detector due to the spherically emission of pulsed neutron sources. To obtain a neutron spectrum with sufficient statistics, neutron bunches must be integrated for several hours in typical neutron facilities. Currently, the energy resolution and statistics are main problem that required to be solved for the practical applications of the NRS.

### 1.1.3 Physics and methods of neutron resonance spectroscopy

#### Neutron-matter interactions

There are kinds of neutron induced reactions including Potential scattering, Elastic resonant scattering, Inelastic resonant scattering, Radiative capture and Fission etc. Some of neutron induced reactions are shown in Table1.3. There is

| **Interaction without formation of a compound nuclei** | | |
|---|---|---|
| Potential scattering (elastic) | $n + A \Rightarrow n + A$ | Always possible |
| **Interactions occurring via formation of a compound nuclei** | | |
| Elastic resonant scattering | $n + A \Rightarrow n + A$ | Always possible |
| Inelastic resonant scattering | $n + A \Rightarrow n + A^*$<br>$A^* \Rightarrow A + \gamma$ | Usually with threshold of the first level of A |
| Radiative capture | $n + A \Rightarrow \gamma + (A + 1)$ | Always possible |
| Fussion | $n + A \Rightarrow PF_1 + PF_2$<br>$+ \ a \ few \ neutrons$ | May or may not be with a threshold |
| Reaction(neutron, charged particle) | $n + A \Rightarrow p + B$<br>$n + A \Rightarrow \alpha + C$<br>ect. | Usually with threshold, sometimes without threshold |

Table 1.3: Neutron induced reactions

only one reaction that is distinguished from reactions called potential scattering. In potential scattering, there is no actual contact between the neutron and the target nucleus, which means nuclear forces are not bought into action. The wave associated with neutron is scattered by the nuclear field. The process is

phenomenologically similar to the elastic collision between two balls with conserved momentum and kinetic energy. For other nuclear reactions, the neutrons are captured by the nucleus when they approach firstly. The category of the reactions can be described by the compound-nucleus model [14] which includes three stages:

1. The entrance channel: The incident neutron penetrates the nucleus. The isotope is increased to next rank, developed into a compound nucleus via the absorption of neutron. The absorbed neutron adds extra binding energy to the nucleus and make this compound nucleus excited.

2. Excited compound nucleus has a lifetime on the order of 10–14 s. On the other hand, the time required for a new nuclear bond to be created is on the order of 10–22 s. The much longer lifetime makes compound nucleus independent from the process that generates it. Thus, in the later period of compound nucleus, it can be treated as a single excited nucleus.

3. The exit channel: When the excited compound nucleus disintegrated, the extra energy brought by neutron is released. Most of the process is radioactive, with emitted photons, ions or other light particles. The excitation energy of the compound nucleus is related to binding energy of the nucleus and kinetic energy of the neutron, where the former is approximately 5 to 10 MeV[15] and the latter can be from zero to a few MeV. This is one of the reasons that makes almost all of particle-emissive reactions have energy threshold.

The neutrons capture process can be express as:

$$A + n \rightarrow (A+1)^{*}. \tag{1.1}$$

The excited nucleus $(A+1)^{*}$ then evolve into subsequently produced particles though various exit channels which represents different reactions (Table1.3).

### Cross section

The concept of cross section is introduced for evaluating the number of reactions between a flux of particles and targets. The microscopic interpretation of the cross section is an area around the target nuclei where a collision will occur if and only if the projectile (incident particle) hit. An intuitive scheme is shown as Figure 1.1. The trajectory of the projectile takes its center near

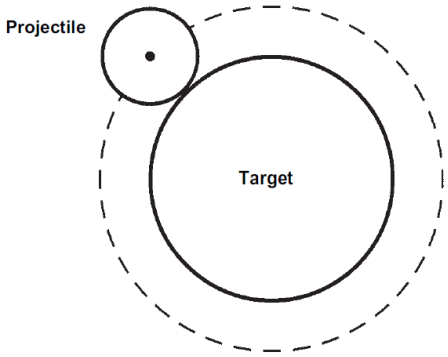


FIGURE 1.1: The concept of cross section[15]

the center of the target to within a distance less than the sum of radii, i.e. it must cross the circle in the plane of the figure whose radius is the sum of the radii of the two particles. The cross section is the surface area $\sigma$ of this circle. Generally, the cross section is considered as the probability of particle collision. Suppose there is a plane that consist of target nucleus with thickness of $dl$. The number of target nucleus is n per unit area. Then the probability of the projectile hitting one of targets is the surface area of the entire set of dashed circles divided by the total surface area. If the flux of projectile beam is $\phi$ and it will decrease by $d\phi$ according to

$$\frac{d\phi}{dl} = -n\sigma\phi. \tag{1.2}$$

Then the exponential attenuation of the beam intensity, i.e. the probability of reaction can be expressed as

$$\phi = \phi_0 e^{-n\sigma l}, \tag{1.3}$$

where $\phi_0$ is the initial beam flux, $\sigma$ is the cross section, $n$ is the atomic area density and $l$ is the total thickness of the target material. Since the radius of a nuclei is on the order of $10^{14}$ cm$^2$, the order of magnitude of the cross section should be in the region of $10^{28}$ cm$^2$. In nuclear physics, cross sections are expressed in barns:

$$1\,barn(b) = 10^{-24}\ \text{cm}^2 = 10^{-28}\ \text{m}^2.$$

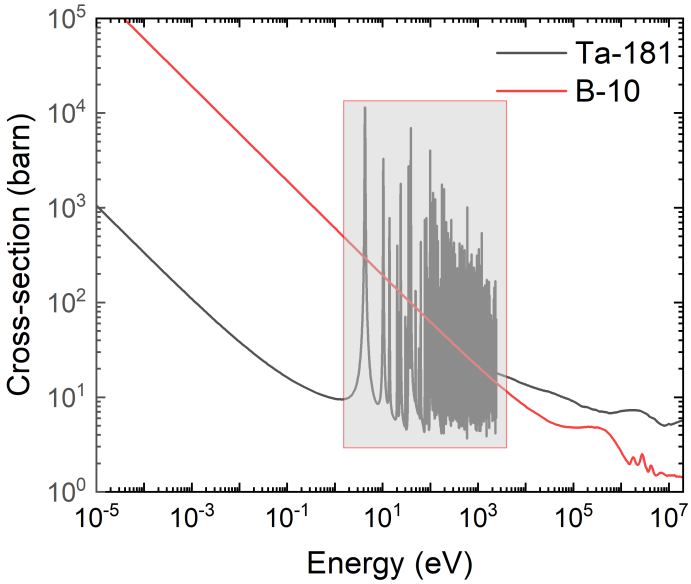


(a) Neutron absorption $(n, \gamma)$ cross section of $^{181}$Ta and $^{10}$B

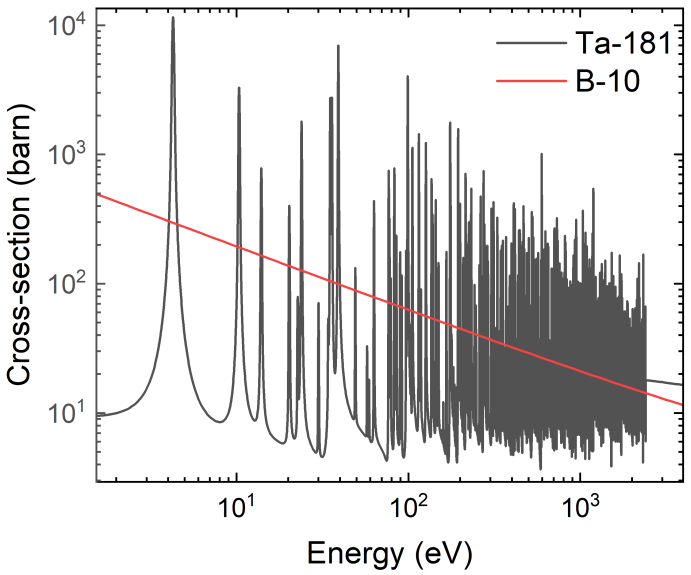


(b) Enlarged area

FIGURE 1.2

### Neutron resonance absorption

The neutron absorption cross section curves of $^{181}$Ta and $^{10}$B are plotted in Figure 1.2(a). One same behavior can be found in both two curves is "1/v" behavior. This is inversely proportional to the speed of the neutrons or to the square root of their kinetic energy. Since the longer low energy neutrons have longer de Broglie wavelength, they also see a larger portion of space than fast neutrons. This lead to larger cross sections in lower energy, i.e. the "1/v" behavior. On the other hand, the $^{181}$Ta curve shows several irregular peaks in epithermal domain (Figure 1.2(b)). This phenomenon is called **Resonance** of the neutron absorption. For $^{181}$Ta, a spectacular resonance peak is observed around 5 eV. The structure in levels of excited states of the compound nucleus $(A+1)^*$ give rise to the resonances of cross section. The excitation energy acquired by the compound nucleus is sum of the binding energy and the kinetic energy of the incident neutrons. If the excitation energy is exactly same with the one level of the compound nucleus, or in its immediate adjacent area (Figure 1.3), the reaction will occur easily, and a large cross section will be observed. Thus, the neutron cross section can change by thousands of times within a very narrow energy region where resonance peaks are located as shown in Figure 1.2(b). For light nuclei, the structure is relatively simple so that there are few or no resonances level. In contrast, since the heavier nuclei has increasingly crowded structures, amount of resonance peaks can be seen in the cross section curves.

Breit-Wigner (BW) single-level formula [4] firstly provided a qualitative evaluation for the cross section of neutron resonance as:

$$\sigma_i(E) = \pi \lambda\!\!\!^{-} g_j \frac{\Gamma_n \Gamma_i}{(E - E_r)^2 + \Gamma^2/4}, \tag{1.4}$$

where

- $E$: the kinetic energies of the incident neutrons.
- $E_r$: the energy of the resonance peak.
- $\lambda\!\!\!^{-}$: the neutron de Broglie wavelength divided by $2\pi$.
- $g_j$: the statistical factor introduced for different angular momentum orientations.

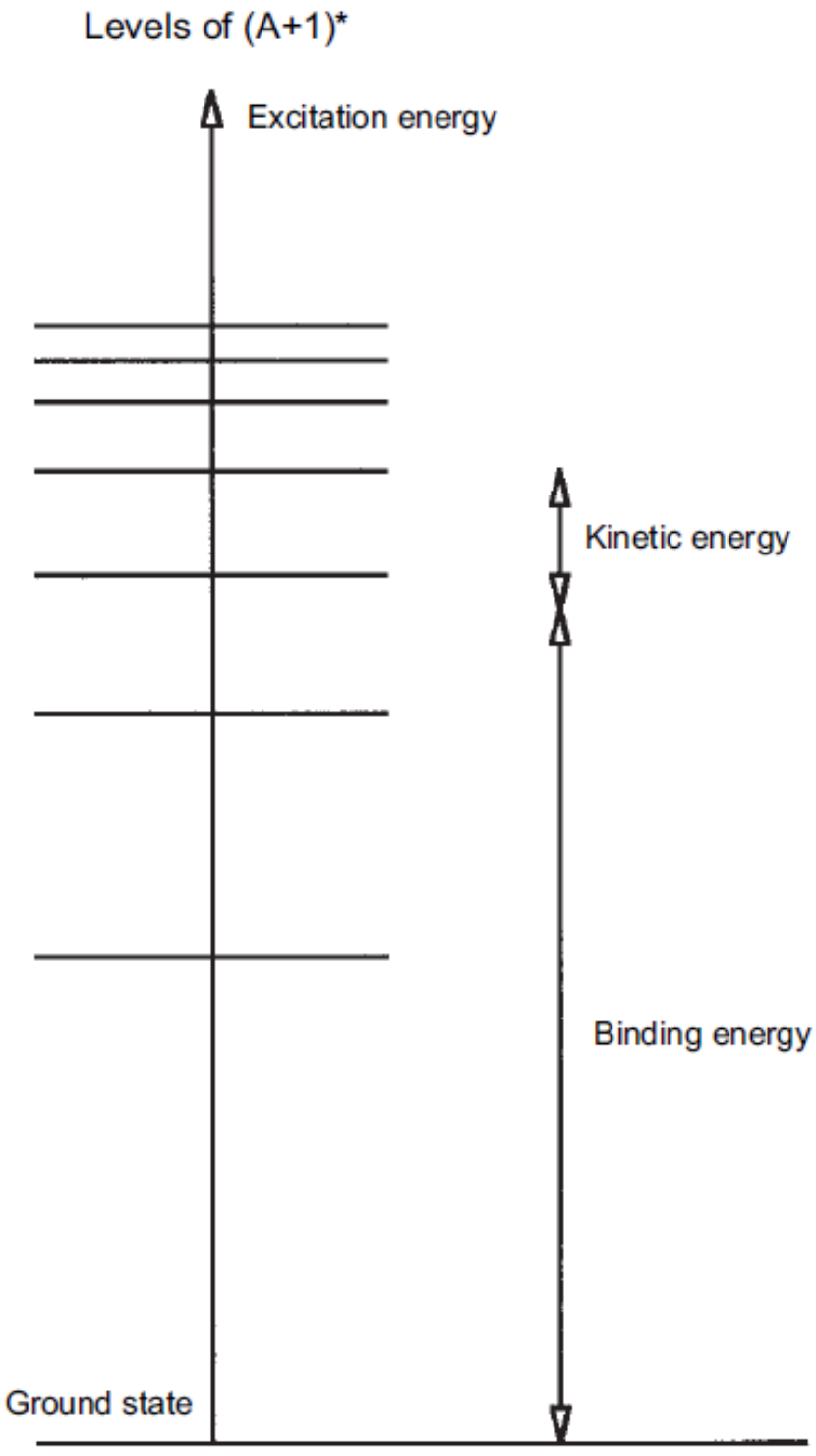


FIGURE 1.3: Neutron brings the nucleus to one of the excitation levels

- $\Gamma$: the width of the resonance. $\Gamma = \hbar/\tau$ where $\tau$ is the average lifetime of the compound nucleus, the width $\Gamma$ has the dimensions of energy and is usually expressed in meV.

- $\Gamma_i$: the partial widths of the neutron induced reactions. As previously introduced, the compound nucleus disintegrate along several exit channels which are represent the possible nuclear reactions such as neutron emission ($n = i$), photon emission ($i = \gamma$), fission ($i = f$), etc. The sum of all possible exit channels is $\Gamma$, which means the ratio $\Gamma_i/\Gamma$ is the probability that the reaction represented by $i$ will occur.

The Breit-Wigner formula describes the partial cross-sections for single resonance assumed to be isolated and determined by the $E_r$ and $\Gamma_i$. For neutron resonance absorption, $i$ is generally considered as $\gamma$ (radiative capture). In practice, the reaction rate can be described as

$$R_i(E) = \Phi \exp(-nl\sigma_i(E)), \tag{1.5}$$

where $\Phi$ is the neutron flux, $n$ is the atomic areal number density of the matter, $l$ is the depth of the incidence. The equation 1.5 gives the number of occurred reactions per unit time when an neutron beam is incident on a matter. For the possibility of a neutron to be absorbed, $\Phi = 1$ and $i = \gamma$ is substituted into the Equ. 1.5.

### 1.1.4 Time-of-flight method for neutron detection

Neutrons are generally measured by the TOF method [16], in which neutron signals are recorded temporally. As shown in 1.4, the neutron energy $E$ is calculated from the flight time $t$ and distance $d$.

$$E = m(\sqrt{(1 - (\frac{d}{tC})^2)} - 1), \tag{1.6}$$

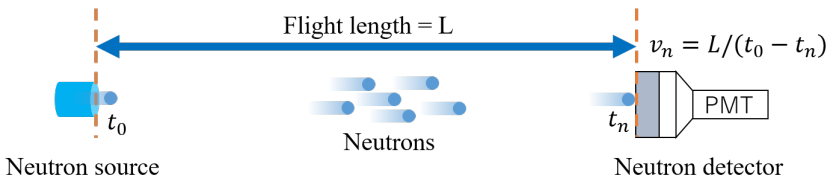


FIGURE 1.4: The time-of-flight method

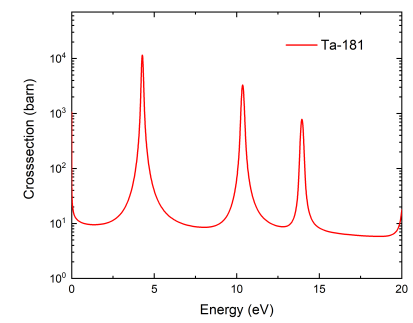


(a) Cross-section of $^{181}$Ta

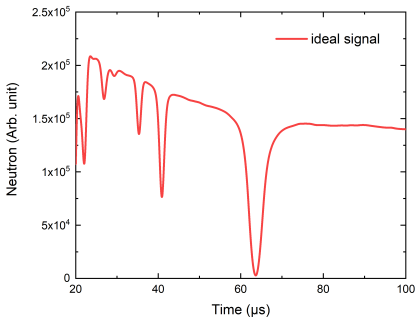


(b) An instance of the ideal NRS signal

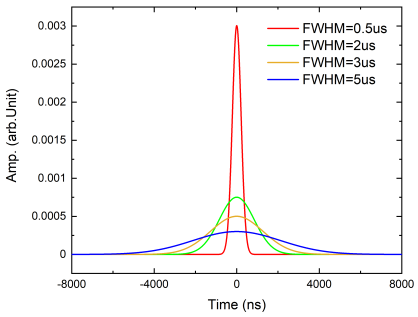


(c) Assumed pulses of neutron sources

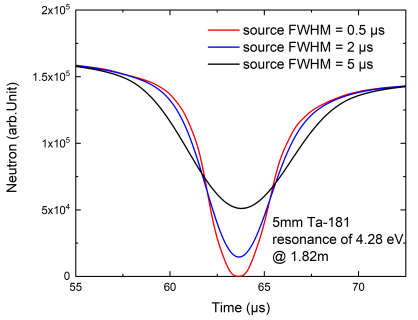


(d) Resonance peak changes with different source pulse duration

FIGURE 1.5

where $m$ is the rest mass of a neutron, $C$ is the speed of light. This formula is applicable to the relativistic cases that fast neutrons have energies over MeV and non-negligible velocities for the speed of light. For low-energy neutrons, the calculation can be reduced to the classical form $E = \frac{1}{2}mv^2$.

With a certain flight distance, the accuracy of neutron spectrum measured by TOF method is depends on the pulse duration of the neutron source. For instance, the absorption rate of a resonance sample $^{181}$Ta is calculated by neutron cross-sections of absorption (Fig. 1.5(a)). If it is multiplied by the simulated neutron signal (in time axis), an ideal neutron resonance spectrum with zero source pulse duration can be obtained (Fig. 1.5(b)). This ideal signal only responses to the neutron resonance of $^{181}$Ta and the time axis literally corresponds to the energy axis in TOF analysis. However, assuming that the neutron source has non-zero pulse duration as shown in Fig. 1.5(c), the neutron spectrum that measured by detector changes into Fig. 1.5(d). As shown in Fig. 1.5(d), with the broader pulse duration of the neutron source, the resonance peaks in the measured neutron spectrum also become broader. This is due to the temporal

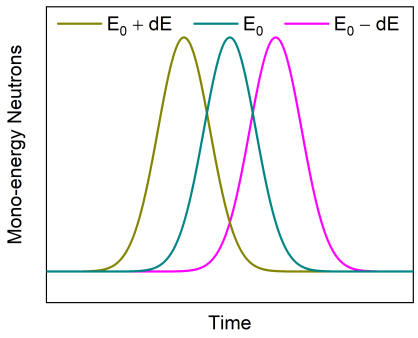


FIGURE 1.6: Temporal broadening of neutron source

broadening of the neutrons with the energies neighboring resonance energy. A bunch of mono-energetic neutrons has a pulse-shaped arrival time on the detector ($t = t_0 \pm \delta t$) and is overlapped by the neutrons in neighboring energy regions ($E_0 \pm dE$ in Fig. 1.6). Therefore, when converting time axis to energy axis, the time axis of neutron signal no longer corresponds exactly to the energy axis. Considering this effect, the accuracy of neutron spectrum measured by TOF method is affected by the source pulse duration.

### 1.1.5 Applications of neutron resonance spectroscopy

The applications of NRS includes isotope identification, density analysis and temperature measurement. Some instances of possible applications on isotope identification and density analysis:

- Archaeology: By checking the elements contained in archaeological materials, it is possible to determine the age of artifacts or estimate the manufacturing method and process.
- Nuclear safety: Nuclear debris may contain fuel elements such as uranium and plutonium. NRS can be used for the quantitative measurement of nuclear wastes or pollution. The non-contact measurements of NRS also guarantee the safety of workers.
- Alloy uniformity: To ensure the functionality of an alloy, the composition ratio and uniformity may be investigated. The NRS can be used to investigate the distribution of specific elements contained in the alloys.
- Material science: The phenomena that fluctuates over time such as shock wave, pressure and deformation can be detected by the NRS.

The temperature measurement using NRS has different features than existing methods. For example, the infrared thermometer is a most common approach of non-contact temperature measurement. The temperature of an object is inferred by measuring the amount of infrared energy emitted by the object and the emissivity. Limited by it's mechanism, the infrared thermometer can only measure the temperature on the surface. On the other hand, there are also many approaches, such as thermocouple, to measure the temperature at a certain depth inside an object. However, all these approaches need to use a probe to contact with the object. The NRS could be the only non-contact and non-destructive method to measure the internal temperature. Furthermore, the temperature measurement can be simultaneously implement with the isotope identification, which indicates the measurements can focus on a specific area or component. By these advantages, the NRS can be used in the precision production and testing such as semiconductors, laser etching and batteries.

The NRS has been mainly studied by using accelerator-based neutron sources. Many works towards to practical applications have been reported, such as material analysis [8–10], spatially resolved thermometry [8, 11, 12] and shock wave measurement [13, 17]. In these studies, the neutron energy spectroscopy is based on the TOF method. One of the current barriers to the method is that a pulsed neutron source is required to ensure all the neutrons are generated at same time. However, it is impossible to generate neutrons simultaneously using actual neutron sources. There is always a pulse duration applied to the generated neutrons, resulting in measurement errors in the determination of the flight time.

## 1.2 Laser-driven Neutron Source

The laser-driven neutron source (LDNS) is a method to generate neutrons by using high-power laser beams. It has been reported that the LDNS method is capable to provide a high neutron yield within a ultra-short single pulse. In this section, the background and methods of LDNS are introduced[18].

### 1.2.1 Background of Laser-driven Neutron Source

The concept of LDNS can be traced back to the breakthrough development of ultra-short and intense laser technology in recent decades. The discovery of Chirped Pulse Amplification (CPA)[19] awarded by Nobel prize in 2018[20] has

significantly improved the intensity of existed laser systems. The construction of large-scale laser facilities has been greatly accelerated since that the paper of Nuckolls et al. [21] was published in 1972 on the inertial confinement fusion driven by laser implosion. After that, many works in laser-driven plasma physics have been reported.

Around 2000, some groups reported experimental results using high-power lasers to accelerate high-energy ions [22–24]. The laser-driven particle generation and acceleration has attracted attentions. Many experimental and theoretical works were reported. For instance, TNSA (Target Normal Sheath Acceleration) is widely known as a typical laser particle acceleration mechanism. The charge separation in the plasma generated by relativistic intensity laser irradiation can lead to a huge potential difference ($\sim$TV/m) with a tiny distance ($\sim$1 μm). This intense electric field which is called sheath field can efficiently accelerate ions to tens or even hundreds of MeV.

As a further application of laser-driven ion source, the LDNS is proposed. The LDNS has been reported to combine the ultra-short pulse duration and high flux[25, 26]. Some efficient methods of neutron generation using laser pulses, such as using high-energy ions (protons or deuterons) accelerated by laser-matter interactions to generate neutrons by nuclear reactions with a secondary target (Li or Be) [27, 28], nuclear fusion [29], and photonuclear reactions [30], have been reported. A currently highest neutron yield of $\sim 10^{11}$ has been achieved [28, 29, 31, 32] for a single pulse. Furthermore, low-energy neutrons at eV $\sim$ meV region have been generated by employing neutron moderators made of hydrogen-rich materials at room temperature [28, 33–35] or cryogenically cooled solid hydrogen [26]. The short pulse duration and miniature scale of an LDNS allow a smaller neutron moderator, resulting in a reduction of the neutron pulse expansion in the moderation process.

### 1.2.2 Applications of Laser-driven Neutron Source and comparison with other neutron sources

As an newly developed neutron source, LDNS [18, 28, 29, 31, 32, 36–41] have attracted widespread attention for their compactness and short pulse performance. A currently highest neutron yield of $\sim 10^{11}$ has been achieved [28, 29, 31, 32] for a single pulse. At present, the neutron beams generated by high-power laser systems are mostly used for the researches on basic science such as nuclear physics [41] and astrophysics [42]. This is because most of the

high-power laser systems are designed with a large scale for the proposes of fusion, plasma physics and so on. Most of these applications of LDNS using the high-flux fast neutron beams.

However, there are some applications developed recently focus on low-energy neutrons at eV $\sim$ meV region. The low-energy neutrons generated by employing a moderator made of hydrogen-rich materials [26, 28, 33–35] provide industrial applications such as neutron radiography [43–45] and resonance spectroscopy [28, 35, 46]. These applications are benefited by the high penetrating ability of neutrons while the neutron induced nuclear reactions can provide the information of isotopes.

As the main topic of this research, the short-pulse LDNS shows a new direction of NRS that is real-time detection. The miniature scale of an LDNS allow a smaller neutron moderator, resulting in a reduction of the neutron pulse expansion in the moderation process. Combining with the TOF method, LDNS can provide a much higher energy resolution than traditional neutron sources. With that energy resolution, a much shorter beamline (flight distance) can be set for NRS. Both of the high peak flux of LDNS and the short beamline contribute to the detected neutron number which determines the statistics in the spectrum. It is possible that the statistics of a single shot of the lasers satisfy the requirement for obtaining a continuous spectrum. Therefore, there is a possibility to realize sing-shot NRS by using LDNS, while it is barely achieved in other neutron sources.

There are also other neutron sources that can be used for the applications. Since the neutron being discovered in 1932 [1], many approaches of neutron generation have been developed. So far, the most representative neutron sources are radioisotopes, nuclear reactors and particle accelerators. The most common radioisotope neutron source is the isotope $^{252}$Cf that undergoes spontaneous fission to generate neutrons. A typical $^{252}$Cf source emits $10^7$ to $10^8$ neutrons per second. The nuclear fission reactors can both produce neutrons and spontaneous fission neutron sources. However, recently, the reactors have been favored for commercial energy usage. Both radioactive neutron sources and reactors produce neurons continuously over time so that they are not suitable for the neutron spectrum analysis with TOF method. As introduced in section 1.1.1, most of current NRS experiments were implemented by using accelerator-based neutron sources. However, the relatively long pulse duration in the accelerator neutron sources imposes many restrictions on the NRS. To ensure a sufficient

energy resolution of TOF method, the beamline of accelerator neutron sources are generally very long (over ten metres). The long beamline greatly reduces the utilization efficiency of neutrons due to the small solid angle of detectors. Therefore, almost all the NRS measurements using accelerator take the integrated results with a long period of times and lots of pulses. This adds more random errors on the measurement.

The high pulsed yield of LDNS shown the potential of NRS measurement in a single shot of laser, which greatly promoted the practical application of NRS technology. At present, accelerator-based neutron sources are more stable while the high-power lasers have many uncertainties from shot to shot. However, when a single laser shot is used for the NRS, the energy resolution depends to the short-term expansion of the initial neutron pulse is expected to be higher than that using an accelerator-based neutron source. Furthermore, with the development of pumping laser systems operating at 10–100 Hz [47, 48], LDNS may provide a real-time thermometry of isotopes that probes the instantaneous temperature of dynamic objects.

Previous studies have demonstrated NRA using LDNS [35, 49, 50]. In the newest work at ILE, Osaka Univ. [18, 28], neutron resonances in the epithermal (several eV) region were measured by using a 1.8 m beamline with an LDNS. The results reported that one resonance spectrum was obtained with a single bunch of neutrons generated by a single pulse of the laser.

## 1.3 The main topic of this work

This thesis consists of the following chapters:

- Chapter 1: Introduction to the thesis topic.
- Chapter 2: A detailed introduction of laser-driven neutron source.
- Chapter 3: An introduction of the time-gated neutron detector and beamline developed for LDNS experiments.
- Chapter 4: The Experiment of sing-shot NRS using LDNS and experimental results.
- Chapter 5: Further investigation on the temperature dependency of neutron resonance.
- Chapter 6: Conclusion of the thesis.

# Chapter 2

# Development of Short-Pulse Laser-driven Neutrons

This chapter introduces the development of Laser-Driven Neutron Source (LDNS) at ILE, Osaka University. The contents include the laser-driven ion acceleration, the neutron generation and the neutron moderation. In addition, the detectors of ions and neutrons are also introduced in this chapter.

## 2.1 Laser-driven ion acceleration

### 2.1.1 Relativistic plasma generation using high-intensity laser beam

In this work, the ion acceleration occurring in the interaction with solid targets, in which the electron density $n_e$ is much higher than the critical density $n_c$.

$$n_c = \frac{m_e \omega^2}{4\pi e^2} = 1.1 \times 10^{21}\ cm^{-3} (\frac{\lambda}{1\ \mu m})^{-2}, \tag{2.1}$$

where $m_e$, $\lambda$ and $\omega$ are mass of the electron, wave length and frequency of the laser, respectively. If there is $n_e = n_c$, the equation $\omega_p = \omega$ exit. The $\omega_p = \sqrt{4\pi n_e e^2 / m_e}$ and $\omega = 2\pi c/\lambda$ are the plasma and laser frequencies, respectively. Therefore, the refractive index of the plasma can be written as

$$\eta = \sqrt{(1 - \frac{\omega_p^2}{\omega^2})} = \sqrt{(1 - \frac{n_e}{n_c})}, \tag{2.2}$$

when the condition is $n_e > n_c$, the $\eta$ has imaginary values which means the laser pulse cannot propagate the matter. Therefore, most of the laser-plasma interactions can only occur in the conditions of $n_e > n_c$ or $n_e \approx n_c$.

The EM field of a laser beam is given by the vector potential $A$.

$$\boldsymbol{A}(\boldsymbol{r},t) = Re[\boldsymbol{A_{pol}} exp\{\boldsymbol{i}(\boldsymbol{k}\cdot\boldsymbol{r} - \omega t)\}], \tag{2.3}$$

where the $\boldsymbol{k} = 2\pi/\lambda$ is wave number, $\omega$, $\lambda$, $\boldsymbol{r}$ and $t$ are angular frequency and wavelength of laser, space, and time, respectively. The $\boldsymbol{A_{pol}}$ represents the polarization of laser. For instance, when $\hat{\boldsymbol{e}}_{\boldsymbol{x}}$,$\hat{\boldsymbol{e}}_{\boldsymbol{y}}$ are unit vectors in the coordinate system, $A_0\hat{\boldsymbol{e}}_{\boldsymbol{x}}$ represents a linearly polarized laser and $A_0(\hat{\boldsymbol{e}}_{\boldsymbol{x}} \pm \hat{\boldsymbol{e}}_{\boldsymbol{y}})$ represents a circularly polarized laser. According to Maxwell' s equations, the laser electric field $\boldsymbol{E}$ and magnetic field $\boldsymbol{B}$ can be expressed by

$$\begin{aligned} \boldsymbol{E} &= -\frac{1}{c}\frac{\partial \boldsymbol{A}}{\partial t} = Re[\frac{i\omega}{c}\boldsymbol{A_{pol}} exp\{\boldsymbol{i}(\boldsymbol{k}\cdot\boldsymbol{r} - \omega t)\}], \\ \boldsymbol{B} &= \boldsymbol{\nabla}\times\boldsymbol{A} = Re[\boldsymbol{ik}\times\boldsymbol{A_{pol}} exp\{\boldsymbol{i}(\boldsymbol{k}\cdot\boldsymbol{r} - \omega t)\}]. \end{aligned} \tag{2.4}$$

The electrons in high-intensity laser ($> 10^{18}$ W/cm$^2$) field move with the oscillation of laser electric field. The momentum can be expressed as $P_{osc} = eE/\omega_0$ and normalized to $P_{osc}/m_e c$, where $e$ is the elementary charge, $E$ is the laser electric field, $\omega_0$ is the laser angular frequency, $m_e$ is the rest mass of the electron, and $c$ is speed of light. This normalized momentum of electrons can be expressed by laser intensity $I_0$ by

$$a_0 = 0.85\times 10^{-9}\lambda_0[\mu m]\sqrt{I_0[W/cm^2]}, \tag{2.5}$$

where $\lambda_0$ is the wavelength of laser. For an example, if a laser beam with $\lambda_0 = 1$ μm has intensity higher than $10^{18}$ W/cm$^2$, there is $a_0 > 1$ and the oscillating electrons in electric field is accelerated to a relativistic velocity within one cycle. The plasma formed by such electrons is defined as the relativistic plasma. The laser has the intensity that make $a_0 > 1$ is defined as the relativistic laser.

In the regime of relativity, the electron mass is greater than the static mass, resulting a decrease of critical density. The relativistic critical density $n_{cr}$ is

$$n_{cr} \sim n_c\sqrt{1+\frac{a_0^2}{2}}. \tag{2.6}$$

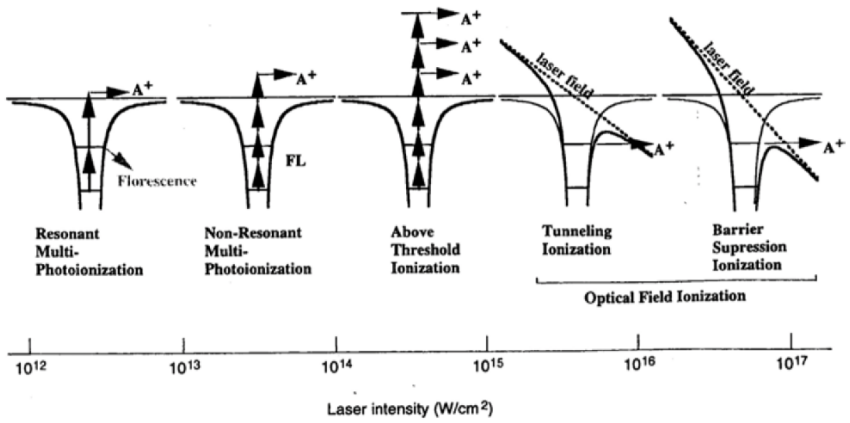


FIGURE 2.1: Laser intensity and ionization mechanism[51]

Therefore, when laser intensity increases, the laser beam becomes easier to propagate in high-density plasma. The phenomenon is called abnormal penetration.

A solid target material can be ionized and turned into plasma on its surface where a laser beam with the intensity exceeding the ionization threshold of the target irradiates on. The degree of ionization mainly depends on the intensity of laser beam, which is the intensity of electric field that excites electrons in the target. The corresponding relationship between laser intensity and ionization mechanisms is shown in Fig. 2.1.

However, for the laser intensity reaches relativistic region, the laser-plasma interaction turns different with the mechanism. As introduced in Chapter1, high-power lasers are based on the CPA technology. Generally, CPA lasers are accompanied by pre-pulse components. Fig. 2.2 shows a typical time structure of laser waveform. Before the main pulse arrives, there are pedestal components in femtosecond and picosecond scale respectively. And there is a much longer ASE (Amplified Spontaneous Emission) component which is produced by spontaneous emission of gain medium. The intensity ratio of main pulse to pre-pulse is defined as the contrast of laser. The contrast of LFEX is about $10^{9\sim11}$. By the pre-pulse of high-power lasers, the radiated solid target is ionized (by the mechanisms in Fig. 2.1) and forms an area of plasma before the main pulse arrival. When the main pulse arrivals, the interaction between relativistic laser and plasma causes the laser energy transferred to the charged particles in plasma. Since relatively large charge-to-mass ratio, the electrons in plasma are accelerated prior. This interaction process varies depending on factors such as plasma scale length, main pulse intensity, polarization, angle of incidence, etc.[52].

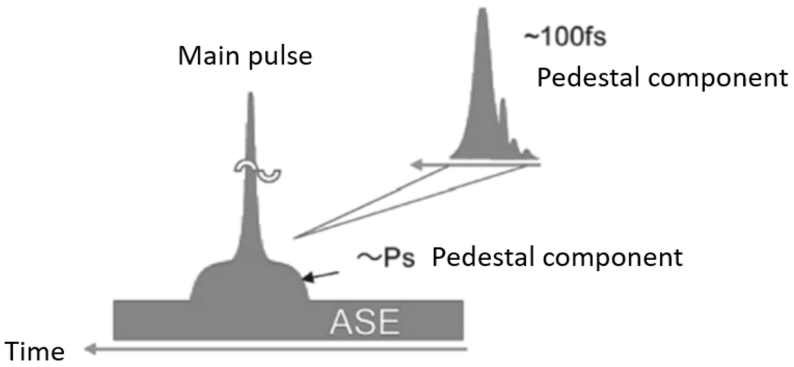


FIGURE 2.2: Time structure of laser waveform

### 2.1.2 Electron heating by laser-plasma interaction

For solid targets that generally have densities higher than the critical density. The energy transfer between laser and plasma occurs by the heating of energetic electrons that exits in the low-density plasma region where laser can penetrate.

The process of hot electron generation is quite complex and not yet completely understood. Since this work focus on the neutron generation using the ions accelerated by laser irradiation, a briefly introduction of existing theories are presented here rather than a in-depth discussion. The mechanisms of absorption of electromagnetic waves in plasma are introduced below.

#### Inverse bremsstrahlung absorption

Inverse bremsstrahlung absorption is the most typical mechanism for absorption of electromagnetic waves in plasma. The oscillating electrons and ions in the laser electric field collide and scatter randomly. The energy transferred by laser electric field is transformed into thermal kinetic energy via collision of scattered electrons. Suppose that the plasma irradiated by laser has a density of $n_e = n_c exp(-z/L)$. Where $z$ is the axis that perpendicular to incident surface, $L$ is plasma density scale length. Then the absorption rate of inverse bremsstrahlung absorption is

$$\eta = 1 - exp(-\frac{8v_{ei}L}{3c}\cos^3\theta), \tag{2.7}$$

where $\theta$ is incident angle of laser beam, $v_{ei}$ is collision frequency of electrons and ions. The $v_{ei}$ can be expressed by

$$v_{ei} \propto \frac{n_i Z^2}{T_e^{\frac{3}{2}}}, \tag{2.8}$$

where $n_i$, $Z$, $T_e$ are ion density, charge number of ions and plasma electron temperature, respectively. It can be seen that as electron temperature increases, the collision frequency of plasma decreases. Therefore, as the laser intensity increases, inverse bremsstrahlung absorption is suppressed. When laser intensity increases to $10^{15}$ W/cm$^2$, the resonant absorption mechanism is on dominant position.

**Resonant absorption**

Assuming that a laser beam is incident on a target surface obliquely, and there is a thin plasma on the surface. Based on Snell' s law, the laser is only able to propagate to $n_c \cos^2\theta$ and then reverse as shown in Fig. 2.3. For P-polarized lasers, the electric field has a component in the direction of plasma density gradient ($\boldsymbol{E} \cdot \boldsymbol{\nabla} \boldsymbol{n} \neq 0$). The electric field can resonantly generate plasma waves ($\omega_0$) near the critical surface (evanescence layer) via tunneling effect. The acceleration effect of the electric field $E_d$ is

$$\begin{aligned} \frac{E_d}{\epsilon(z)} &= \frac{E_L}{\sqrt{2\pi\omega_0 L_n/c}}\phi(\tau), \\ \tau &= (\omega_0 L_n/c)^{\frac{1}{3}} \sin\theta, \\ \phi(\tau) &\cong 2.3\tau exp(-2\tau^3/3), \end{aligned} \tag{2.9}$$

where $\epsilon$ is dielectric constant, and $L_n$ is density scale length. The energy transferred from electromagnetic waves to electron plasma waves is

$$f_{ra} = \frac{\phi^2(\tau)}{2}. \tag{2.10}$$

This absorption is a collision-less process, and electron energy mainly comes from the forced vibration of laser electric field. The conditions of resonant absorption are mainly related to the plasma refractive index, electron density and incident angle. Therefore, this mechanism occupies a dominant position when irradiating laser has wavelength of 1∼10 μm and pulse duration shorter

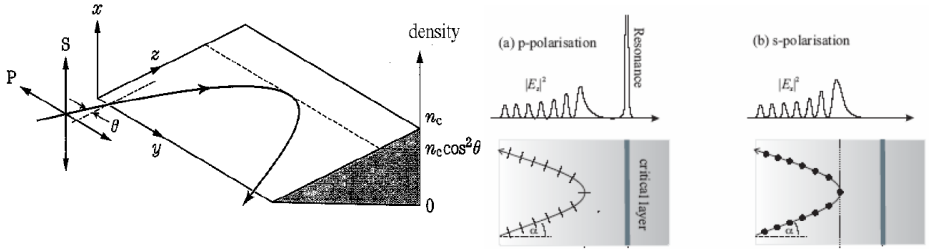


FIGURE 2.3: Resonant absorption

than 100 ps. And there is an optimal incident angle $\theta$ for resonant absorption.

$$(\frac{\omega L}{c})^{\frac{1}{3}} \sin\theta = 0.8. \tag{2.11}$$

### Vacuum heating

At very high intensities (relativistic intensity), absorption may be due to the generation of energetic electron through a mechanism which called Vacuum heating. In relativistic intensity regime, the plasma on the laser irradiation surface has a very steep density gradient. Similar to resonant absorption, a P-polarized laser beam will be totally reflected at a very shallow depth on the surface and generates an oscillating field extending out of the surface. For intense fields, electrons can be driven from the plasma surface into the vacuum region (Fig. 2.4). After half of an oscillation period, the electrons re-enter the plasma with higher energies and may cross the evanescence layer to deliver their energies. Therefore, the electrons escaping from the accelerating field region can be considered to be 'absorbed' in the plasma. During the half-oscillation on the vacuum side, the electrons are heated to close to the order of the oscillation energy in the external oscillating field. The electrons can be driven across the plasma-vacuum interface during half-oscillation by both the $\boldsymbol{E}$ and $\boldsymbol{v} \times \boldsymbol{B}$ terms in the Lorentz force with velocities of $\omega$ and $2\omega$, respectively. This mechanism originally proposed by Brunel [53].

### Ponderomotive force and $J \times B$ heating

The interaction of relativistic intensity laser and plasma is highly nonlinear, so it must be described by dynamic model. The Ponderomotive force is a non-linear force that a charged particle experiences in an inhomogeneous oscillating electromagnetic field. To consider the movement of electrons in a high-frequency electric field whose amplitude varies with space, the electrons can be treated as

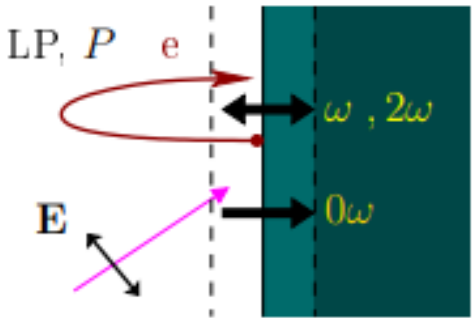


FIGURE 2.4: Vacuum heating

fluids. So the momentum equation of electrons can be expressed by

$$\frac{\partial \boldsymbol{\mu_e}}{\partial t} + \boldsymbol{\mu_e} \cdot \boldsymbol{\nabla} \boldsymbol{\mu_e} = -\frac{e}{m_e}\boldsymbol{E} - (\frac{e}{m_e c}\boldsymbol{v} \times \boldsymbol{B}). \tag{2.12}$$

Assuming the plasma is a cold plasma, the electron pressure is ignored. If the nonlinear term is ignored, electron velocity can be obtained as

$$\boldsymbol{\mu_h} = \frac{e\boldsymbol{E}}{m_e \omega} \cos(\omega t). \tag{2.13}$$

It can be seen that in this case the electrons simply oscillate around an initial point as happens in a homogeneous electric field. If nonlinear term is extracted, the equation can be written as

$$\boldsymbol{F_p}(t) = -\frac{1}{2}\frac{e^2}{m_e \omega^2}\nabla|\boldsymbol{E}|^2 \cos^2(\omega t) = -\frac{1}{4}\frac{e^2}{m_e \omega^2}\nabla|\boldsymbol{E}|^2(1 + \cos(2\omega t)), \tag{2.14}$$

which including steady ponderomotive force and a term oscillating at $2\omega$ frequency. The mechanism caused by the oscillating term is called $J \times B$ heating[54]. In this case, the electrostatic field driven by the oscillation component of ponderomotive force causes electron acceleration.

$$\frac{\partial \boldsymbol{P_c}}{\partial t} = -e\boldsymbol{\nabla}\phi - m_e c\boldsymbol{\nabla}(\gamma - 1). \tag{2.15}$$

Therefore, the ponderomotive potential is given by

$$U_p = (\gamma - 1)m_e c^2. \tag{2.16}$$

Assuming electron energy is derived from ponderomotive potential, the effective electron temperature approximates Maxwellian distribution[55]. It can be

expressed by

$$T_{hot} \cong (\sqrt{1 + \frac{I\lambda_{\mu m}^2}{2.74 \times 10^{18}}} - 1) \times 511\ keV. \tag{2.17}$$

### 2.1.3 Mechanisms of ion acceleration

Since the first experimental result of accelerated protons with beam-like properties and multi-MeV energies were reported in 2000[22–24], more theoretic and experimental works have been done to investigate the mechanisms and its physics of laser-driven ion acceleration. While most of these works have based on sheath acceleration processes, several novel mechanisms have been proposed. The research of laser-driven ion acceleration has been oriented to various foreseen applications in medicine, industrial inspection, nuclear fusion and high energy density science.

#### Target normal sheath acceleration

With the abounding generation of fast electrons via relativistic laser irradiation, intense electrical currents penetrate the target: the current density may be of the order of $J_f \sim 10^{11}$ A·cm$^{-2}$ which correspond to more than $10^{11}$ A through the focal area. If a thin foil target (0.1∼10 μm) is used, the fast electrons reach the rear side of the target and be captured by Coulomb potential of ions, creating a charge separated region [56] (Fig. 2.5). In this region, which is also called sheath, a quasi-electrostatic field with an intensity of up to 10 GV·cm$^{-1}$ is formed in a short distance (∼1 μm). The quasi-electrostatic field is also called sheath field. The sheath field accelerates ions towards the

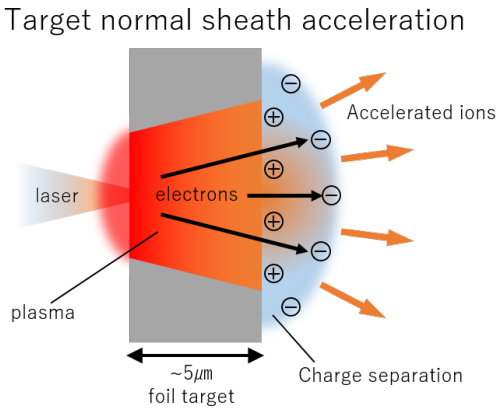


FIGURE 2.5: The basic scheme of TNSA

direction normal to the target surface, so the mechanism is called Target Normal Sheath Acceleration (TNSA). For the relatively thicker solid target (>1 μm) and picosecond-femtosecond laser pulses, the TNSA generally dominates ion acceleration. In this work, the TNSA of ions is driven by LFEX laser that focus on a foil target with thickness of 1.5∼5 μm.

### 2.1.4 Radiation pressure acceleration

Another mechanism is called Radiation Pressure Acceleration (RPA). The momentum carried by EM waves may be delivered to a non-transparent medium via both absorbing and reflecting. This effect is regarded as the Radiation Pressure. For instance, when a plane, monochromatic EM wave with intensity of $I$ and frequency of $\omega$ normally incident on the surface of a medium, the radiation pressure $P_{rad}$ is expressed by

$$P_{rad} = (1 + R - T)\frac{I}{c} = (2R + A)\frac{I}{c}, \tag{2.18}$$

where $R$, $T$ and $A$ are the reflection, transmission and absorption coefficients (with $R + T + A = 1$), respectively. If an ultra-intense laser irradiates a dense plasma, the radiation pressure is coupled to the electrons via the steady ponderomotive force in Eq.2.16. In the case of thick targets, the radiation pressure pushes the electrons in over-dense plasma inward, creating a charge separation layer and an electrostatic, depressed field (Fig. 2.6(a)). This field in turn leads

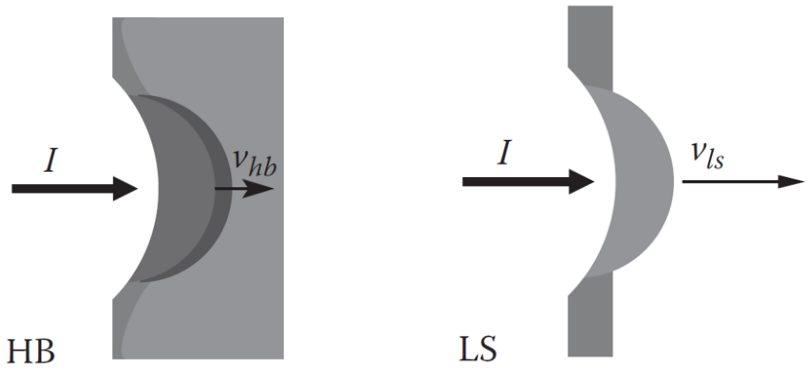


(a) Hole Boring (b) Light Sail

FIGURE 2.6: Simple illustration of RPA

the acceleration of ions. The dynamics which the ions are pushed forward by the ponderomotive force called Hole Boring (HB)[55]. If the target is thin enough that the front of ions pushed by HB process reaches the rear of the target during laser irradiation (Fig. 2.6(b)), the RPA is in the regime of Light Sail (LS). In this case, the ions are not covered by the plasma, so the laser is able to accelerate ions to higher energies[57].

### 2.1.5 Collision-less shock acceleration

High intensity laser may generate collision-less shock waves under certain conditions. The steep front of plasma density and potential propagates in the plasma with supersonic velocity. This supersonic front may generate shock waves via charge separation effects instead of collisional and viscosity effects in standard hydrodynamics. For instance, a shock wave propagates in the plasma with velocity of $v_{sh}$. It is given by

$$v_{sh} = Mc_s, (M > 1), \tag{2.19}$$

where $c_s$ is the 'speed of sound', that is, the velocity of acoustic waves in plasma. And the $M$ is the Mach number, which is defined as the ratio of $v_{sh}$ and $c_s$. Since $M > 1$, there is a shock wave with an extremely steep density distribution propagates in an expanding plasma (Fig. 2.7).

Supersonic front of the shock wave generates a steep density gradient, which reflects ions via electric field generated by prior accelerated electrons. Since there is no collision during reflection process, the velocity of reflected ions is $v_{ions} \sim 2Mc_{s0} + v_0$, where $v_0$ is original velocity of ions in expanding plasma.

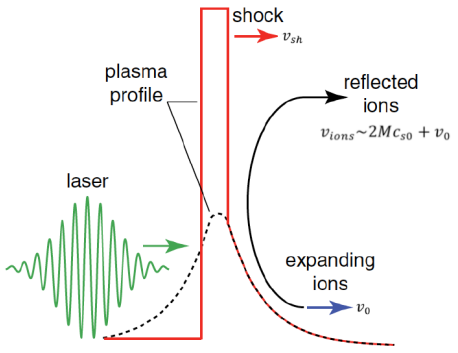


FIGURE 2.7: The basic scheme of CSA

Therefore, this mechanism accelerates ions with quasi-monoenergy and is called Collision-less Shock Acceleration (CSA).

## 2.2 Neutron generation

Generally, neutrons may be released from nuclei via energetic radiation including electromagnetic radiation and high energy ions. In addition, neutrons also can be released as a consequence of fusion reactions, which has been demonstrated in inertial confinement fusion experiments and applied in spallation neutron sources. Ultra-intense lasers have been proposed as a new approach for brilliant, compact and highly efficient neutron source. In spite of lower yield in a long period when compared with accelerator-driven sources or high flux reactors, the Laser-Driven Neutron Source (LDNS) has emerged a high yield per bunch and an ultra-short pulse duration. As the current neutron spectrum measurement is focused on TOF method, the features of LDNS make it possible to greatly improve the accuracy of neutron resonance spectroscopy, which can promote the application of neutron penetration analysis technology.

### 2.2.1 Neutron generation methods

#### Nuclear fusions

As an expected solution to future energy problems, nuclear fusion has attracted much attention in nearly 100 years since its discovery. The reaction processes with the combination of two or more nuclei or subatomic particles, generating one or more different particles. The difference in mass between the reactants and products due to the change of atomic binding energy is manifested as either the release or the absorption of energy. In the early 1970s, Inertial Confinement Fusion (ICF) [58] using laser irradiation appeared to be a practical approach to power production via nuclear fusion. Generally, laser beams are irradiated on the target to heat and compress the fuel. As the typical reaction for ICF, D-D and D-T reactions are expressed by

$$D + D \rightarrow^{3} He + n + 3.28\ MeV,$$
$$D + T \rightarrow^{4} He + n + 17.6\ MeV.$$

Both of these two reactions generate neutrons. These kinds of thermonuclear fusion reaction usually require MJ (Mega Joule) laser systems, and most of the

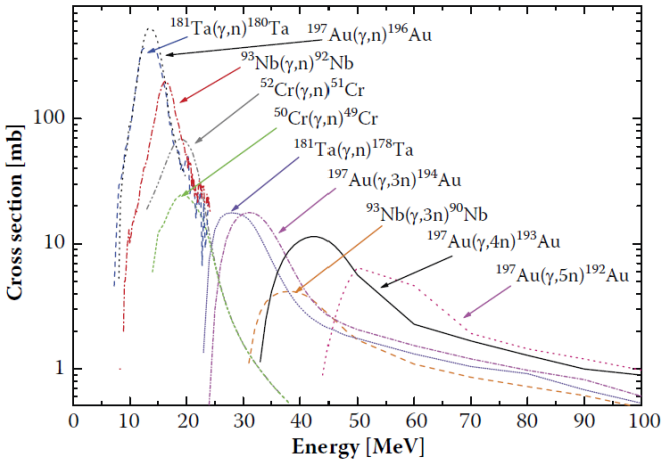


FIGURE 2.8: Cross-sections of photo-nuclear $(\gamma, xn)$ reactions for different isotopes[59]

research focuses on the improvement of ICF. The neutron yield of ICF experiments is usually used as the evaluation parameter of fusion and has relatively lower numbers.

### Photon-nuclear reactions

If a nucleus absorbs high-energy photons with energy exceeding the binding energy, the particles such as neutrons, protons, deuterons and -particles are released from nucleus. The reaction is regarded as the photo-nuclear reaction. A hot electron beam generated by interaction of intense laser and matters can produce X-rays with the energy over 15 MeV in high-Z materials[60] via the mechanism of Bremsstrahlung. The energy of Bremsstrahlung photons depends on the hot electrons whose energy is directly related to the laser intensity. Therefore, the energy of X-rays can exceed the threshold of photon-induced nuclear reactions. Through the cross section of $(\gamma, xn)$ reaction is usually smaller than that of proton collision reaction, it can reach 1 barn in some high-Z materials. Fig. 2.8 gives cross section of some isotopes.

Due to the high transmittance of X-rays, a large target is required to make X-rays completely reacted. Considering the efficiency of neutron moderation (as introduced in Section2.3), a large neutron source also requires a large moderator. Since the performance of short pulse is effected by the moderator size, the photo-nuclear reaction is not suitable for NRS using LDNS.

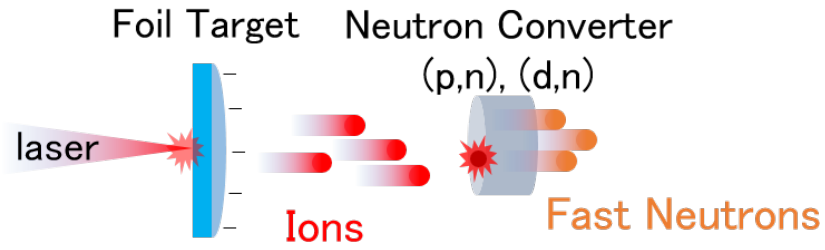


FIGURE 2.9: A typical pitcher-catcher geometry for laser-driven neutron source

**Ion induced low-energy nuclear reactions**

Due to the large cross-section of neutron producing reactions, ion-induced neutron generation has relatively higher efficiency. Taking advantages of laser-driven ion accelerations, a compact neutron source with high yield and short pulse duration can be realized via 'Pitcher-Catcher' (PC) Method [27, 61]. As details, the laser-driven ions that accelerated via TNSA mechanism are 'thrown' towards a neutron converter. Then the neutron converter which is generally Low-Z materials such as Li or Be 'catches' the ions to generates neutrons by nuclear reactions. In this method, the ion acceleration target is like an ion 'pitcher' and the neutron converter is like an ion 'catcher' (Fig. 2.9).

The neutrons are generated via (p,n) and (d,n) nuclear reactions. The (d,n) reaction is one of the stripping reactions which was first described in 1950[62]. Due to the weak bond between neutron and proton in a deuteron. When an incident deuteron hits the nucleus, the proton in the deuteron is stripped by the coulomb barrier and combines with the target nucleus, while the residual neutron proceeds with most of its original momentum in almost its original direction (Fig. 2.10). So in the (d,n) reaction, the generated neutrons originate from deuterons instead of the catcher nucleus.

On the other hand, the (p,n) reaction is one kind of the spallation, in

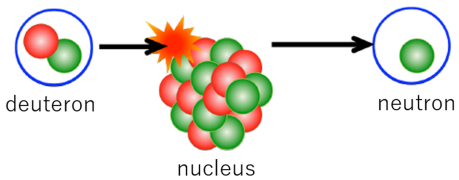


FIGURE 2.10: Deuteron stripping reaction

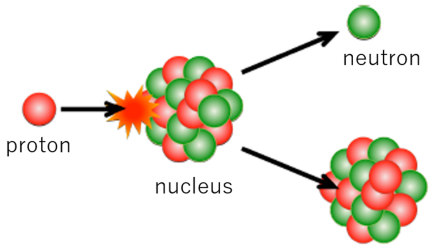


FIGURE 2.11: Proton induced reaction

which neutrons are ejected from target nucleus due to the impact of incident neutrons(Fig. 2.11). This reaction has fairly large cross-section and is capable of high neutron yield [63].

## 2.3 Neutron moderation

### 2.3.1 Method of neutron moderation

In almost all of neutron sources, the primary neutrons generally have high energy of ∼MeV, which is undesirable for neutron resonance measurement and other applications using low energy neutrons. This makes it necessary to 'slow down', namely, moderate the neutrons. A widely employed method is to use matters to block the neutron beam, so that the neutrons collide with atoms in the matters and loss their energy. As the consequence, the neutrons are moderated to lower energy. The matters used to moderate neutrons is called moderator. Since the slowing down process mainly relies on repeated elastic collisions, the main parameters involved in the moderation are:

- The mass of nucleus in the moderator: Energy-loss of neutron in one collision.
- Neutron scattering cross-section and number density of the moderator: Rate of collisions.

According to the theory of elastic collision, energy-loss per collision decreases as mass increases. Therefore, the lighter nuclei require fewer collisions to slow the neutron. As defined in [64], the mean logarithmic reduction of neutron energy per collision is

$$\xi = \ln \frac{E_0}{E} = 1 + \frac{(A-1)^2}{2A} \ln(\frac{A+1}{A-1}), \tag{2.20}$$

where the $E_0$, $E$ and $A$ are initial kinetic energy of the neutron, kinetic energy of the neutron after the collision and atomic mass of nucleus in the moderator. The $\xi$ represents fractional energy loss per collision of the neutron. As described in Ref[65], it can be approximated to

$$\xi \sim \frac{2}{A + 2/3}. \tag{2.21}$$

This indicates that an atom with smaller mass has higher moderation efficiency. For a few instances, Table 2.1 gives the moderation parameters of several isotopes. The number of collisions is that required to moderate a neutron with an initial energy of 2 MeV to a final energy of 1 eV.The materials with high hydrogen density are generally fast for moderation and can generate a slow neutron from fewer collisions. This is consistent with the inference of Eq.2.21.

| | Mass of kernels $\mu$ | Energy decrement $\xi$ | Collision times ($2MeV$ to $1eV$) |
|---|---|---|---|
| Hydrogen | 1 | 1 | 18 |
| Deuterium | 2 | 0.7261 | 25 |
| Beryllium | 9 | 0.2078 | 86 |
| Carbon | 12 | 0.1589 | 114 |
| Oxygen | 16 | 0.1209 | 150 |
| Uranium | 238 | 0.0084 | 2172 |

TABLE 2.1: Moderation parameters of various isotopes

There are several kinds of neutron moderators that have been demonstrated with appreciable efficiency of moderation[26, 66, 67]. In practice, it is also necessary to consider the factors such as the mean free path of neutrons, spontaneous release of energy and the neutron absorption cross-section[67]. Both the water and polyethylene have relatively high number density of hydrogen atoms. However, considering the strong absorption and long mean free path of water, in this study, the High-Density Polyethylene (HDPE) is used as the material of neutron moderators.

### 2.3.2 Development of neutron moderator

As introduced in Chapter1 Section1.1.3, the accuracy of TOF measurement depends on the pulse duration of the neutron source. When neutrons are moderated, the moderation makes neutrons of same energies to be generated

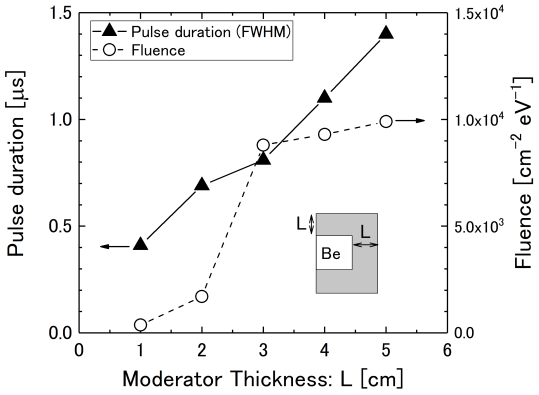


FIGURE 2.12: Neutron moderation of HDPE with various thickness

in a time window due to the collisions in the moderator. When using TOF method, the broadened neutron pulses cause errors in energy-time transform, finally produce error on the energy axis of NRS.

The moderator was optimized according to the balance between moderation efficiency and the duration of moderated neutrons. The simulations for low-energy (1∼10 eV) neutron yield and duration (FWHM of 10±0.1 eV) were calculated by *PHITS* code[68]. In the simulation, the detector was set at the rear surface of the moderator. The results are shown in Fig. 2.12. With the thickness increasing from 1 to 5 cm, the yield of neutron in 1∼10 eV region firstly goes up and flattens out at 3 cm. On the other hand, the duration increases almost linearly with the thickness, from 0.4 to 1.4 μs.

Therefore, considering both the performance of neutron yield and pulse duration, a moderator with thickness of 3 cm was designed for the experiments of NRS using LDNS [28]. The details are introduced in Chapter4.

## 2.4 Thomson parabola ion spectrometer

The accelerated ions are measured by a Thomson Parabola Ion Spectrometer (TPIS) with an Imaging Plate (IP). This section includes the method and configuration of TPIS, the feature and analysis of signal on IP.

### 2.4.1 The configuration of thomson parabola ion spectrometer

By applying an electrostatic field and a magneto-static field in parallel with each other, ions which incident can be accelerated according to mass and charge.

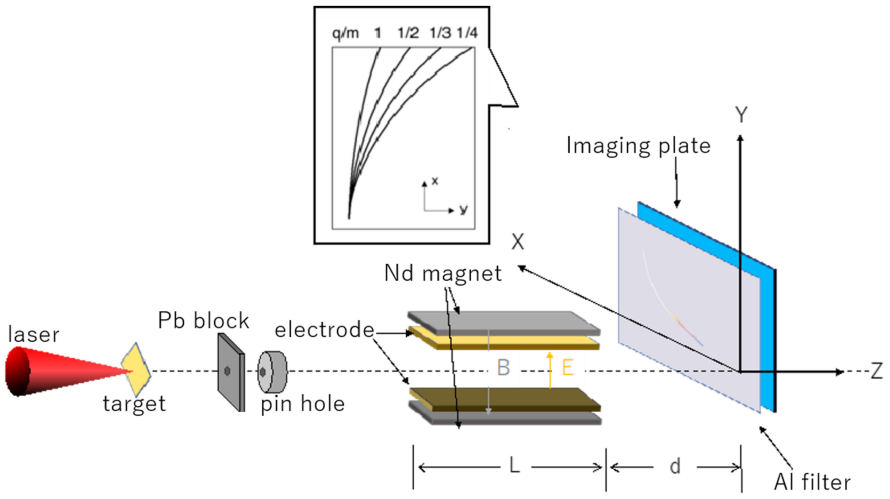


FIGURE 2.13: Diagram of TPIS

After traveling a certain distance, the accelerated ions hit different positions of a sensitive surface. Thus, the ion can be distinguished by energy and mass-to-charge ratio. Using this method, a TPIS can be designed to record the energy spectrum of different ions respectively (Fig. 2.13).

The neodymium magnets provide a magnetic field of 0.85 T. The electrodes are made with copper for low permeability. Two copper electrodes are placed 10 mm apart with a bias voltage of 15 kV applied. Ions are incident between the two electrodes through the pinhole, and then deflected by the electric and magnetic field, finally show a parabolic trajectory on the detective surface. In order to distinguish ion species that have same mass-to-charge ratio such as $C^{6+}$ and deuterons, 3 layers of aluminum filters with thickness of 300 μm, 100 μm and 50 μm respectively are attached to the upstream of detective surface. Thus, the $C^{6+}$ ions are completely stopped by the filter while a part of deuterons pass through. The IP developed by FUJIFILM is used as ion detective surface.

### 2.4.2 Imaging plate

The IP is produced by applying powder crystal phosphor of barium fluorobromide doped with divalent europium ($BaFBr : Eu^{2+}$) on a plastic film. The phosphor layer is specialized for the Photo-Stimulated Luminescence (PSL). It has a 1000 times higher sensitivity than that of ordinary X-ray films, with a wide dynamic range and high spatial resolution. The IP used in this study is BAS-TR2025 manufactured by FUJIFILM.

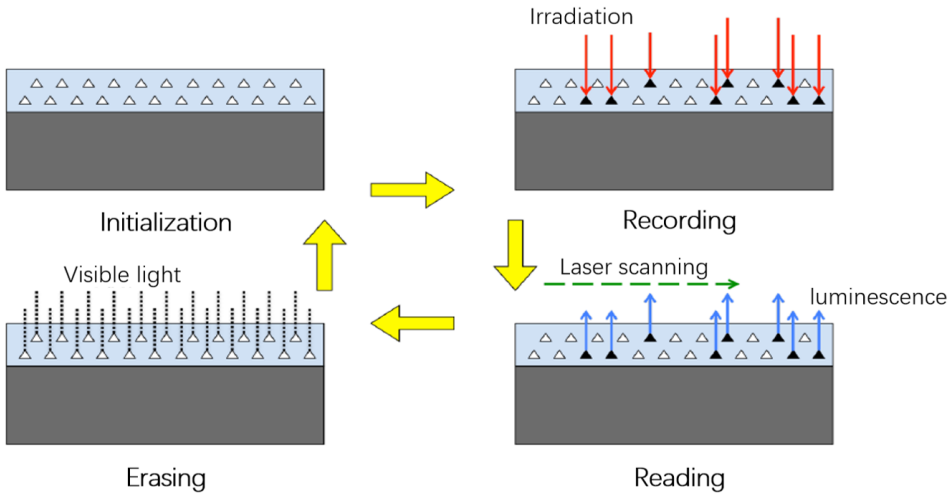


FIGURE 2.14: Recording and reading process of IP signal

The PSL is a process that stored energy produce a luminescent signal within a phosphor via stimulation with visible light. The process of signal recording and reading (Fig. 2.14, 2.15) can be expressed as:

- Recording (energy storage): After the initial exposure by original radiation, $Eu^{2+}$ ions lose an electron to become $Eu^{3+}$ ions. The excited electrons in the phosphor material are trapped by the lattice defects that originally existed in the crystal. In case of $BaFBr:Eu^{2+}$, the empty lattice of $F$ ion and $Br$ ion capture the excited electrons to form meta-stable color centers. Since the amount of trapped electrons is proportional to the irradiation dose, a 2D image of the irradiation is recorded.

- Reading (energy release): A lower-frequency light source that is insufficient in energy to create more $Eu^{3+}$ ions can return the trapped electrons to the conduction band. The $Eu^{3+}$ ions capture these electrons and rise to the excited state of the $Eu^{2+}$ ion. When the excited $Eu^{2+}$ ion returns to the ground state, a blue-violet $390nm$ luminescence is released. The light is produced in proportion to the number of trapped electrons, and thus in proportion to the original irradiation signal. The reading process is completed by a dedicated IP reader which can record the luminescence as a 2D image data. In this study, the Typhoon FLA7000 (Fig. 2.16) from GE Healthcare Japan is used as the IP reader.

Although the signal recorded on the IP can be stored for a long time, it has a drawback that the signal is fading with time due to thermal relaxation[69]. A calibration work was done by D. O. Golovin [70]. The fading function is given

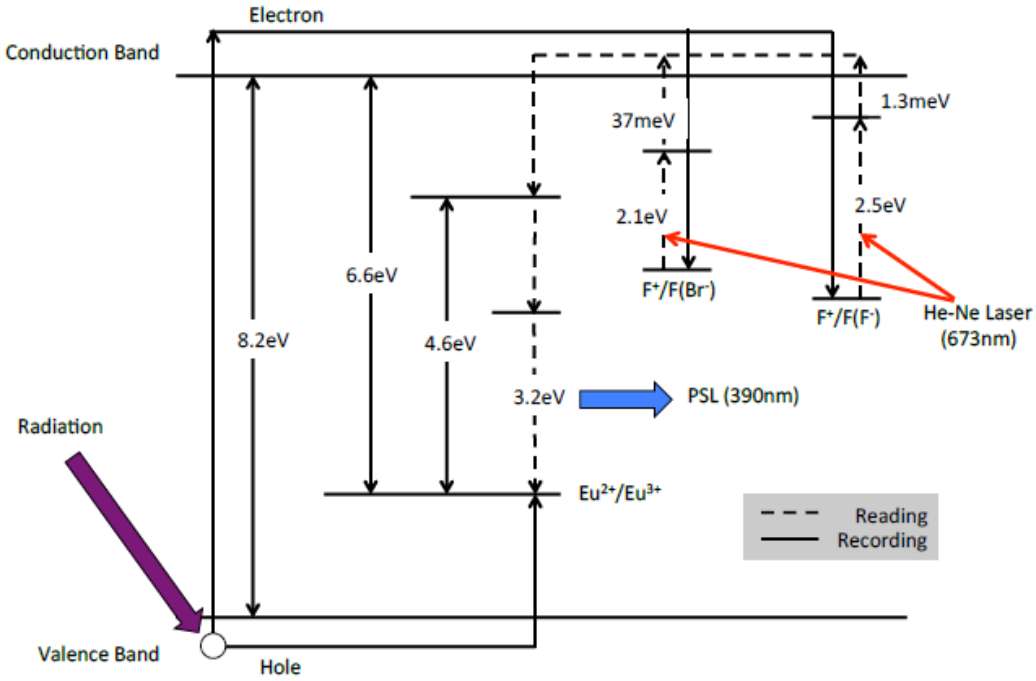


FIGURE 2.15: Energy levels in PSL process

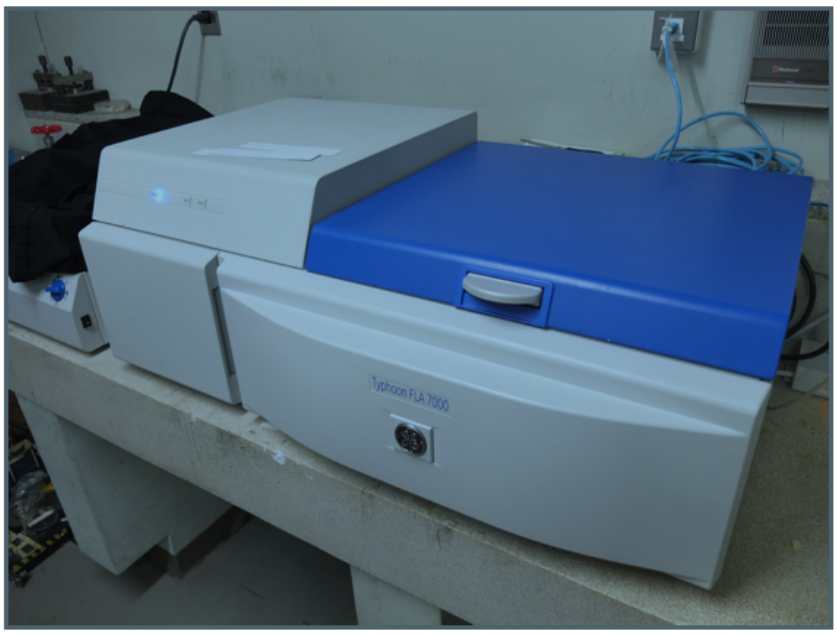


FIGURE 2.16: Typhoon FLA 7000

by

$$F(t) = PSL_t/PSL_0 = A_1 exp(\frac{-t}{B_1}) + A_2 exp(\frac{-t}{B_2}), \tag{2.22}$$

where $PSL_t/PSL_0$ is a relation between PSL value at time $t$ (given in minutes) and zero time. The parameters are:

$$A_1 = 0.3590, \quad B_1 = 33.227, \quad A_2 = 0.6404, \quad B_2 = 2041.2.$$

In addition to the fading, IP signal is also underestimate due to scanning efficiency. The signal from first scan cannot be fully resolved due to generation of many excited trapping centers inside the IP, which continuously deposit energy. This suggests that there is a dependency between the obtained PSL value and the number of the scans. To fix this problem, a function is given by

$$PSL^N/PSL^1 = C_1 exp(\frac{-N}{D_1}) + C_2 exp(\frac{-N}{D_2}), \tag{2.23}$$

where $PSL^N/PSL^1$ is the relation between PSL value for scan number $N$ and the first scan. The parameters are:

$$C_1 = 2.0084, \quad D_1 = 0.847, \quad C_2 = 0.4595, \quad D_2 = 5.4617.$$

When the number of scans is large enough, the signal $PSL^N$ will be negligible. Combine the function (2.22) and (2.23), a function for fixing time fading and scan efficiency can be written as

$$(\sum_N^1 PSL_t^N)/PSL_t^1 = 2.4143(t - 3.7213)^{0.0738}, \tag{2.24}$$

where $(\sum_N^1 PSL_t^N)/PSL_t^1$ is relation between total PSL value obtained during all multiple scan sequences and the first scan PSL value.

The calibration results from Ref. [70] are used to convert PSL to ion numbers. The function is given by

$$C_p = 0.137E^{-0.749}, \tag{2.25a}$$

$$C_d = 0.1298E^{-0.731}, \tag{2.25b}$$

where $C_p$ and $C_d$ are responses in PSL units per one incident proton and deuteron respectively and E is an incident ion energy per nucleon.

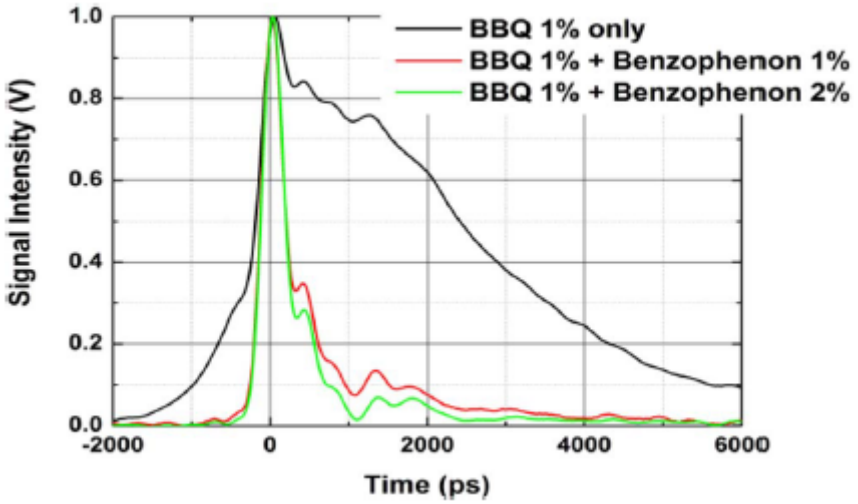


FIGURE 2.17: Light decays of benzophenone-doped BBQ liquid scintillator[71]

## 2.5 Neutron time-of-flight detectors

Due to the neutrality of neutrons, they cannot cause ionization or excitation of matter like charged particles, which makes neutrons difficult to be detected directly. And for the same reason, neutrons cannot use electromagnetic fields to distinguish the energy distribution. Instead of direct detection, charged particles or photons generated by the interaction between neutrons and medium materials are generally used to achieve indirect detection of neutrons. In this study, a customized liquid scintillator and $^{6}$Li-glass scintillator are used for neutron detectors.

### 2.5.1 Liquid scintillator for fast neutron detection

A customized liquid scintillator which developed by Y. Abe et al.[71] is used as medium materials for fast neutron detection. The single dye of BBQ $(4,4^{''''}-bis[(2-butyloctyl)oxy]-1,1^{'}:4^{'},1^{''}:4^{''},1^{''''}-quaterphenyl)$ has been reported to have fast time decay characteristics. The liquid solvent is $1,2,4\text{-}TMB(1,2,3trymethybenzene)$ which has been tested with the 1% BBQ and 2% benzophenone flour (Fig. 2.17). The results show this new liquid scintillator has a fast time response with negligible afterglow. The liquid scintillator container is coupled to a photomultiplier tube (PMT) (Thron EMI 9902KBT) which collects scintillation light and convert it into electrical signals. A high-speed oscilloscope is used to record the signal.

| Properties | GS2 | GS20* | KG2 |
|---|---|---|---|
| Density [g/cm³] | 2.64 | 2.5 | 2.42 |
| Coefficient of linear expansion/°C | 7.0x10⁻⁶ | 9.23x10⁻⁶ | 100 x 10⁻⁶ |
| Light output relative to anthracene* | 22-34% | 20-30% | 20% |
| Decay times†, neutron excitation, ns | none | 18, 57 & 98 | 18, 62 & 93 |
| Decay times†, alpha excitation, ns | 20, 48 & 88 | 16, 49 & 78 | 15, 45 & 56 |
| Decay times†, beta excitation, ns | 19, 57 & 103 | 20, 58 & 105 | 17, 51 & 96 |
| Alpha/beta ratio | | 0.23 | |
| Wavelength of emission max [nm] | 395 | 395 | 395 |
| Refractive index at emission maximum | 1.58 | 1.55 | 1.566 |
| Resolution on the thermal neutron "peak" obtained with moderated Po/Be neutrons | 13-22% | 15-28% | 20-30% |
| Peak/through ratio of above "peak" (range) | 15:1 - 40:1 | 10:1 - 40:1 | 10:1 -20:1 |

*Determined by thickness, increasing with decreasing thickness down to approximately 2mm
†Fast component, slow component and 90-10% respectively.

* GS20 is a registered trademark of Scintacor Ltd.

| Type | Isotopic Ratio | Total Lithium |
|---|---|---|
| GS1 | Natural | 2.4% |
| GS2 | 95% $^6$LI | 2.4% |
| GS3 | 99.99% $^7$LI | 2.4% |
| GS10 | Natural | 6.6% |
| GS20 | 95% $^6$LI | 6.6% |
| GS30 | 99.99% $^7$LI | 6.6% |
| KG1 | Natural | 7.5% |
| KG2 | 95% $^6$LI | 7.5% |
| KG3 | 99.99% $^7$LI | 7.5% |

FIGURE 2.18: $^6$Li-glass scintillator parameters provided by SAINT-GOBAIN

### 2.5.2 $^6$Li-glass scintillator for epithermal neutron detection

$^6$Li-glass is a scintillator specialized in low-energy neutron detection which is made by doping $^6$Li isotopes into cerium activated glass. Since early $^6$Li-glass was developed in 1960s[72], it has been widely used in the detection of low energy neutrons. In this study, Cerium activated lithium silicate glass scintillators (GS20, $\phi$=5.08 cm, t=1 cm) manufactured by Scintacor Ltd. were used for epithermal neutron ToF detector. Some parameters of GS20 is shown in Fig. 2.18.

When neutrons are incident on the scintillator, the following nuclear reaction will occur:

$$n + {}^6Li \Rightarrow T + {}^4He + 4.78\ MeV. \tag{2.26}$$

The reaction can be abbreviated as $^6$Li(n,t)$^4$He. With a large $Q$ value (4.78 MeV) of the reaction, two charged particles produced by the reaction excite the cerium ions in the scintillator glass to high energy levels. Then the cerium ions back to the ground state and emit 400 nm luminescence light (Fig. 2.19). GS20 has been investigated to prove that each neutron incident event can produce ∼6000 photons[73]. This bright scintillation can be clearly detected by the PMT.

Since the ions that generate scintillation are produced by nuclear reactions, compare to the $Q$ value (4.78 MeV) of the reaction, the kinetic energy of neutrons is negligible in low energy region (1∼100 eV) where resonances occur. Thus, the neutron detecting efficiency mainly depends on the cross-section. The

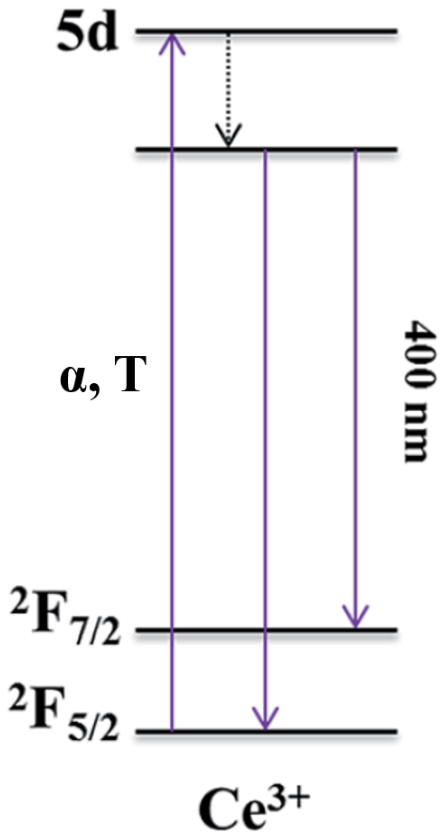


FIGURE 2.19: The schematic energy levels of $Ce^{3+}$[74]

cross-section of $^{6}$Li(n,t)$^{4}$He reaction has been accurately measured and evaluated[75]. Since the thickness of GS20 glass is t=1 cm, the probability of reaction can be calculated by formula (Equ. 1.3) using the nuclear data (Fig. 2.20) evaluated by JENDL4.0 database [76]. The calculated result of neutron detecting efficiency is shown in Fig. 2.21.

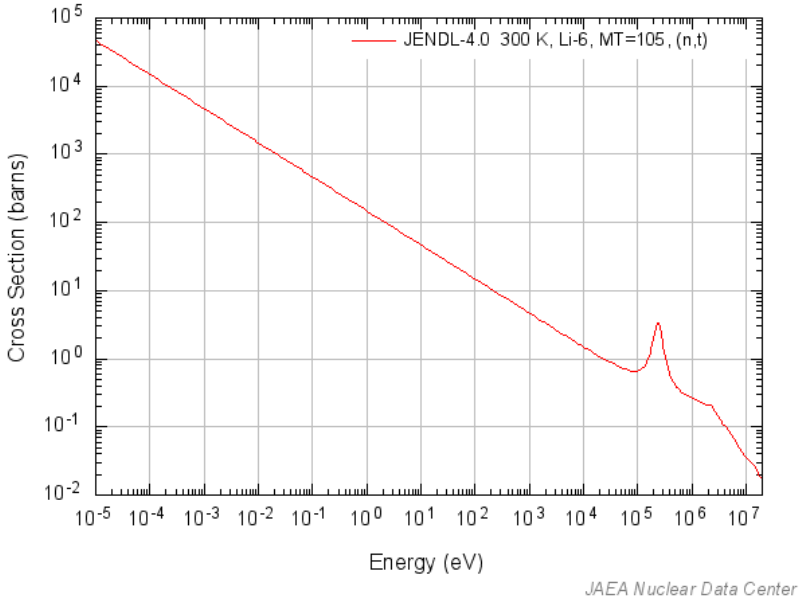


FIGURE 2.20: Cross-sectoin of $^{6}$Li(n,t)$^{4}$He reaction[76]

In the intense X-ray environment of high-power laser facility, the PMT that is coupled with the scintillator may easily saturated during all of the neutron incident events. A customized time-gated PMT is coupled with the GS20 glass for scintillation collecting and recording. With the electrical time-gating (ETG) system, the laser generated X-ray background which is 4-5 orders of magnitude stronger than neutron events is effectively suppressed. The details of time-gated PMT is introduced in Chapter3.

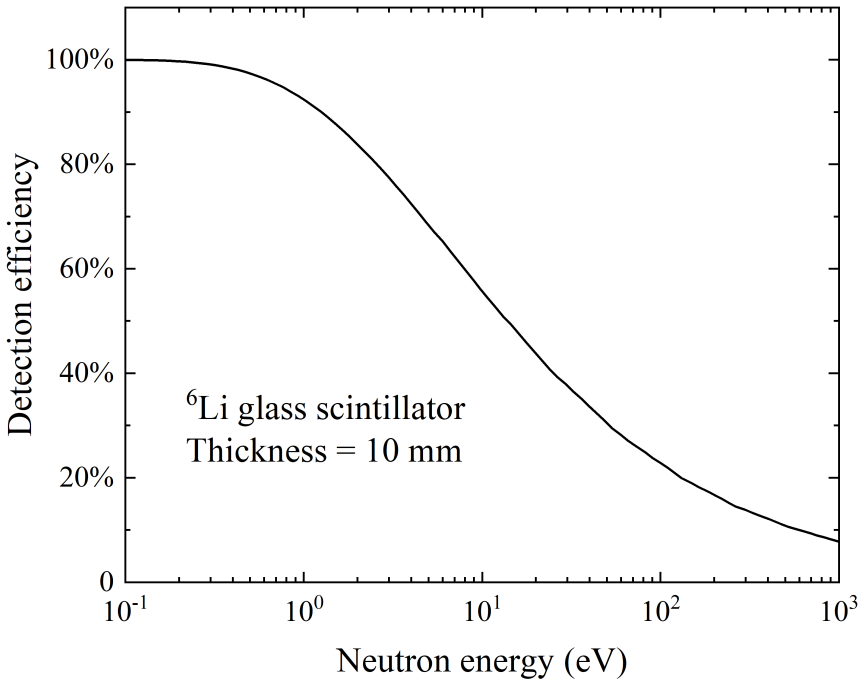


FIGURE 2.21: Neutron detecting efficiency of GS20

# Chapter 3

# Development of Time-gated Neutron Detector and Beamline

## 3.1 Problems of time-of-flight neutron detection in high-power laser experiments

In a typical neutron TOF spectroscopy, scintillator coupled with a photomultiplier tube (PMT) is used to record the neutron signals. A typical construction of PMT is shown in Fig. 3.1 [77]. The light signal is converted into electrons by photoelectric effect at the cathode. Then photoelectrons are reflected and multiplied by the subsequent dynodes. The anode collects all the photoelectrons and outputs a current signal corresponding to the incident light. The multiplication of a PMT has limitation due to the driver circuit of the PMT. In the driver circuit, the voltages of dynodes are divided by voltage divider resistors in series (Fig. 3.2 [77]). When the photoelectrons are reflected and multiplied by dynodes, the reverse current ($I_{Dy}$) flows into the circuit through the surfaces of dynodes. The potentials of dynodes are reduced due to the $I_{Dy}$, leading to

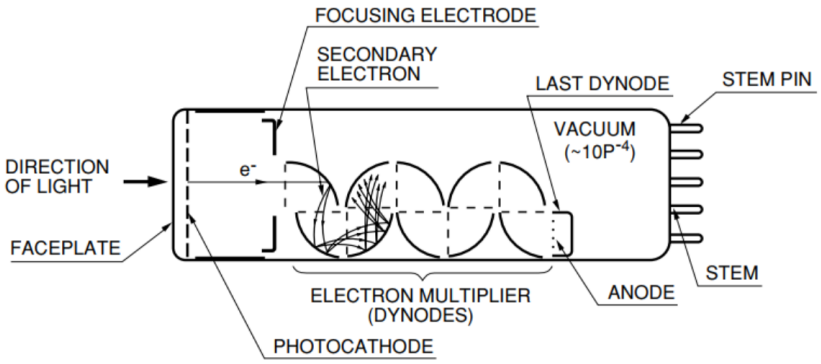


FIGURE 3.1: Construction of a photomultiplier tube [77]

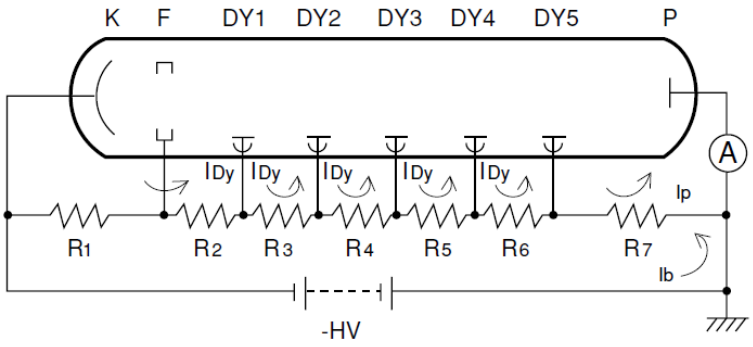


(a) Driver circuit of PMT.

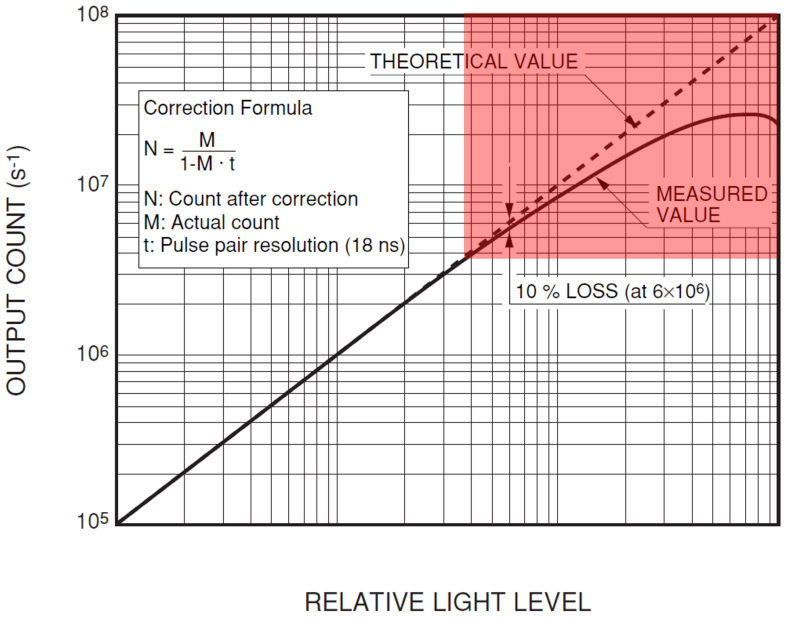


(b) The output of PMT with relative input light level. The linearity of response changes when the light level is too high (red region). [77]

FIGURE 3.2

the changing of gain of multipliers. As a result, an overloaded signal causes the response of PMT to lose linearity (red region in Fig. 3.2(b)). Although, the response linearity can recover for the later incident signals, the recovery times are typically in microsecond range.

For the neutron TOF detection, the arrival time of neutrons is generally ns$\sim$ μs later than X-ray backgrounds. Therefore, if the X-ray background is so intense that it overloads the PMT, the subsequently arriving neutron signals could be effected by the X-rays. In high-energy laser-driven neutron experiments, one of the major hindrances to neutron's measurement is that all reactions, including laser-induced ion acceleration and neutron generation,

release large amounts of energy in the form of intense hard X-rays [44]. As introduced above, the X-rays reach the detector before other particles in the TOF method. However, the effects only need to be considered for epithermal or lower energy neutrons while can be ignored in fast neutron detection.

In fast neutron (with an energy of tens MeV) measurements, the flight distance is restricted to more than tens of metres to provide a long flight time that keeps the neutron signal separated from the X-ray peak [28, 31, 32, 40]. The high yield of fast neutrons (~$10^{10}$/sr) make the statistics are enough to give a entire spectrum even with a long beamline of tens of metres. At that distance, the smaller solid angle allows less signals to enter the detector. Furthermore, a thick lead shield can be set in the beamline to reduce the X-rays efficiently, while the fast neutrons are less affected due to the higher transmittance.

As introduced in Chapter 2, the yield of thermal neutrons is relatively limited for the short pulse. Since the propose of this research is to realize single-shot NRS, a short beamline is required for an enough statistics at the detector. For the epithermal neutrons, the intense X-ray generated by the laser shot could be separated in times even with a beamline shorter than 2 m, due to the ultra-short pulse of eV energy neutrons in 100s ns. However, the bigger solid angle of the short beamline also enhances the X-rays signal in detectors. At about 2 m distance, the PMT can be easily overloaded by X-rays. Due to the low energies of epithermal neutrons, the thick shield for X-rays such as lead can not be used. A lead shield that is thick enough to block X-rays to protect PMT from overload also reduces the number of epithermal neutrons, leading to insufficient statistics in the spectrum. According to the above conditions, the temporally separated X-ray signals can still effect the subsequent detection of epithermal neutron signal in 10s of μs later, and suppressing the X-rays by changing the beamline setup is not feasible.

## 3.2 Development of time-gated photomultiplier driver circuit

### 3.2.1 Necessity and purpose of the development

To cut off the X-ray background signal, some time-gated neutron detectors have been developed [78–80] for neutron detection. A customized electrical

time-gating (ETG) system has been coupled with a PMT to stop the multiplication of electrons during a specific period by applying a reverse bias on the dynodes of the PMT [81–84]. Although PMTs with ETG systems have been developed for a long time and there are commercial modules providing ETG functions, few products are suitable for high-energy laser-driven neutron experiments. The overload current of the X-ray signal usually disables the commercial ETG circuit. Furthermore, there is another problem. Most models available for sale provide only relatively small photosensitive surfaces ($\phi < 1$ cm), while detecting laser-driven neutrons requires bigger scintillators ($\phi > 2$ cm) for higher statistics. Therefore, commercial modules are not feasible for laser-driven neutron experiments.

For a time-gated PMT with an ETG system, the bias voltage is generally delivered by a capacitor. The charging time of the capacitor determines the speed of the switch. However, for high-energy laser experiments, the capacitor may be completely discharged very quickly, causing the ETG to shut down earlier than the set time. As reported in [80], a high-speed ETG can provide a switching time of less than 100 ns by using a 10 nF capacitor. This design enables the detection of fast neutrons in high-energy laser experiments. However, for low-energy neutrons, the time length of the signal can be hundreds of μs or several ms. The capacitance is unable to maintain such a long-time switch and is discharged in approximately 10 μs. A gated PMT with an ETG circuit that is normally ON may be a solution for this problem. Previous research [83] has reported that switching the dynodes at the cathode end of a tube (K, Dy1 and Dy2) can result in a higher cut-off ratio and less interference on the normal response. However, for the present purpose, time-gating by switching the K bias is not feasible for the PMT due to the slow response time (>100 μs) of the semi-transparent bialkali photocathode.

In this study, the author developed a customized time-gated neutron TOF detector with a high cut-off ratio for the time gate, a large tolerance for the load current and the ability to maintain linearity throughout long time measurements[85]. The cut-off ratio refers to the electron gain of the PMT between the ON and OFF states, which is controlled by the ETG system. The author designed a gated PMT with an ETG circuit that is normally ON. The normally ON ETG can maintain the PMT in a normal working response and shut down when there is no control pulse input and a square pulse, respectively. With this design, transient shut downs are needed only in a very short period of several

µs during a laser shot. The normally ON ETG ensures an unlimited length of measuring time. The fast-switching gate and high cut-off ratio allow measurements in high-energy laser experiments with intense background and noise levels.

### 3.2.2 Design of a photomultiplier driver circuit with an electrical time-gating system

The PMT used for time-gated development is an 8-stage linear focused type HAMAMATSU-R2083, which provides a 46 mm diameter effective area of a bialkali photocathode and an anode pulse rise time of 0.7 ns. A diagram of the structure is shown in Fig.3.3. There is a focusing grid (G) and an accelerator electrode (ACC) between the photocathode (K) and dynodes (Dy n, n = 1,2,3...) to increase the collection rate and reduce the photoelectron transit time [86]. The multiplication of electrons is dominated by the voltage of the dynodes. The electrons are guided by the potential difference between the dynodes, reflected stage by stage and finally collected to output a current signal by the anode.

To realize a normally ON gate, a voltage dividing circuit is designed for dynodes and an ETG subcircuit is added on Dy1 to reverse the bias between Dy1 and Dy2 during the high-level gate-control signal. The voltage-dividing circuit and ETG subcircuit are shown in Figs. 3.4(a) and 3.4(b). The voltage-dividing circuit is the main circuit of the PMT and is powered by a high voltage of -1400 V. Therefore, the potential of each dynode increases stage by stage from Dy1 to Dy8 to ensure that the electrons can be accelerated between the dynodes. The

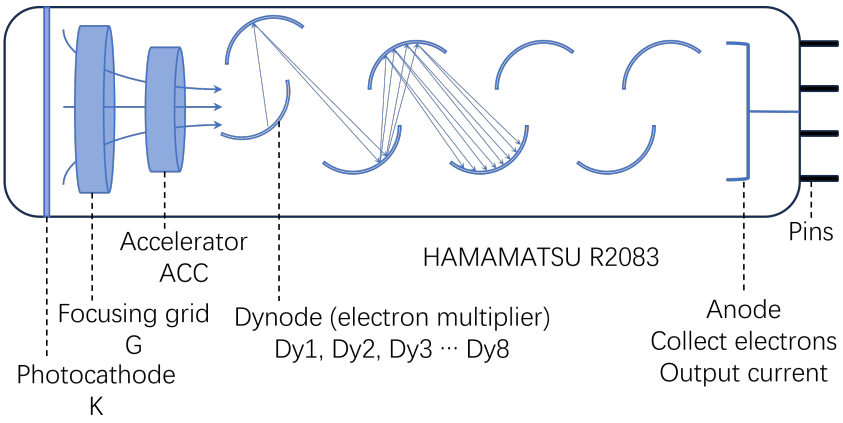


FIGURE 3.3: R2083 manufactured by HAMAMATSU Photonics

capacitors connected in parallel with the resistors in the last stages stabilize the voltages to maintain linearity when the large number of electrons hitting on the dynodes cause reverse currents [87]. Dy1 is connected to an independent parallel branch separately, which supplies a potential. The ETG sub-circuit, which is named HV Pulser and depicted in Fig. 3.4(b), is also connected to Dy1 through capacitor C15. HV Pulser IO1-4 is connected to a +360 V high-voltage power source with an output to capacitor C15, a 4 V TTL control pulse signal input and the electrical ground. The control signal is input to a gate driver, UCC27517DBVR, which drives an N-channel high-voltage MOSFET to generate a square pulse of 360 V.

### 3.2.3 Test for temporal characteristic of the electrical time-gating circuit

The expected temporal characteristic of the gated PMT is shown in Fig. 3.5(a). When a +4 V TTL signal is delivered to the HV Pulser, a square pulse of +360 V is generated and delivered to Dy1 through C15. The potential of Dy1 increases by 360 V, making it 10 V higher than the potential of Dy2. Therefore, the bias between Dy1 and Dy2 is reversed to prevent the electrons from reaching Dy2. Thus, the gate is OFF and the gain of the PMT is theoretically close to 0. In the normal state, the Dy1 potential is lower than that of Dy2. The electrons are accelerated to Dy2, multiplied in the subsequent stages and finally output as a current signal from the anode.

The temporal performance of the gated PMT was tested with an LED light in a darkroom, and the test results are shown in Fig. 3.5(b). The gate control signal, DC power to the LED and PMT output signal were recorded by an oscilloscope. The gate control signal was a TTL pulse generated by a digital pulse generator (DG535), as shown by the black line. The LED light was powered by a DC pulse output of DG535, as shown by the red line. The level of the input gate control signal changed during the period when the LED was glowing. The response signal of the gated PMT was recorded and is represented by the blue line. Before the gate control signal changed to a low level, although there was incident light from the LED, the response signal of the PMT was zero. When the gate control signal changed to a low level, the gain of the PMT was restored, and the response signal was output. An enlarged figure of the lower edge of the gated control signal is shown on the left of Fig. 3.5(b). Here, we defined two parameters to evaluate the time performance of the gated PMT:

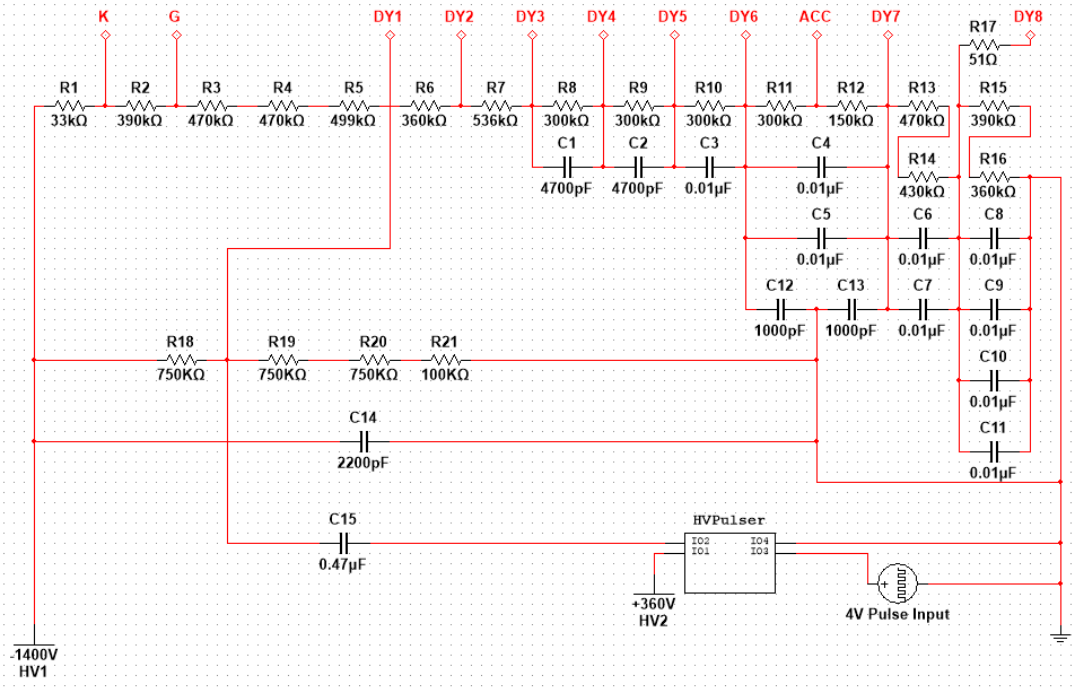


(a) Main circuit of the gated PMT[85].

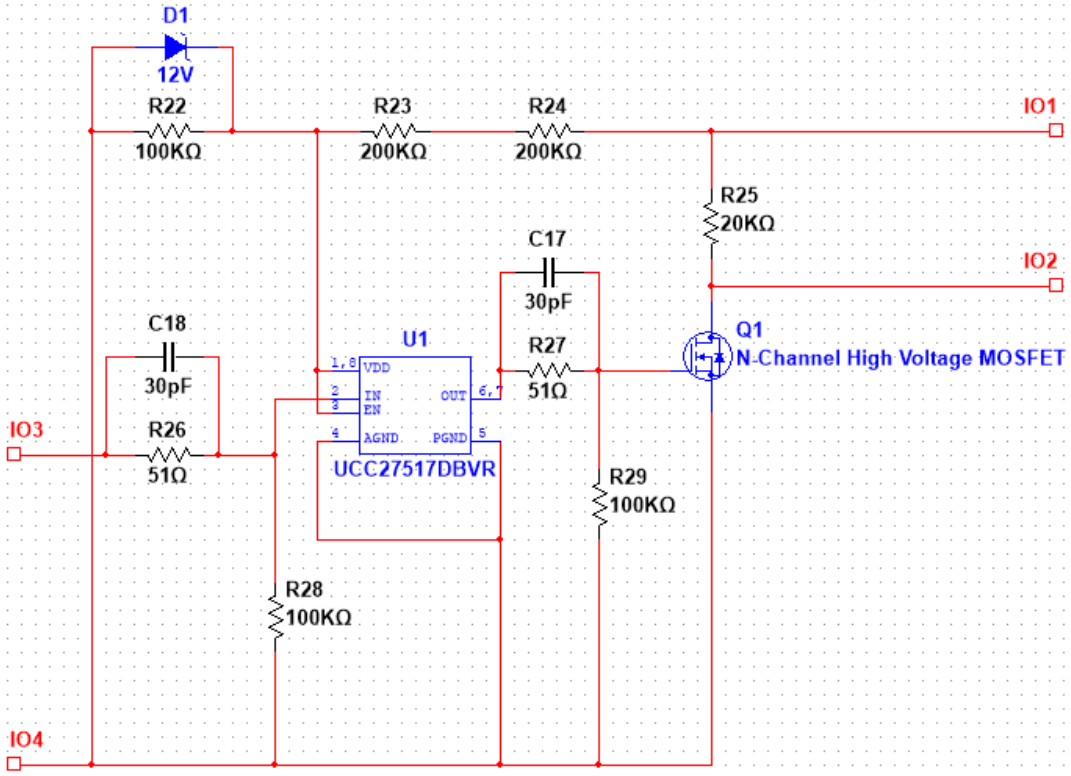


(b) The ETG subcircuit (HV Pulser) is connected to the main circuit[85].

FIGURE 3.4

the transit time and the raising time. The transit time represents the time from the start of the low edge of the gate signal to the start of the high edge of the gain. The rising time is the gain of the gated PMT from 0 to the maximum. These two delays are generated by the internal delay of the MOSFET and the gate driver chip. The transit time and raising time were determined to be approximately 170 ns and 400 ns, respectively. In practical operation, the transit time can be offset by adjusting the gate signal time. The gain of the gated PMT was calibrated by a typical HAMAMATSU H2431-50 PMT module with LED light. By comparing the output signal levels of H2431-50 and gated PMT, we evaluated the gain of gated PMT to be $8 \times 10^4$ during the ON period.

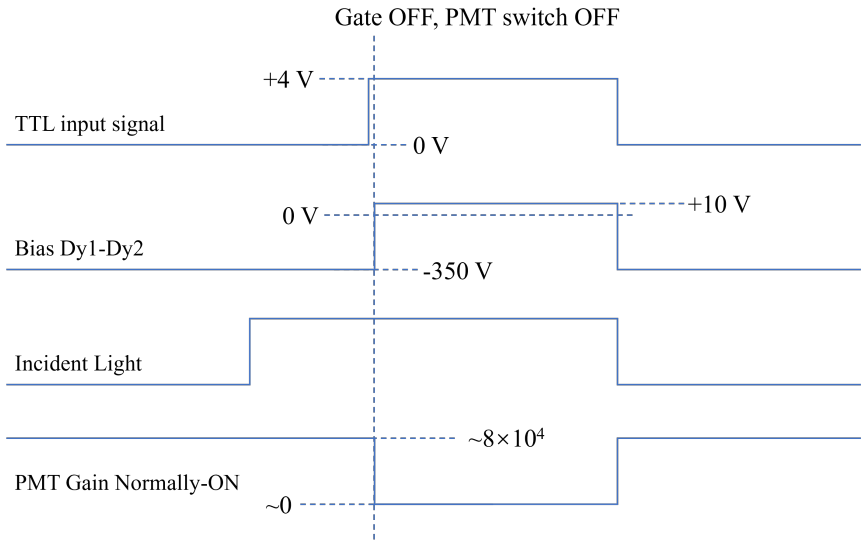


(a) Time line of the TTL input signal, bias of Dy1-Dy2, incident light and gain of the PMT[85].

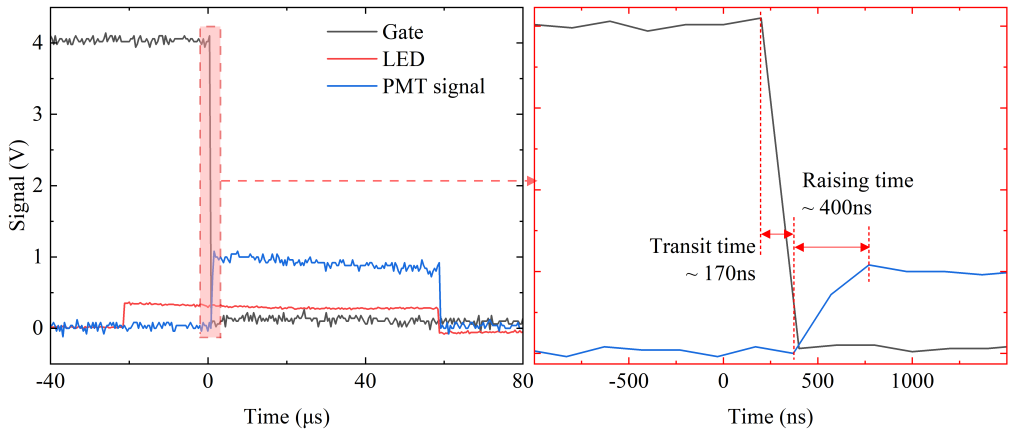


(b) The response test of the gated PMT[85].

FIGURE 3.5

### 3.2.4 Test for time-gated photomultiplier tube in high-power laser experiments

To verify the feasibility of the gated TOF detector in high-energy laser experiments, we implemented test laser shots using LFEX Laser for Fusion Experiments), the high-power laser facility of Osaka Univ. The experimental setup is shown in Fig. 3.6. The 4 laser beams of LFEX were focused on a 5 μm thick deuterated polystyrene (CD) foil target with an intensity of $\sim 1 \times 10^{19}$ W·cm$^{-2}$, an energy of 1300 J and a 1.5 ps pulse duration [28]. A secondary target of cylindrical Be with high-density polyethylene (HDPE) was placed 5 mm downstream of the CD foil, resulting in the generation of fast neutrons and slower neutrons in the energy region of eV, respectively. The gated PMT was coupled with a $^6$Li glass scintillator (GS20, Scintacor Ltd., 10 mm in thickness, 25.4 mm in radius). The neutron-induced nuclear reaction of $^6$Li(n,T)α provides a large cross section in the low-energy region, which contributes to the high efficiency of neutron detection. The detection efficiency was calculated from the $^6$Li(n,T)α cross section data obtained from the JENDL4.0 database [76], considering the weight proportion and fraction of $^6$Li in the GS20 scintillator [88]. According to the calculation (Fig. 2.21), a $^6$Li glass scintillator with a thickness of 10 mm can provide approximately 20%∼90% detection efficiency in the 1∼100 eV energy region. The GS20 scintillator was combined with the photosensitive interface of the PMT with a silicon optical glue. This scintillation detector was used as a gated TOF detector at 1.8 m from the CD target. An aluminium flange on the laser chamber was installed to provide a high transmittance of epithermal neutrons along the beamline. No collimator or shield was set around the beamline to evaluate the influence of background.

To evaluate the X-ray cut-off of the gated TOF detector, the neutron generator and the moderator were removed for the test shots, while the rest of the setup was retained. The gate-off time window was set from 1 μs before the laser shot to 1 μs after the laser shot. The signal of the X-rays induced by the laser incident on the CD foil target was observed in the gated TOF response signal (the enlarged part in Fig. 3.7) regardless of the cut-off. This was attributed to the direct irradiation of the X-rays on the secondary and subsequent dynodes in the PMT. The ionization of the residual gas in the PMT further generated electrons. The direct irradiation-induced X-ray signal was acceptable when it was within the tolerance of the PMT. When the ETG system was switched ON, the PMT output noise signals, including residual X-rays and scattered neutrons, as

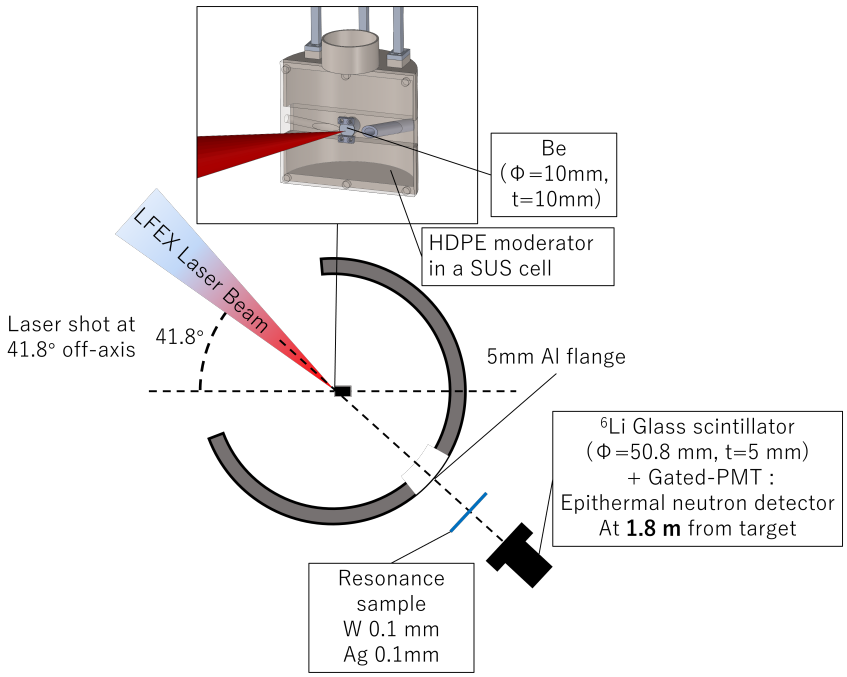


FIGURE 3.6: Laser-driven neutron experimental setup[85].

discrete pulses after 1.5 μs (Fig. 3.7). For epithermal neutrons with energy of hundreds of eV, the most applied scintillator 6Li glass generated approximately 6000 photons for every neutron incidence event [89]. Considering the gain of the gated TOF detector, we estimated the response signal level of a neutron to be 10∼100 mV. The signal level was consistent with the pulse height in the test signal (Fig. 3.7), suggesting that some background (scattering neutrons and X-rays) was detected in the CD shots. The results of the test experiments showed an effective cut-off of the X-ray signals, while some background neutrons were detected after the gate switch was ON.

This design of time-gated PMT was used in the experimental epithermal neutron measurement, and the single-shot NRS was realized for the first time. Detailed results are introduced in Chapter4.

## 3.3 Development of epithermal neutron beamline for laser-driven neutron source

### 3.3.1 Necessity and purpose of the development

As introduced in Chapter2, the epithermal neutron yield of moderated LDNS is limited for a short pulse (< 1 μs at ~1 eV). Meanwhile, there are

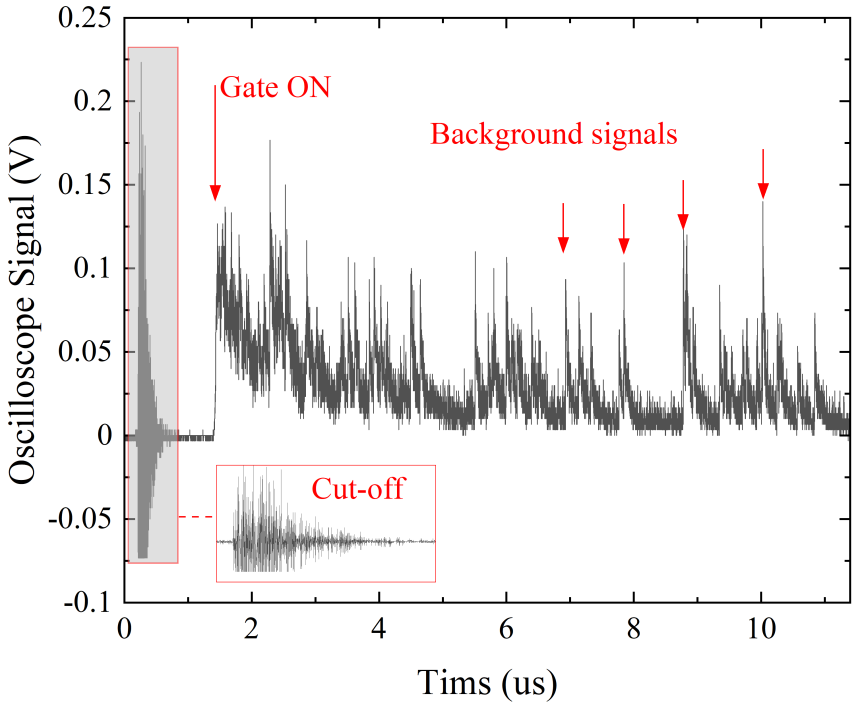


FIGURE 3.7: The response signal of a gated-PMT in a CD shot without Be or HDPE[85].

backgrounds of neutrons and X-rays which are scattered from the laser chamber and other constructions. These backgrounds generally produce response signal much higher than the desired epithermal neutron signals and arrive the TOF detector in a long time window including desired signals' timing due to the random scattering. Although the backgrounds can not be blocked by time-gated PMT, a neutron collimator and a shield around beamline are effective approaches of improvement.

The purpose of the development is to improve the S/N ratio of epithermal neutron signals. By optimizing the designs of collimator and shield, the statistics of neutron spectrum can be improved and the backgrounds can be suppressed. A smoother neutron spectrum provides more information in the details of resonance peaks, which is important for the investigation of temperature dependency of NRS.

The developments of a Nickle epithermal neutron collimator and a Boron-doped Polyethylene shield are introduced in this section.

### 3.3.2 The development of nickle epithermal neutron collimator

Nickle has high cross sections of neutron elastic scattering and small cross sections for absorption and other reactions. So far, many neutron experiments have used the nickle as the material of neutron reflector or neutron supermirror [90–92]. It is need to note that, the 'reflector' and 'mirror' refer to the elastic scattering rather than the specular reflection such as optical behaviors. In previous works, the interests are most focused on the critical angle that depends on the neutron wavelength.

In this research, an tube made by Ni-0 (natural) is designed as a neutron collimator, taking the advantage of high elastic scattering cross section. As shown in Fig. 3.8, the cross section shows a platform of about 20 barn in mev ~KeV where is the energy region of epithermal and thermal neutrons.

The thickness of tube can be optimized to select the neutron by incident angle on the nickle (Fig. 3.9). Fig. 3.9(a) shows the mechanism of neutron collimation. When neutrons incident into the nickle surface, the pass length of neutrons are depends on the incident angle (as $\theta$ in the Fig. 3.9(a)). With a bigger incident angle, neutrons have less probability to occur elastic scattering

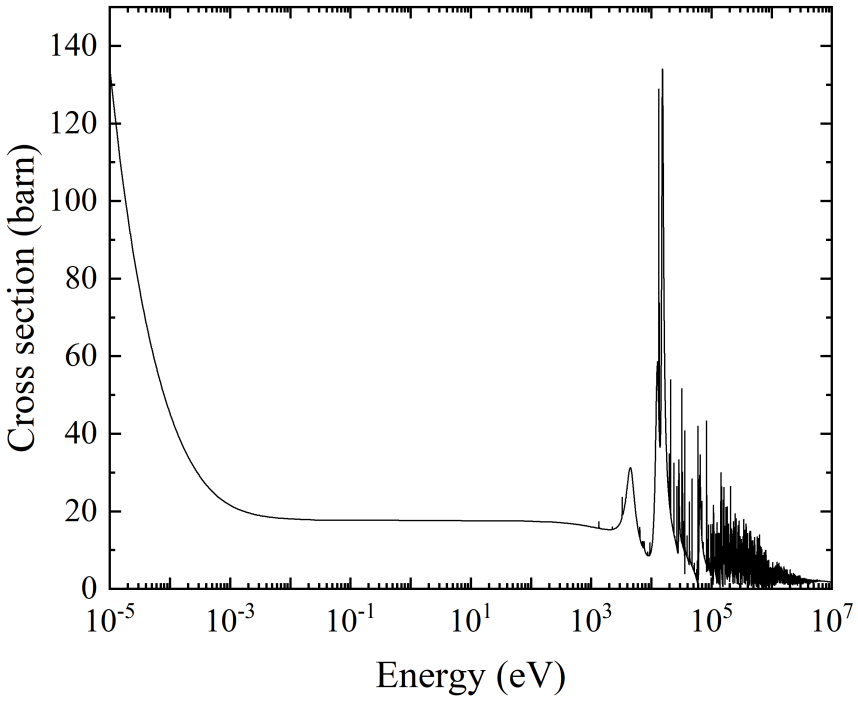


FIGURE 3.8: The cross section of neutron elastic scattering in Ni-0 [76].

so that most of them go through the nickle wall. For neutrons incident with a smaller angle, relatively longer pass length make them easier to be scattered. If the scattered neutrons towards a direction close to the center axis of beamline, the neutrons will repeat the scattering or directly arrive the detector. In the case where neutrons arrive at the detector after multiple scatterings, the small scattering angles and less scatterings can ensure that the time broadening caused by different flight distances is negligible compared to the source pulse width. By this design, the epithermal neutrons can be focused along the beamline to increase the detected statistics. Fig. 3.9(b) shows the calculated reaction rate changing with angles of incident neutrons. The neutron energy is assumed as 5 eV that most of individual resonance peaks exist. When neutrons incident vertically ($\theta = 90°$), there is about 20% probability of scattering. With the $\theta$ decreases, scattering rate increases exponentially. The optimization of nickle thickness is considered with the length of the beamline and the effective surface of the detector. With 1.8 m beamline and detector surface of $\phi$ =2.54 cm, 2 mm thickness nickle is considered as the optimized design and provides 100% scattering rate under 10°.

A simulation of designed nickle tube was calculated by PHITS [68]. The fast neutrons of LDNS was used as input source. The neutron moderator was same as the optimized design in Chapter2. The recorded neutrons were 5 eV during the simulation. As shown in Fig. 3.10(a), a 45 cm nickle tube with thickness of 2 mm was set at downstream of the neutron moderator. The 2D result shown that the 5eV neutron flux inside the nickle tube was much higher than out side. To confirm the collimation efficiency and the affect on neuron pulse duration, a reference simulation was calculated with the same setup except the nickle tube. The neutron pulse duration (FWHM) at 5 eV is 0.88 μs with the collimation of the nickle tube. Compared with the reference case (0.75 μs), the nickle tube broadened the neutron pulse by 0.13 μs. In the simulation, the energy window of recording is set to be 5±0.05 eV. This thickness of the energy window also contributes to the broadening of pulse duration due to the distance (45 cm) between detector and neutron source. In the real experiments, the energy resolution should be considered by a mono-energy neutron pulse as introduced in Chapter2.

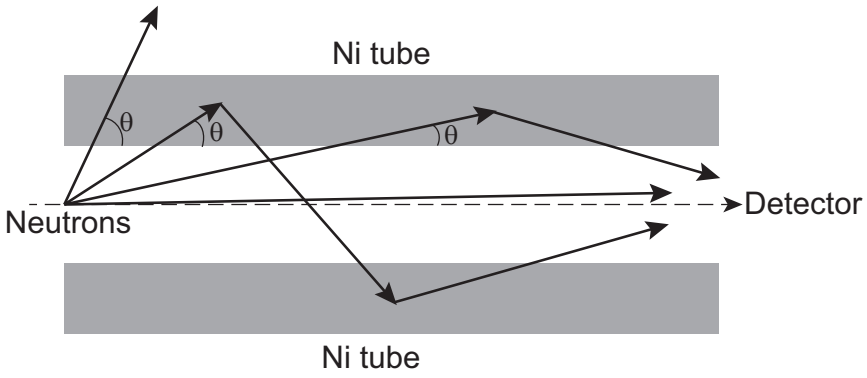


(a) The schematic diagram of nickle collimator.

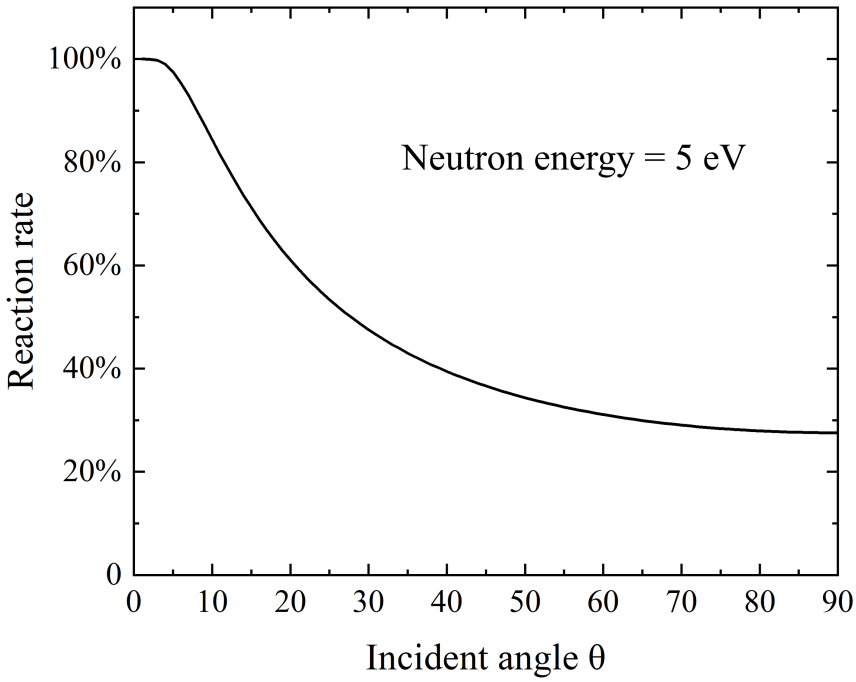


(b) The reaction rate of 5eV neutrons elastic scattering changes with incident angles.

FIGURE 3.9

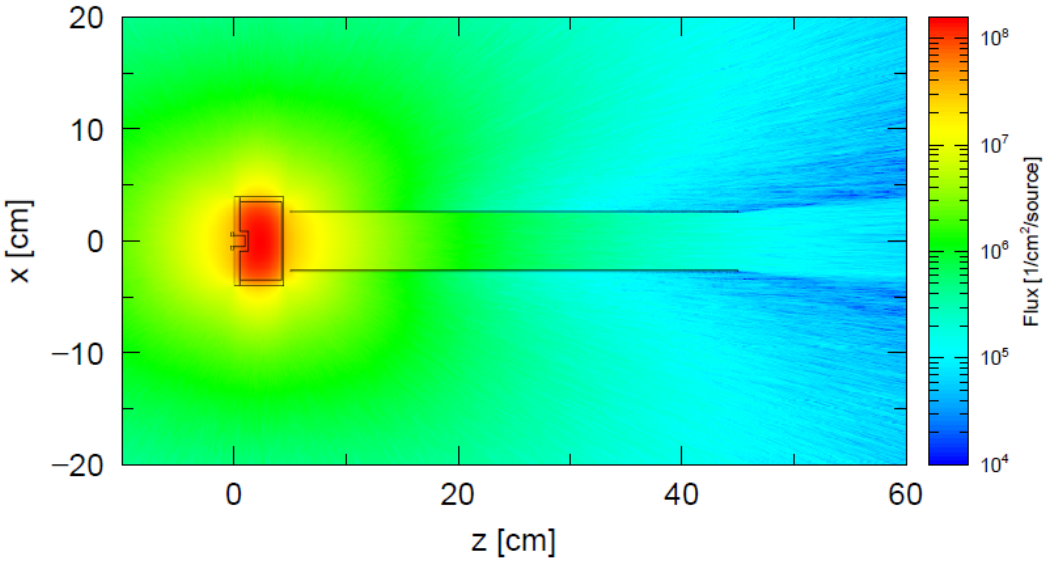


(a) The 2D result of simulated neutron collimation by using a nickle tube (L = 45 cm, t = 2 mm). The neutrons with 5 eV energy were recorded duration the simulation.

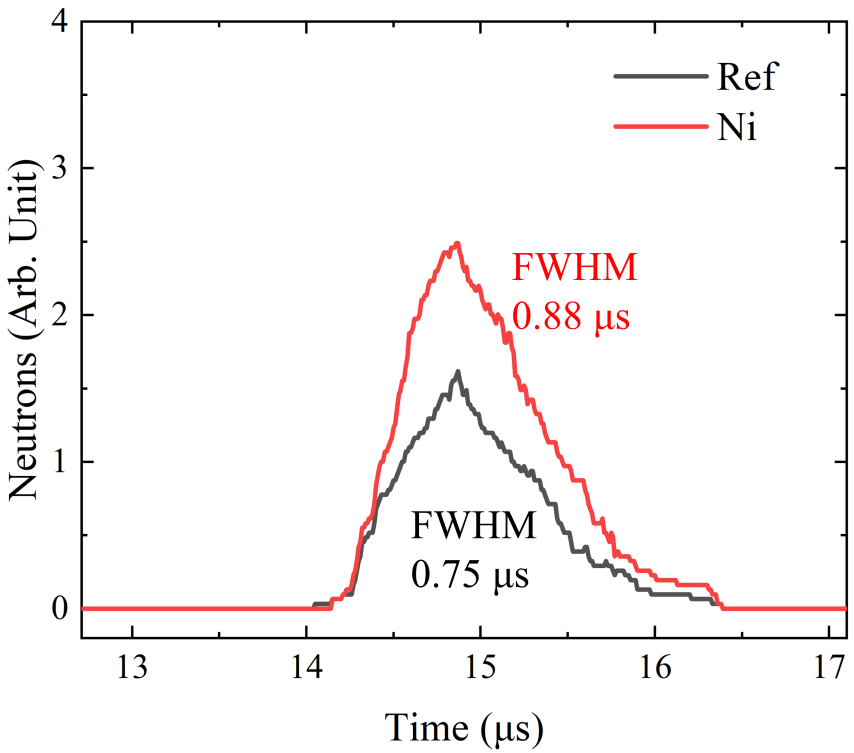


(b) The time duration of 5 eV neutrons on the exit of nickle tube. The red line is the 5eV neutron pulse at exit of the nickle tube. The black line is a reference result with the same setup except the nickle tube.

FIGURE 3.10

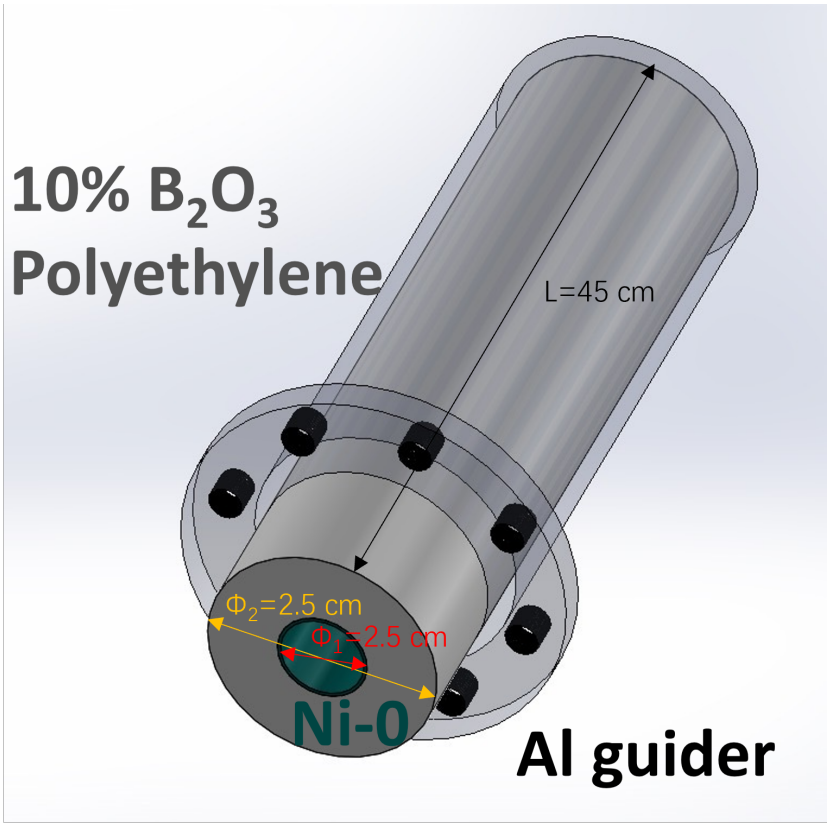


FIGURE 3.11: The structure diagram of neutron collimator used in LDNS experiments.

### 3.3.3 The design of background shield

To block the background neutrons which are scattered by the laser chamber and other structures, a shield sleeve was set on the out side of the nickle tube (Fig.3.12). The sleeve was made by polyethylene which doped by 10% $B_2O_3$. The high hydrogen content of polyethylene can scatter neutrons and slow them down to thermal neutrons. Boron is a widely used thermal neutron absorber due to the large absorption cross-section. All parts of the collimator are loaded by a Al guider which is installed on the laser chamber. Al has very small neutron cross-sections to provide a minimal interference on the neutron beamline. The experimental setup of the neutron beamline is introduced in Chapter 5.

### 3.3.4 The experimental demonstration of the beamline development

The NRS experimental results show the effectiveness of beamline development. The resonance peaks of $^{109}$Ag at 5.19 eV and $^{181}$Ta at 4.28 eV are used

for check neutron signal level. The thickness of resonance samples is adjusted to absorb 100% neutrons at the resonance peaks. Therefore, the depths of the troughs are equal to the level of the neutron signal. Fig. 3.12(a) is the signal measured without any collimator and shield, while Fig. 3.12(b) is the signal measured with neutron collimator as the design shown in Fig. 3.11. A same detector is used in the two cases with exactly same setup. The evaluated parameter is S/N ratio which is defined by the ratio of signal and noise level (rest part of signal except neutrons). The depth of resonance peaks is estimated by a fitted base line of the signals. The signals in Fig. 3.12 indicates that developed beamline with the neutron collimator improve S/N ratio from 9.8% to 18.7%. This is a important improvement that make more detailed investigation of resonance peaks becomes possible by using single-shot of LDNS. As an instance, The results of temperature dependency of neutron resonance are introduced in Chapter5.

The development of neutron collimator and shield introduced in this section has potential to improve and can be flexibly applied to different experimental purposes of LDNS. For example, the thickness and length of nickle layer can be adjusted to selectively collimate neutrons in a specific energy region. Furthermore, multi-material layers can be developed for more complicated and effective neutron collimation.

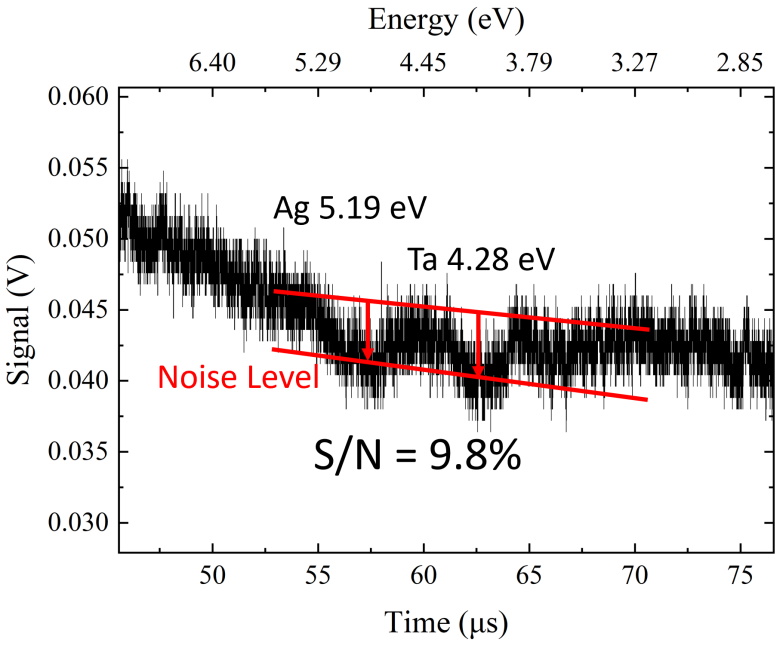


(a) The experimental result of NRS using LDNS without any shield and collimator. The resonance samples were Ag and Ta.

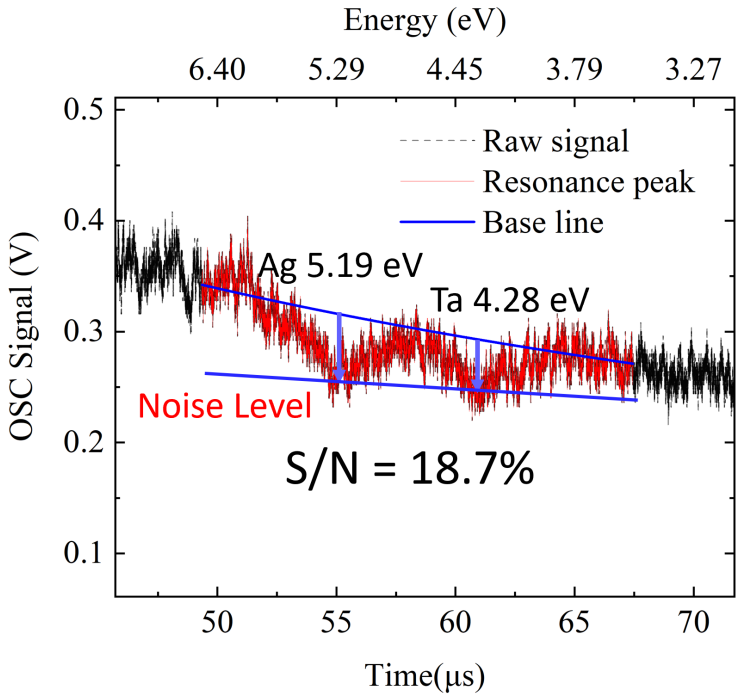


(b) The experimental result of NRS using LDNS with the shield and collimator designed above. The resonance samples were Ag and Ta.

FIGURE 3.12

# Chapter 4

# Single-shot Neutron Resonance Spectroscopy using Laser-driven Neutron Source

The experiment was implemented for the measurement of neutron resonance absorption. The resonance peaks of various isotopes were observed with a beamline of 1.82 m in every single shot of LDNS. The main propose of the experiment is to demonstrate the feasibility of neutron resonance measurement with LDNS and to evaluate the neutron source pulse duration for further discussion on energy resolution of the TOF method.

## 4.1 Experimental setups

The laser facility used in the experiment is Laser for Fast Ignition Experiments (LFEX at ILE, Osaka Univ., Japan). Three beams of LFEX deliver laser pulses with a duration of 1.5 ps (FWHM), a central wavelength of 1.0 μm and an energy of ∼1000 J (∼300 J/beam). The laser intensity is on the order of $10^{18\sim19}$ W·cm$^{-2}$. The high-energy ions (mainly protons and deuterons) are accelerated via TNSA mechanism (as introduced in Chapter2) from laser-irradiation targets[22–24] which are deuterated polystyrene (CD) foils with thickness of 5 μm. The experiment was including 3 phase with different target for the measurements of ions, fast neutrons and epithermal neutrons, respectively.

In first phase of the experiment, the spectrum of accelerated ions was investigated by a TPIS which was set to be coaxial with incident laser, while the laser normally irradiates the CD foil. In the second phase, a cylindrical beryllium

($\phi$ = 0.5 cm, t = 1 cm) set at 2 mm downstream of CD foil, which generates fast neutrons via (p,n) and (d,n) reactions. The fast neutron spectrum was measured by a high-speed TOF detector coupled with liquid the scintillator[71] at 8.257 m, 15° off-axis. The laser condition and incident arrangement is same with the first phase.

In the last phase, the beryllium is embedded in a high-density polyethylene (Fig. 4.1(b)) which is used as the neutron moderator to slow down fast neutrons. The laser was arranged to irradiate at 40° off-axis. A time-gated TOF detector with a $^6$Li-glass scintillator (GS20, $\phi$ = 2.54 cm, t = 1 cm) was used to measure the neutron signal in 1∼20 eV region. The time-gated TOF detector was arranged coaxial with the Beryllium at 1.82 m far from main target (Fig. 4.1(a)). A customized shield were used to protect the GS20 from intense X-ray background and scattered neutrons. The shield consists of one layer Pb and one layer 10% $B_2O_3$ mixed polyethylene. Both of layers are with thickness of 5 cm. The GS20 coupled Gated-PMT was set in the shield with a 1 mm thickness cylindrical Cadmium collimator (Fig. 4.1(c)). If the scattered neutrons pass though the shield, the cut-off effect of cadmium[93] is anticipated to absorb low-energy neutrons that are slowed down by the polyethylene. For the epithermal neutron beamline, an aluminum flange with center thickness of 5 mm is used for the high transmittance of the neutrons. The Gate-on timing of the PMT was set at 20 μs after laser shot, corresponding neutron energy of 0∼43.3 eV. In resonance measurement shots, Tantalum, Silver and Indium were used as the samples that occur neutron resonance absorption. The laser shots were implemented with two cases, a Ta sample or three layers of Ta, Ag and In. Fig. 4.2 shows dimensional details of the HPDE moderator. This special shape of circular truncated cone with side cut is designed for the laser alignment. The volume and thickness of the moderator is optimized with the simulation results in Chapter3.

## 4.2 Experimental results and analysis

### 4.2.1 Energy spectrum of laser-driven ion acceleration

By normally irradiating of LFEX laser on a 0.5 μm CD foil, protons and deuterons were accelerated to 10s of MeV. The TPIS, set coaxial with the laser, was used to measure the energy spectrum of ions with distinguished species. The

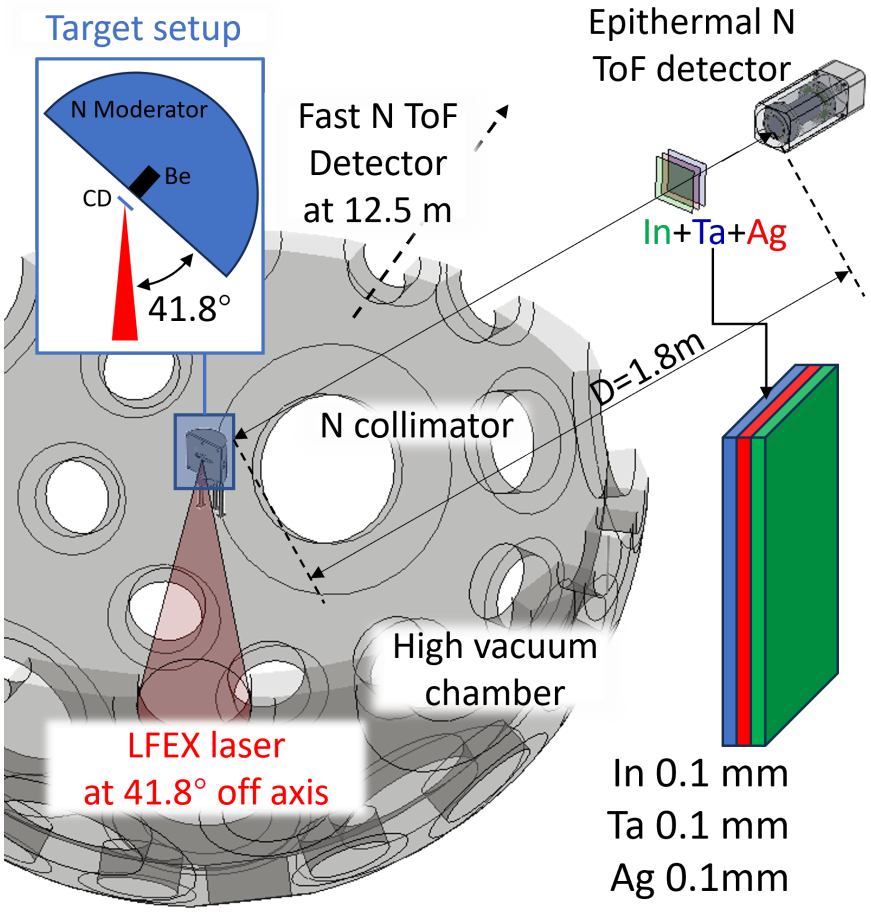


(a) Experimental setup geometry

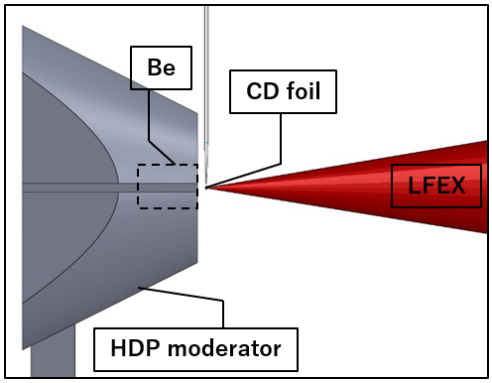


(b) Enlarged target geometry

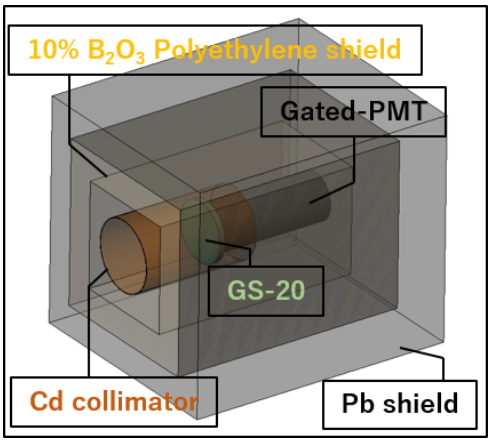


(c) N-ToF detector geometry

FIGURE 4.1

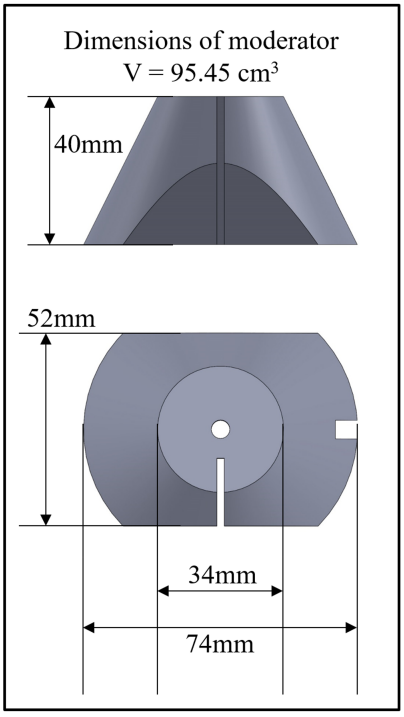


FIGURE 4.2: HDPE moderator geometry

ion energy spectrum is shown in Fig. 4.3(a). The spectrum shows a typical exponential distribution with a cut-off energy. As Ref.[94] indicated, $^{9}$Be(d,n)$^{10}$B and $^{9}$Be(p,n)$^{9}$B reactions have thresholds at 0.5 MeV and 2.2 MeV, respectively (Fig. 4.3(b)). After a sharp rising edge, the neutron yield begins to level off with the increase of ion energy higher than the threshold. Meanwhile, the protons and deuterons accelerated by LFEX has a high flux in 10s of MeV and MeV regions with maximum energy of 33 MeV and 8 MeV, respectively. This modeling illustrates that the laser-driven ion acceleration using LFEX is applicable to neutron generation based on PC method. In addition, the experiment only used 3 beams of LFEX which can provide 4 beams with a total energy of 1200 J, thus, the ion energy and flux can be further improved.

### 4.2.2 Fast neutron generation results

By setting a Be at downstream of CD foil, fast neutrons can be generated via $^{9}$Be(d,n)$^{10}$B and $^{9}$Be(p,n)$^{9}$B reactions. A fast-responding liquid scintillator is coupled with a PMT to consist the fast neutron ToF detector. The detector was set at 15° off-axis with laser as described in Section4.1. A typical raw fast neutron signal is shown in Fig. 4.4(a). An intense signal peak can be observed almost simultaneously with laser shot, which corresponds to strong $\gamma$-ray and

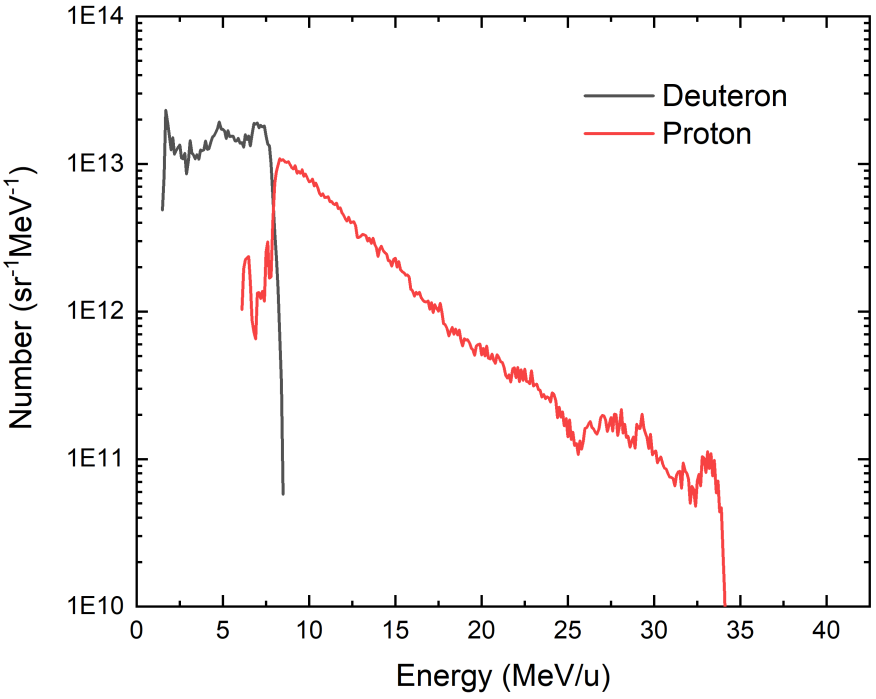


(a) Ion spectrum measured by TPIS

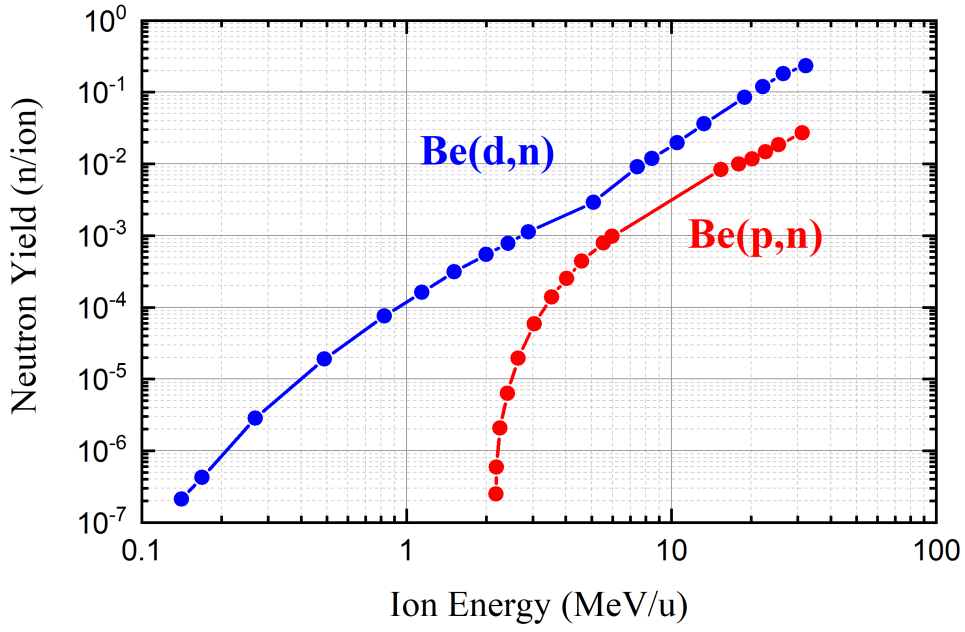


(b) Fast neutron yield of a thick target

FIGURE 4.3

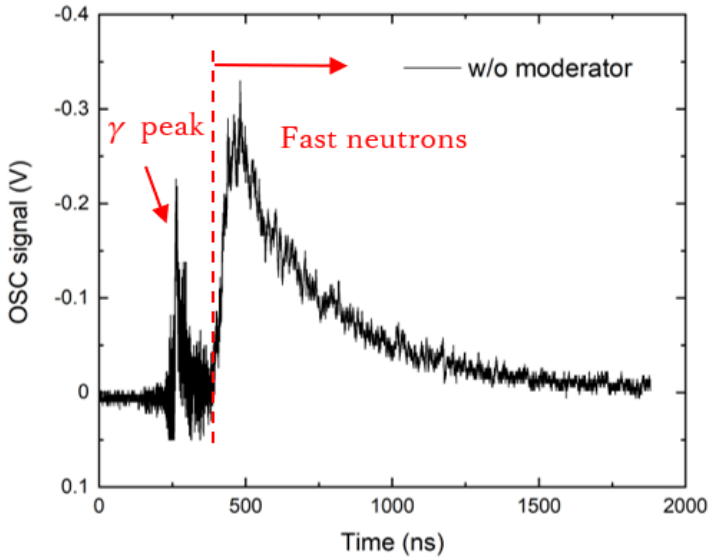


(a) Raw signal of fast neutrons measured by TOF detectors

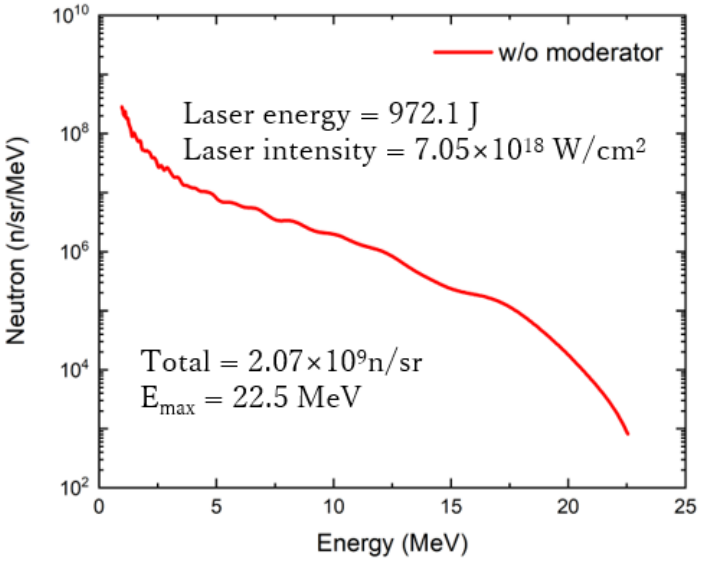


(b) Fast neutron spectrum

FIGURE 4.4

X-ray generated via Bremsstrahlung of hot electrons. Though the liquid scintillator is sensitive to the X-ray, the fast-respond feature lead to a very short decay time of the X-ray signal. By employing an appropriate TOF arrangement, this X-ray signal can be distinguished from neutron signal temporally. As seen in Fig. 4.4(a), the $\gamma$ peak exponentially decays to zero before the fast neutron arrives. Taking account of point spread function (temporal broadening of detector response to single neutron) and efficiency of the detector, the energy spectrum can be obtained from the signal (Fig. 4.4(b)). As the results, the neutron spec-

trum shows a exponential LFEX-based LDNS is capable of high-flux neutron generation with yield of $2.07\times10^{9}$ n/sr (1 MeV $\sim$ Maximum). During several shots, the recorded neutron signal gives similar spectrum with the maximum of 10s of MeV and highest flux in the $\sim$ MeV region. Compare with the Ref.[25] which introduced the neutron yield of LFEX neutron source, the yield is reduced by one orders of magnitude. This shot was implemented with 3 beams of LFEX, the laser energy was 972.1 J and the laser intensity was $7.05\times10^{18}$ W$\cdot$cm$^{-2}$. The reason could be lower energy and less intense due to the lack of one laser beam. But the Ref.[26] reports that LFEX-based LDNS gives neutron yield of $\leq10^{9}$ n/sr/pulse, which is highly coincide with the experimental results. However, it is necessary to note that fast neutron yield reported in Ref.[26] was detected with an solid hydrogen moderator attached behind the Be, while the signals in Fig. 4.4 were measured without any moderator. Considering the lack of one laser beam, the difference is reasonable. Even though, the yield is still sufficient to generate detectable amounts of low-energy neutrons by employing an HDPE moderator.

### 4.2.3 Single-shot neutron resonance spectroscopy results

A customized HDPE moderator was attached on Be to generate epithermal neutrons. A specialized epithermal neutron TOF detector was used to record the neutron signal as described in Chapter3. Three different materials were used as resonance sample in the experiment. At first, a 0.5 mm Ta plate is set in front of cadmium collimator entrance. Fig. 4.5(a) gives a geometry of TOF arrangement. Recorded epithermal neutron signal is shown in Fig. 4.5(b). In every shot of the experiment, same features were observed which shows troughs at specific energies. By converting time to energy, it is confirmed that the reason of the troughs is neutron resonance absorption of $^{181}$Ta at 4.28, 10.36 and 13.95 eV. These results further support the point that LDNS provides sufficient epithermal neutron yield for resonance measurement. On the other hand, the LDNS has demonstrated excellent time performance that provide a sufficient time-energy resolution with a short beamline (1.82 m). For the resonance measurement in similar energy region when using an accelerator-driven neutron source, it generally requires 10s of meters beamline[95–97].

To experimentally demonstrate the feasibility of elemental analysis with NRS using LDNS, multiple layers of sample (Ta, Ag and In) were used in the subsequent experiments. Furthermore, the thickness of samples were changed

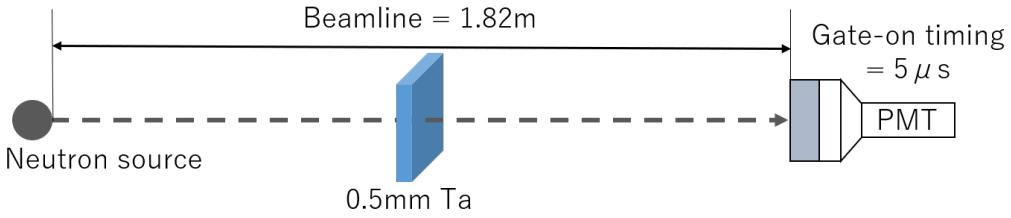


(a) TOF arrangement with resonance sample of Ta

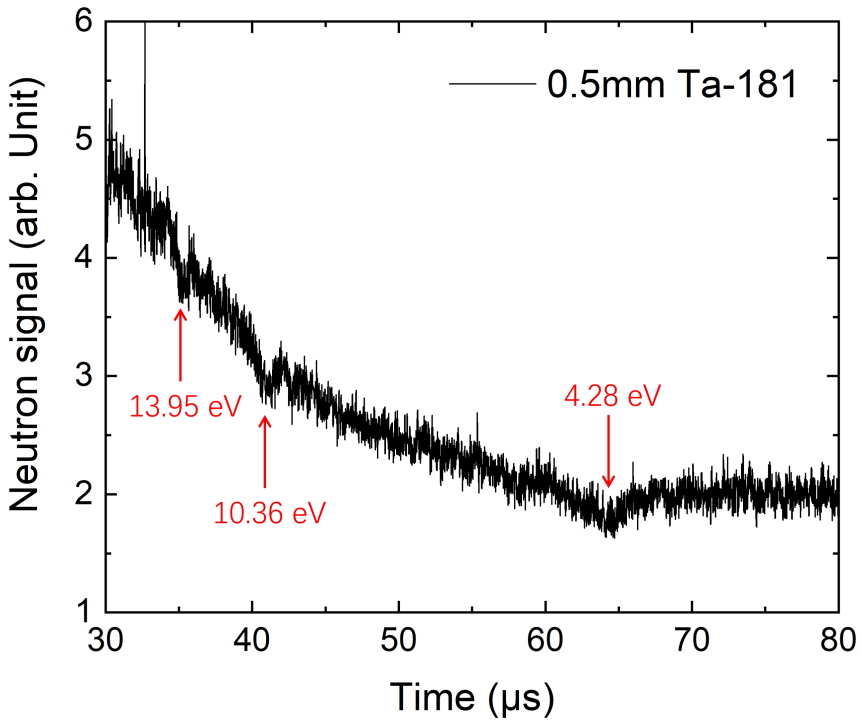


(b) Experimental raw signal of $^{181}$Ta neutron resonance at 4.28, 10.36 and 13.95 eV

FIGURE 4.5: Single-shot NRS measured using LDNS.

between 0.1 and 0.5 mm to evaluate the energy resolution of the TOF measurement (Fig. 4.6(a) and 4.6(b)).

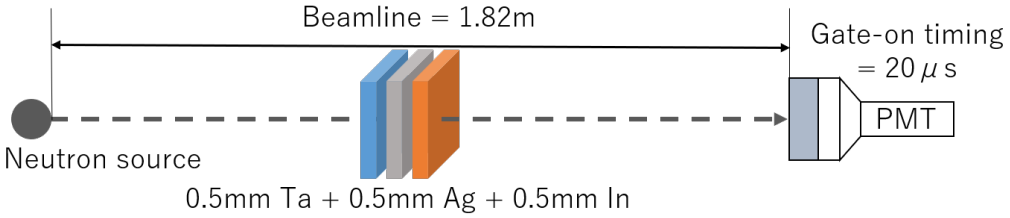


(a) TOF arrangement and resonance samples (0.5 mm)

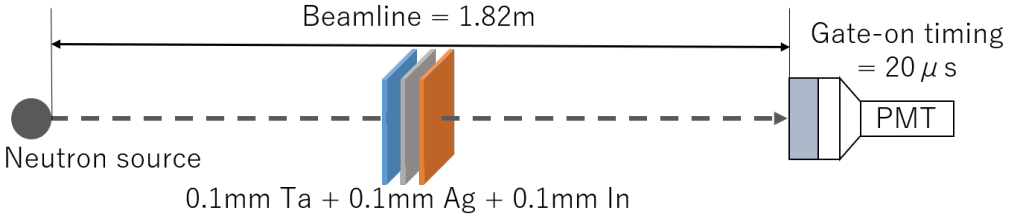


(b) TOF arrangement and resonance samples (0.1 mm)

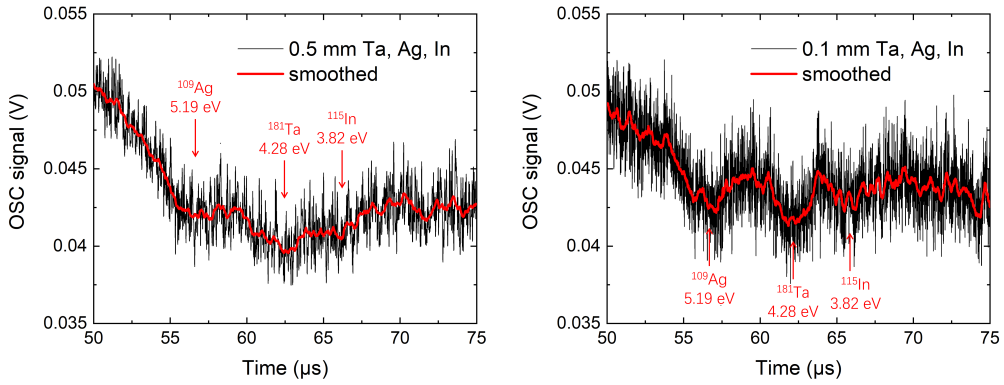


(c) $^{181}$Ta, $^{109}$Ag and $^{115}$In neutron resonance signals

FIGURE 4.6: Multiple resonances measurement results

As seen in Fig. 4.6(c), with the three layers samples of 0.5 mm, the 3 resonances partially overlapped and indistinguishable from each other. When the 0.1 mm samples were used in the TOF measurement, the overlap decreases and the resonances can be individually analyzed. A theoretical calculation (Fig. 4.7) was done by employing Equ.1.3 to investigate how the isotope content (e.g. sample thickness) affects resonance signals. The calculated result indicates that due to the strong resonance absorption of $^{181}$Ta and $^{109}$Ag, when the sample thickness increases from 0.1 mm to 0.5 mm, its absorption rate at resonance energy is saturated. However, at neighboring regions of resonance peaks in where the absorption rate does not reach to 100%, the absorption becomes

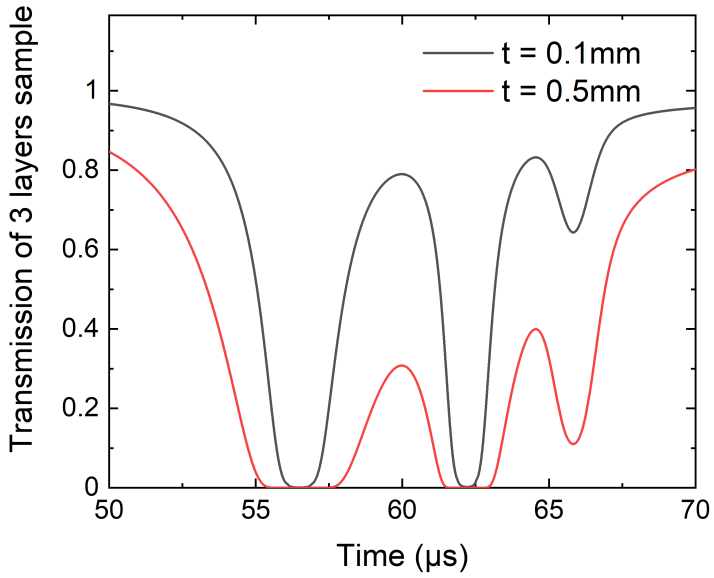


FIGURE 4.7: Calculated transmissions with the thickness of 0.1 and 0.5 mm

stronger with the increasing thickness. This effect results in the broadening of resonance peak detected. The results are anticipated to be an experimental groundwork for the feasible application of neutron resonance to analyze the isotope content of substances.

### 4.2.4 Evaluation of neutron duration and energy resolution

Summarizing above measurement results, the pulse duration of the LDNS can be roughly evaluated. As seen in Fig. 4.6, the $^{181}$Ta and $^{109}$Ag samples completely absorbs neutrons near the resonance energy. However, the neutron signal recorded in experiments (Fig. 4.5(b) and 4.6(c)) did not weaken to zero at the resonance peaks. This indicates that the experimental raw data was accompanied with a strong background. In addition, an exponential post-gate artifact which was much higher than the neutron signal exist right after the gate-on timing. In order to analyze the amplitude and FWHM of resonance peaks, it is necessary to remove the background and the post-gate artifact from the signal. Assuming that the neutron signal has a typical exponential distribution, the original neutron signal from the HDPE moderator (before passing through the samples) can be fitted as a base line (Fig. 4.8(a)).

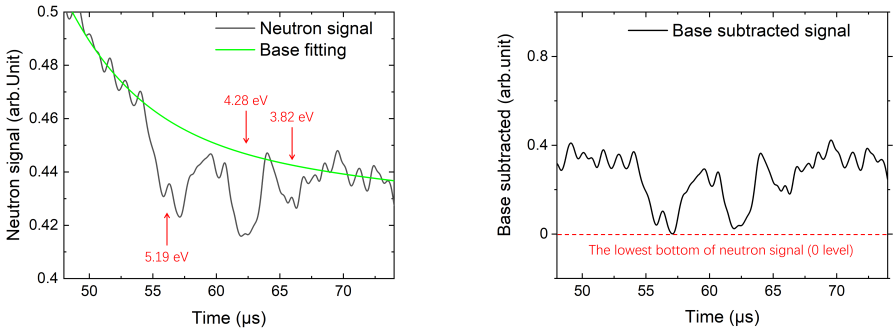


(a) Baseline fitting of the neutron signal (b) Baseline subtracted signal and background estimation

FIGURE 4.8: The analysis of resonances absorption

By subtracting the fitted baseline from the recorded data, the resonance peaks are extracted as Fig. 4.8(b). A moving average smoothing is applied to eliminate the Poisson noise (random vibration). According to Fig. 4.7, neutrons with energies that near resonance peak of Ta and Ag are totally absorbed by the sample, so it is reasonable to assume that neuron signal at centers of the peaks are actually zero. Thus, the portion of the signal due to background irradiation can be estimate, as the dashed line in Fig. 4.8(b), assuming background is constant within the region of the three peaks. According to the neutron signal and estimated background amplitude, the neutron transmittance of resonance sample can be obtained. Since the signal in the experiment contains a lot of random noise, it is difficult to mathematically analyze it to get the pulse duration of LDNS. However, it is possible to estimate source pulse duration by comparison with theoretical calculation results such as Fig. 4.7 shows. In Fig. 4.7, the transmittance curve is an ideal situation without considering the source duration. If it is convolved with the time distribution of the neutron source (Fig. 1.5(c)), the predicted signals under different source duration can be calculated. The experimental transmittance and predicted signals are shown in Fig. 4.9. As discussed in Chapter1, the broadening of neighboring energy neutrons result in the dropping of resonance peaks. When convolved with 5 μs source, as the blue dashed line in Fig. 4.9, the In resonance peak is almost disappeared, the resonance peaks of Ta and Ag also become lower. When convolved with 2 μs source, as the green dashed line, the calculated result obviously starts to approach the experimental signal, but the peak height is still lower than experimental signal. The convolution result of 0.5 μs source is almost same with the one of 2 μs source. These results indicate that the

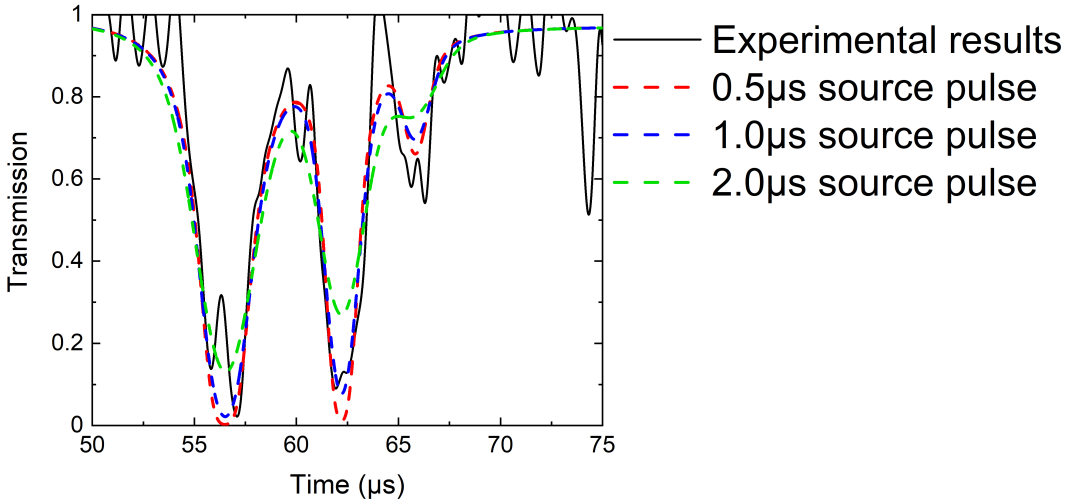


FIGURE 4.9: Experimental transmittance and predicted transmittance

pulse duration (FWHM) of LDNS at 5 eV energy region is lower than 2 μs. For further discussion, the resonance signal of single layer Ta sample (Fig. 4.5(b)) provides a more accurate estimate with wider energy range.

The source pulse duration of LDNS is also estimated at energy of 13.95 and 10.36 eV using the experimental results of the single Ta sample (Fig. 4.10). The

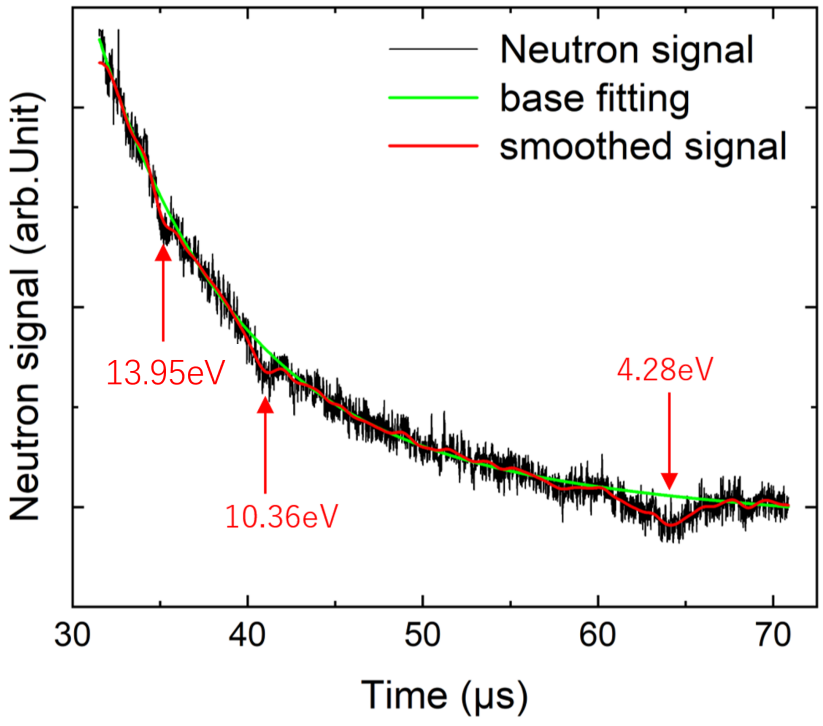


FIGURE 4.10: Neutron signal and baseline fitting of Ta-181 sample

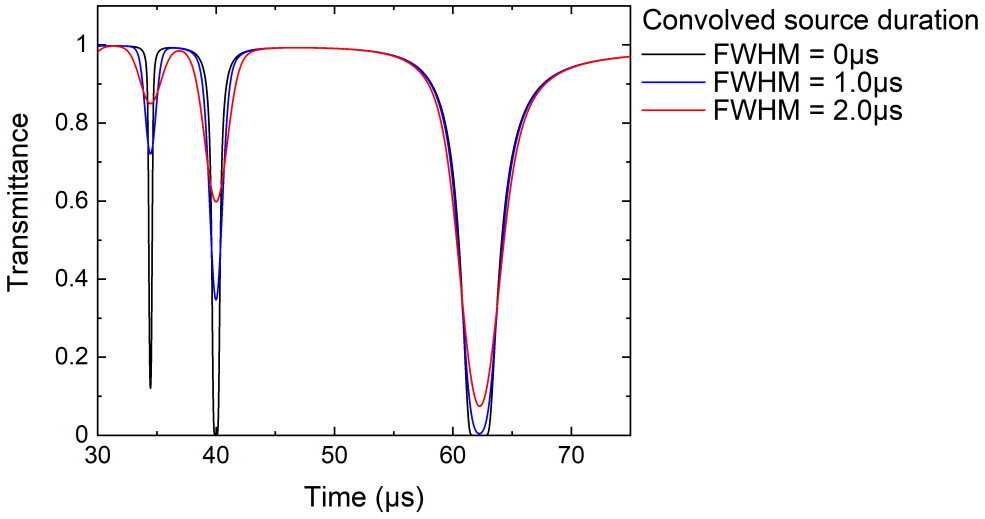


FIGURE 4.11: Calculated transmittance with various source duration (FWHM)

pulse duration at 10.36 and 13.95 eV were evaluated by the experimental results (Fig. 4.10 ) and *PHITS* simulation (Fig. 4.12(a)). The evaluation method is : firstly, fix the shift in time axis by align the peak of resonance energy in experimental data and the evaluated cross-section (Fig. 1.5(a)). Then, calculate the theoretical NRS with assumed pulses as shown in Fig. 4.11. At last, find the calculation that best fits experimental results. Therefore, the corresponding pulse duration is estimated by the fitting.

In order to verify the validity of the evaluation, a PHITS simulation is employed to calculate the theoretical source duration using the experimental fast neutron spectrum (Fig. 4.4(b)) and moderator (Fig. 4.2). Fig. 4.12(a)) shows the simulation results of mono-energy neutrons duration. At the energies of 3.82, 4.28 and 5.19 eV (corresponding to three resonance peaks of $^{115}$In, $^{181}$Ta and $^{109}$Ag in Fig. 4.6(c)), the FWHM are 0.65, 0.62 and 0.56 μs, respectively. Furthermore, when the neutrons with several eV energies pass through 1 cm distance in the scintillator, the flight time is in sub-μs. Therefore, the time broadening at the detector should be considered for NRS with 1-m-class short beamlines in which 5 eV neutrons flight time is 10s of μs. The pulse broadening at the $^{6}$Li-doped scintillator S(t) is evaluated to be 320 ns for 5 eV neutrons (red line in Fig. 4.12(b)). By convolving the temporal broadening induced by the moderator M(t) (results in Fig. 4.12(a) and green line in Fig. 4.12(b)) and the scintillator S(t), the total pulse broadening effect in the neutron detection

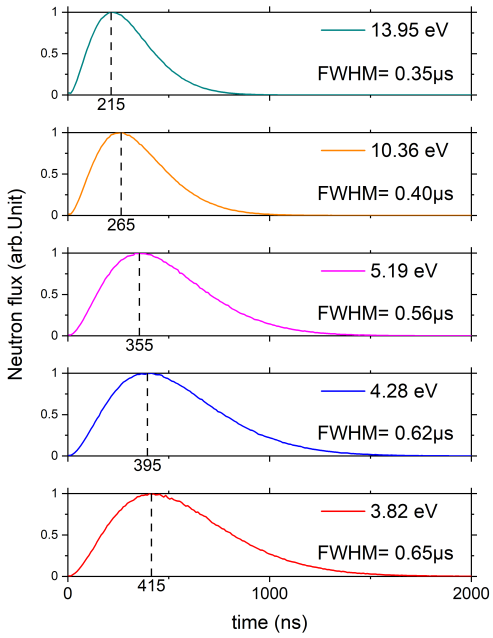


(a) Mono-energy neutrons pulse duration calculated by *PHITS*

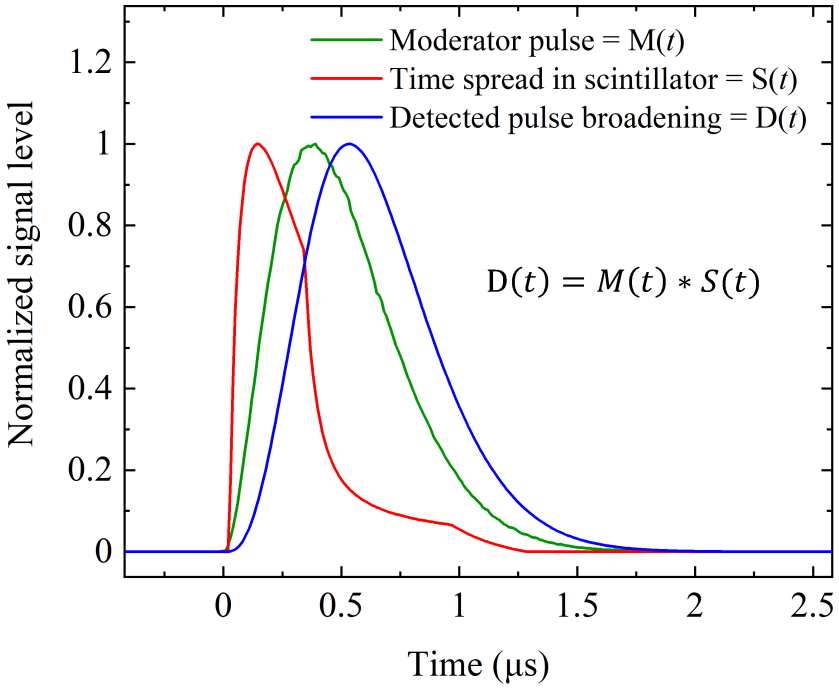


(b) Pulse duration at the simulated neutron moderator (green line, same as Fig. 4.12(a)), the time spread when neutron pass through the $^{6}$Li glass scintillator (red line), and convoluted result of response pulse broadening at the detector (blue line, systematic error).

FIGURE 4.12

is obtained as D(t) = M(t) ⊗ S(t) (blue line in Fig. 4.12(b)), where ⊗ represents the convolution operation. The FWHM of D(t) can be estimated as $\Delta\tau = \sqrt{\Delta\tau_m^2 + \Delta\tau_t^2}$, where $\Delta\tau_m$ and $\Delta\tau_s$ are the FWHM of pulse broadening at moderator and scintillator. For the neutrons of 5.19 eV, $\Delta\tau = 0.66$ μs.

The evaluated pulse duration results are listed in Table4.1. The experimental results of pulse duration are about 0.1∼0.3 μs longer than the simulation results (Fig. 4.12(a)). The reasons could be the strong background of scattering neutron from the chamber and other structures, intense X-ray generated in high-energy laser experimental environment and the artifact signal of time-gated PMT. All the noises are affecting the TOF method (scattering neutron with different TOF) or the response of PMT (saturation caused by intense X-ray), finally result in the disagreement between experimental data and simulation results. In addition, the LFEX and almost all of high-energy laser facilities have very strong fluctuations of energy and intensity due to the technological constraint on laser focusing and amplification. In spite of the differences, the estimated duration results (Table4.1) are not so far from the simulation (Fig. 4.12(a)), which shows that the estimation model is valid to some extent. By the improvement of detector, shield and collimator, the experimental data is anticipated to gradually approach the simulation results. The nickle collimator introduced in Chapter3 were imported in the subsequent experiments which are introduced in Chapter5. The results are the first evaluation result of the

| Energy (eV)) | 4.28 | 10.36 | 13.95 |
|---|---|---|---|
| Estimated FWHM (μs) | ∼0.8±0.2 | ∼0.6(±0.2) | ∼0.5(±0.2) |
| Energy resolution (roughly estimated, $\Delta E/E$) | 2.3% | 3.1% | 4.9% |

Table 4.1: Temporal properties of LDNS

temporal performance of the LDNS. The energy resolution is roughly estimated with the estimated source duration and length of beamline (Table4.1).

Compared with accelerator-driven neutron source, the LDNS demonstrates a much shorter pulse duration. This important feature promotes the development on application of NRA with highly special and temporal resolution. The shorter beamline also breaks the limitations of accelerator-driven neutron source. To achieve a same energy resolution with LDNS, accelerator-driven

neutron source generally needs 10s of meters beamline which severely limits the application of accelerator-driven neutron source [9].

Furthermore, the $I_L^4$ law of neutron generation that introduced in Ref.[28] gives an estimation of the neutron yield of LDNS. Combining the yield and energy resolution of LDNS, the experimental applications can be realized in several high-power laser facilities in the world [29, 31, 32, 40]. Even the laser facilities with high repetition rate [47, 48, 98, 99] can further improve the NRS method using LDNS.

# Chapter 5

# Temperature Dependency of Neutron Resonance

This Chapter introduces a proof-of-principle experiment on a single-shot neutron thermometry using a 1.8 m NRS beamline driven by laser[46]. The temperature dependence of neutron resonance absorption measured using a short-pulse ($<$ 1 μs in neutron energy of eV) and high-intensity LDNS. The NRS was measured by TOF method to analyze the Doppler broadening of the resonance peak with a 0.1 mm thick tantalum plate heated to 350∼600 K.

## 5.1 Experimental setup

The experiment to measure the temperature-dependent neutron resonance was carried out using 1.5 ps beams from the Laser for LFEX [100] delivering a total energy of 900 J on the target at ILE, Osaka University. The setup (Fig. 5.1) is almost the same with single-shot NRS experiments introduced in Chapter4. A laser pulse with an intensity of ∼1 $\times$ $10^{19}$ W·cm$^{-2}$ [28] was focused on a 5 μm thick deuterated polystyrene (CD) foil to accelerate protons and deuterons(Fig. 5.4(a)) induce nuclear reactions of (p,n) and (d,n) to generate neutrons. The energy of the ions was measured by a TPIS located in the normal direction of the CD foil when the secondary target and $^{6}$Li-TOF detector were removed. As introduced in Chapter2, protons and deuterons were accelerated up to MeV energy, where the ps duration laser pulse enhanced the acceleration of the deuterons [101] that were initially covered by a contaminant layer of hydrocarbons.

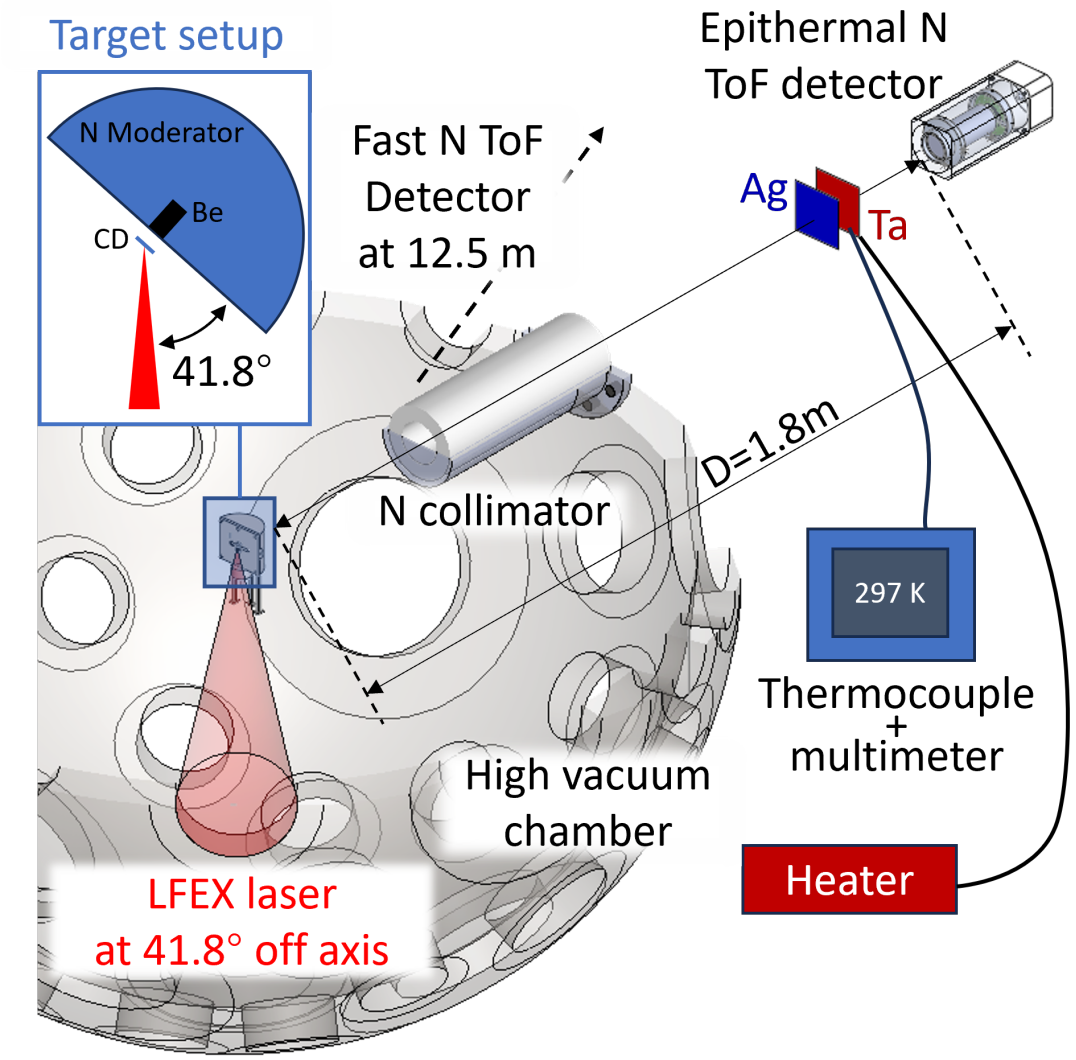


FIGURE 5.1: The experimental setup of the laser-driven epithermal neutron generation and resonance absorption measurement using the TOF method[46].

To generate neutrons, the ions were injected into a secondary target, a Be cylinder with a diameter of 10 mm and a thickness of 10 mm. The diameter is designed to be larger than the angular divergence of the incident ions. The thickness is designed to be sufficient for stopping the ions. Fast neutrons with energy over tens of MeV were generated via the $^{9}$Be(p,n)$^{9}$B and $^{9}$Be(d,n)$^{10}$B reactions and analyzed by the fast neutron TOF detector [28] introduced in Chapter2. The fast neutron TOF detector was located 12.5 m from the LDNS outside the vacuum chamber and measured the fast neutron spectrum in each laser shot. The fast n-TOF detector was calibrated by a bubble detector [102] to obtain the correct energy spectrum and neutron number. This part on above is the same with the setup in Chapter4.

Compared with the experiment in Chapter4, the main improvements include the moderator design, development of beamline and resonance samples. As introduced in Chapter2, the neutron moderator used in our experiment was made from high-density polyethylene (0.98 g·cm$^{-3}$). Different than previous design in Chapter4, the moderator was designed in a shape of cylinder. The moderator geometric diagram is shown in the Fig. 5.2. The moderated neutrons passed through an aluminum window (for high transmittance of the neutron beam) into air and were measured at 1.78 m by another $^{6}$Li-TOF neutron detector consisting of a $^{6}$Li-doped glass scintillator (GS20, Scintacor Ltd., 10 mm in thickness) coupled to a originally developed time-gated PMT introduced in Chapter3. To protect the PMT and ensure the linearity of it's output response, the time gate was set to block the electromagnetic pulses and the intense flash of X-rays generated by the laser-plasma interactions. Furthermore, to reduce the background of neutrons scattering at the chamber wall, the nickel (Ni) collimator that introduced in Chapter3 was installed on the chamber along the beamline.

The neutron resonance absorption is identified predominantly in the energy region of eV (Fig. 5.3). The neutrons in eV region is suitable to measure the Doppler width of sub-eV, which corresponds to the temperature of 300-1000 K.

## 5.2 Experimental results

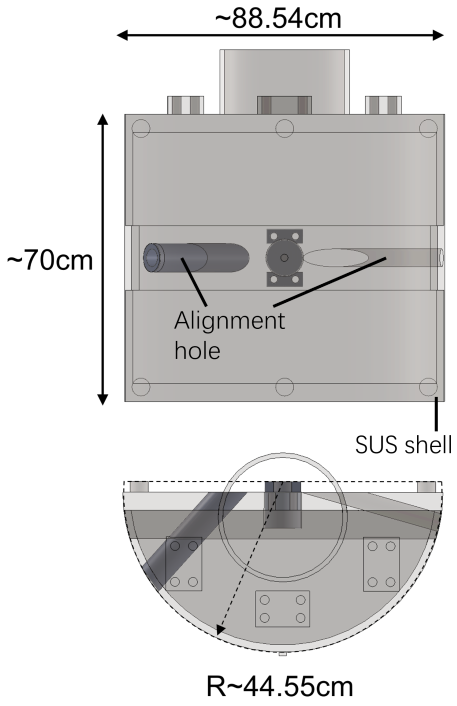


FIGURE 5.2: The moderator design diagram. A SUS shell is used to fix high-density polyethylene. And there are tow through holes for alignment and avoiding direct irradiation of the stray light focused by the laser system.

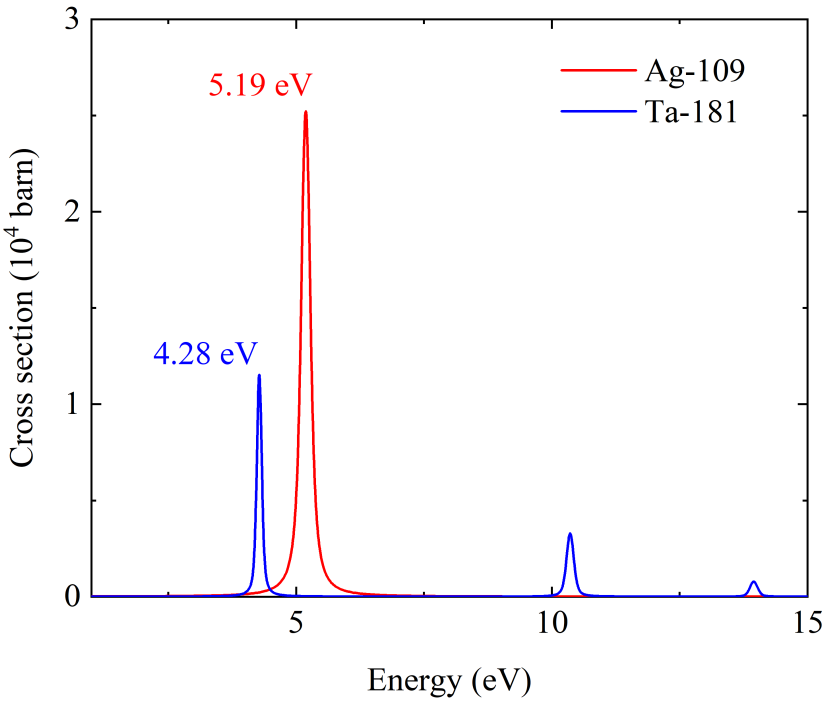


FIGURE 5.3: The neutron absorption cross sections of $^{109}$Ag and $^{181}$Ta obtained from JENDL4.0 data base [76].

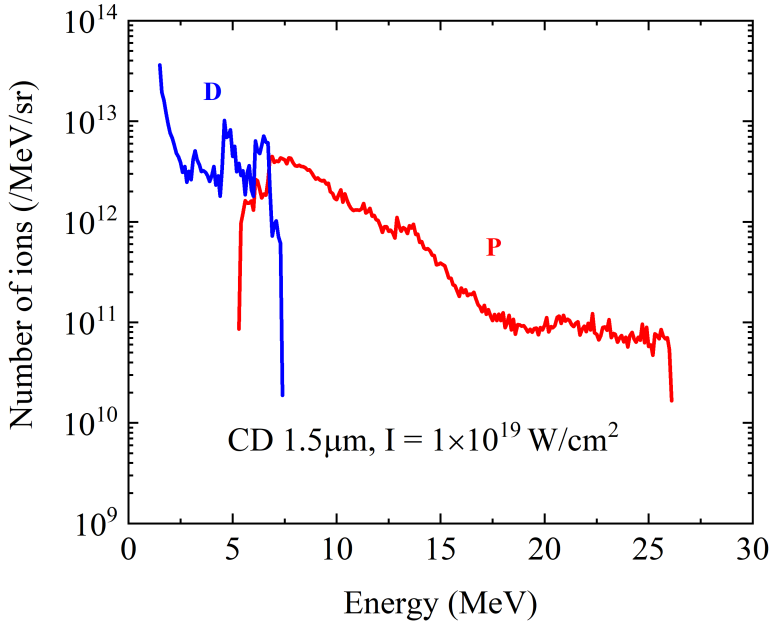


(a) The ion spectrum measured by a Thomson Parabola (TP) ion spectrometer.

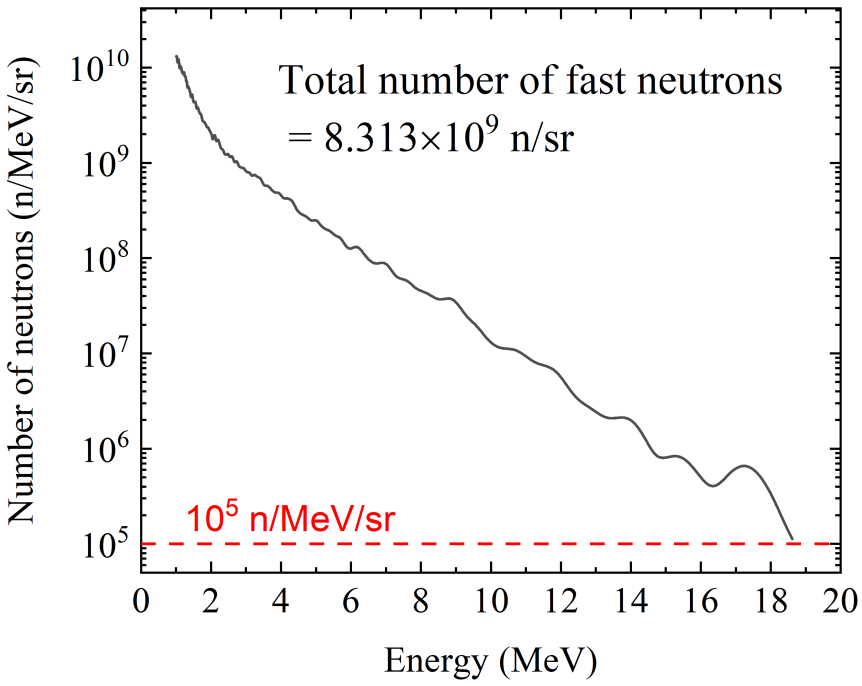


(b) The fast neutron spectrum measured by the fast n-TOF detector.

FIGURE 5.4

### 5.2.1 Ion and fast neutron spectrum

As a typical shot of the LDNS (Fig. 5.4(b)), the maximum energy of the fast neutrons reaches 18.6 MeV, with a neutron number of $8.313\times10^9$ n/sr. The total number was calculated by integrate the neutron spectrum in the energy range above 1 MeV. The real neutron number can be much higher than it with considering of neutrons of under MeV energy. The angular distribution of the fast neutrons is close to isotropic according to our previous work [28]. This indicates that the total number of neutrons in the $4\pi$ direction reaches $10^{11}$ in a single laser shot. Compared with other LDNSs [31, 38, 39, 103], our neutron number is one to two orders of magnitude higher. Benefited by the large number of fast neutrons, a high flux of moderated neutrons can be expected.

### 5.2.2 Simulation of epithermal neutron pulse duration and broadening on detectors

As mentioned in Chapter1, the energy resolution of TOF method depends on the pulse duration of the neutron source. The process of moderation inevitably broadens the pulse duration of the neutron source. Since the moderator design is different from previous experiments. A *PHITS* [68] simulation was used to evaluate the temporal structure of the moderated neutron pulses. In the simulation, the neutrons are monitored at the exit of the moderator. Fig. 5.5(a) shows the temporal structure of moderated neutrons M(t) with kinetic energies 5.19 eV and 4.28 eV, which correspond to the resonance energies of $^{109}$Ag and $^{181}$Ta (Fig. 5.3), respectively. These materials are well-suited for demonstration purposes because their resonance peaks exhibit a large reaction cross sections and are not affected by nearby resonances. Here, time zero indicates the time when the laser is first incident on the target, and the time for neutron generation in the LDNS is shorter than 50 ps [28, 31, 38, 39]. The pulse broadening is evaluated to be 562 and 618 ns at the FWHM for 5.19 and 4.28 eV neutrons, respectively, based on the temporal structures (Fig. 5.5(a)). The peaks are delayed by 350-400 ns. The upper part of Fig. 5.5(b) shows the delay of the pulse peak at the moderator exit as a function of the neutron energy. The delay leads to non-negligible underestimation of the neutron energies in TOF analysis due to the flight distance extremely shorter than that of accelerator-based neutron facilities. We evaluate the energy shift caused by the underestimation to be 0.0524 eV and 0.0635 eV for 4.28 eV and 5.19 eV

neutrons(lower part of Fig. 5.5(b)), respectively. The pulse broadening at the $^{6}$Li-doped scintillator S(t) is evaluated to be 320 ns for 5 eV neutrons (red line in Fig. 4.12(b)).

Same as the method in Chapter4. By convolving the temporal broadenings induced by the moderator M(t) (green line in Fig. 4.12(b)) and the scintillator S(t), the total pulse broadening effect in the neutron detection is obtained as D(t) = M(t) $*$ S(t) (blue line in Fig. 4.12(b)), where $*$ represents the convolution operation.

### 5.2.3 Single-shot analysis of neutron resonance

By using the D(t) function, we obtain TOF signals with the pulse broadening effects at the moderator and the detector being removed in every laser shot. Fig. 5.6(a) shows the signal of epithermal neutrons transmitted through Ag and Ta plates and recorded by the 6Li-TOF detector. The samples were at room temperature (296 K). Note that the TOF results were measured for a single laser shot without any time integration. In the time region of 50-60 μs, two distinct dips are seen in the continuous neutron signal. In the following, we investigate whether the two dips can be attributed to the neutron resonances of $^{109}$Ag and $^{181}$Ta. The flight time $t_{raw}$ measured by the detector is expressed by

$$t_{raw} = t * D(t), \tag{5.1}$$

where $t$ is the flight time deconvolved from the pulse broadening $D(t)$. The $*$ represents the convolution. The neutron kinetic energy $E$ is obtained by $E = m(d/t)^2/2$, where $d = 1.78$ m is the flight distance, and $m$ is the mass of the neutron. The TOF signal in Fig. 5.6(a) is converted into the neutron absorption rate $R_{exp}(E)$ (dashed line in Fig. 5.6(b)), where we assume $R_{exp}(E) = 0$ for the base line (dashed line in Fig. 5.6(a)) since the original neutron signal should be a smooth curve [104].

In present analysis, we evaluate the background level for each laser shot using the reference foil (Ag) in the following procedure similar to black resonance [105]. The baseline [the blue dashed line in Fig. 5.6(a)] is obtained from a least-square fitting for the raw signals excluding the two resonance dips. The background (the green solid line) is obtained from the baseline by subtracting the depth of the resonance peak of $^{109}$Ag, because the Ag target is enough thick

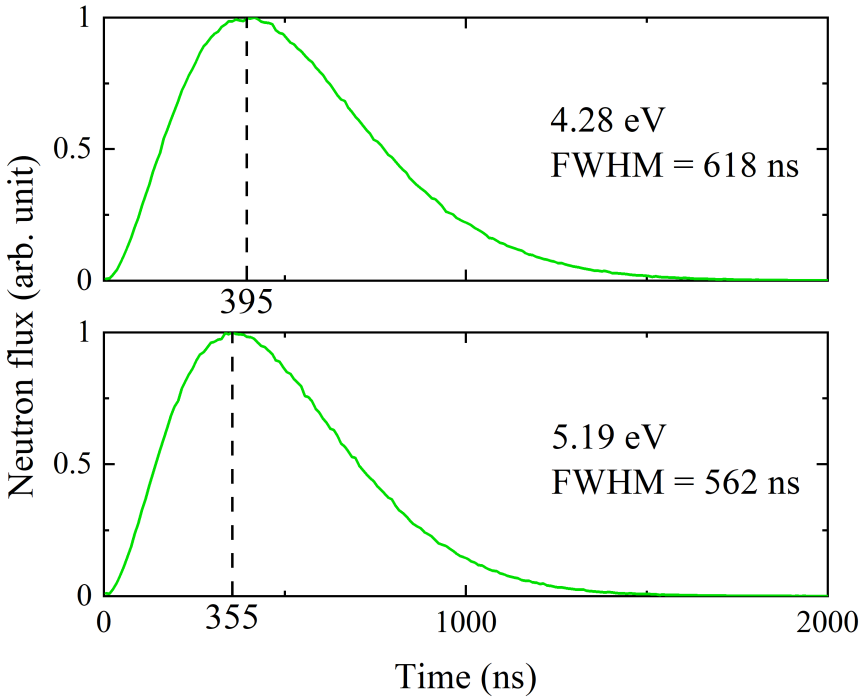


(a) Simulated pulse duration for 5.19 eV and 4.28 eV neutrons. The vertical dotted lines are marking the peak timing of the neutron pulse.

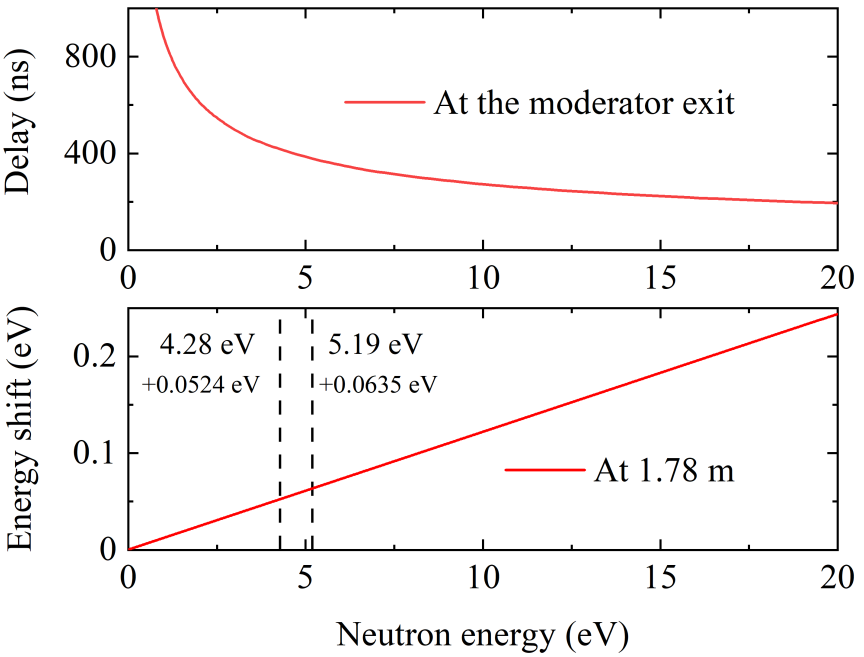


(b) Simulated neutron flight time delay and detected energy shift at 1.78 m. The horizontal axis represents the original neutron energy. Tow vertical dotted lines are marking the energies of resonance peaks measured in the experiment.

FIGURE 5.5

to absorb almost all neutrons around the resonance energy. From the difference between the raw signal and the baseline, the experimental absorption rate $R_{exp}(E)$ normalized to the difference between the baseline and the background is obtained as the blue dashed line in Fig. 5.6(b). The absorption rate $R_0(E)$ for the Ag and Ta foils is theoretically analyzed by

$$R_0(E) = 1 - \prod_{Ag,Ta} \exp(-nl\sigma(E)), \tag{5.2}$$

where $n$ is the volumetric number density, $l$ is the thickness of the targets and $\sigma(E)$ is the NRA cross section (JENDL4.0 data base [76]) at 300 K (Fig. 5.3). The black line in Fig. 5.6(b) shows the theoretical absorption rate when $t_{raw} = t$ without considering the effect of $D(t)$. $R_{exp}(E)$ exhibits two peaks at 4.3 and 5.2 eV which are also found in the analytical model $R_0(E)$. However, the detailed shape of the experimental peaks is not well reproduced by $R_0(E)$, especially for the thicker target (Ag), where the saturated absorption observed in $R_0(E)$ is not exhibited in $R_{exp}(E)$. This difference indicates the presence of another effect, $F(t)$, that causes further pulse broadening in addition to $D(t)$.

The pulse broadening caused by effects other than $D(t)$ including statistical neutron scattering along the beamline, is involved in $F(t)$ in a Gaussian form. We determine the function $F$ by fitting the experimental absorption rate $R_{exp}(E)$ with the following equation:

$$R_1(E) = (R_0 * F)(E), \tag{5.3}$$

where $F(E)$ is expressed as a function of the neutron energy $E$. Fig. 5.6(c) shows $R_{exp}(E)$ (gray) fitted with the model $R_1(E)$ (red) by using an nonlinear-curve-fitting function, where the resonance peaks are well reproduced as the errors shown in the lower frame, without the discrepancies observed in Fig. 5.6(b). $F(t)$ has a half-width of approximately 100 ~200 ns, which is sufficiently shorter than $D(t)$ (~0.6 μs), indicating that the advantage of the miniature size of the moderator is not offset by the pulse broadening caused along the beamline. Compare with previous results [28], performed with the setup without the neutron collimator (see Fig. 5.1), the TOF signal (Fig. 5.6(c))shows narrower peaks for Ag and Ta. This fact indicates that $F(t)$ can be reduced by optimizing the background shielding as introduced in Chapter3.

### 5.2.4 Analysis of Doppler broadening

In this section, we demonstrate a proof-of-principle experiment for the neuron thermometry with the laser-driven NRS. To analyse the temperature dependence of the resonance absorption, we introduce a Breit-Wigner (BW) single-level formula [4], as seen in [13, 97], for the neutron absorption cross section at 0 K:

$$\sigma_{BW}(E') = \pi\lambda\!\!\!^{-}\, g_j \frac{\Gamma_n \Gamma_\gamma}{(E' - E_r)^2 + (\Gamma_n + \Gamma_\gamma)^2/4}, \tag{5.4}$$

where $E_r$ is the resonance energy, $E'$ is the kinetic energy of the incident neutron relative to the target nucleus with $E' = E$ at 0 K, $\lambda\!\!\!^{-}$ is the de Broglie wavelength of incident neutron (divided by $2\pi$), and $g_j$ is a statistical factor determined by the angular momentum. $\Gamma_n$ and $\Gamma_\gamma$ represent the resonance widths for the neutron and decay width for $\gamma$-ray, respectively. For the $^{181}$Ta resonance at $E_r$=4.28 eV, $\Gamma_n$=1.74 meV and $\Gamma_\gamma$=55 meV; For the $^{109}$Ag resonance at $E_r$=5.19 eV, $\Gamma_n$=8.34 meV and $\Gamma_\gamma$=136 meV [76]. The value of $\pi\lambda\!\!\!^{-} g_j$ was determined by fitting the $\sigma_{BW}(E)$ formula to the latest analytical result of JENDL4.0 data base[76], which is one of the standard nuclear database, for 0 K and 300 K.

When the thermal motion of target nuclei is sufficiently slower than the incident neutron, the Doppler broadening effect can be well approximated by a Gaussian function [11, 13]. Therefore, we developed an analytical cross-section $\sigma_T(E, T)$ for the neutron resonance absorption involving the target temperature as follows:

$$\sigma_T(E, T) = A \times \sigma_{BW}(E') * \exp(-\frac{(E' - E_r)^2}{2\Gamma_D^2(T)}), \tag{5.5}$$

where $A$ is a fitting parameter and $E'$ is the relative neutron energy for integration variable. $\sigma_{BW}$ and the following Doppler broadening term are convoluted in the energy axis. The Doppler width $\Gamma_D(T)$ broadens with the temperature $T$. As seen in Fig. 5.7, $\sigma_{BW}(E)$ is in good agreement with the JENDL results for 0 K and 300 K.

Then, the temperature-dependent absorption rate $R_T(E)$ is developed as follows:

$$R_T(E, T) = 1 - \prod_{Ag,Ta} \exp(-nl\sigma_T(E', T)) * F(E'). \tag{5.6}$$

According to the model given by Equ.(5.6), we analyze the absorption rate $R_{exp}(E)$ measured for different target temperature $T$, as shown in Fig. 5.8. The Ta target was heated to T = 361, 413, 474, 573 and 617 K, which is the highest

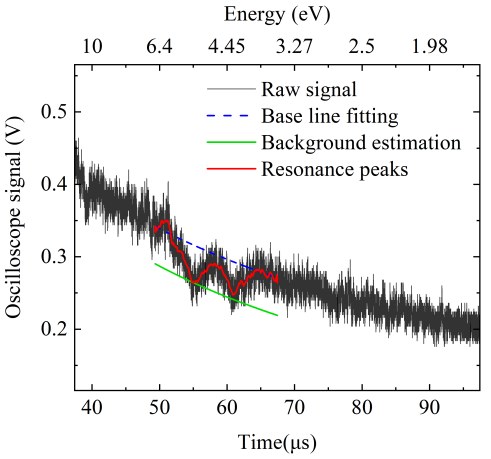


(a) The epithermal neutron signal[46].

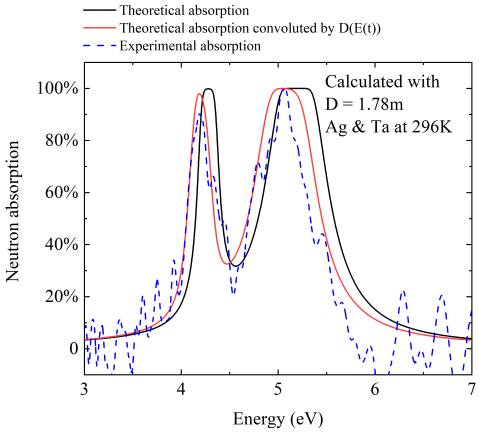


(b) Experimental and calculated neutron absorption with energy axis[46].

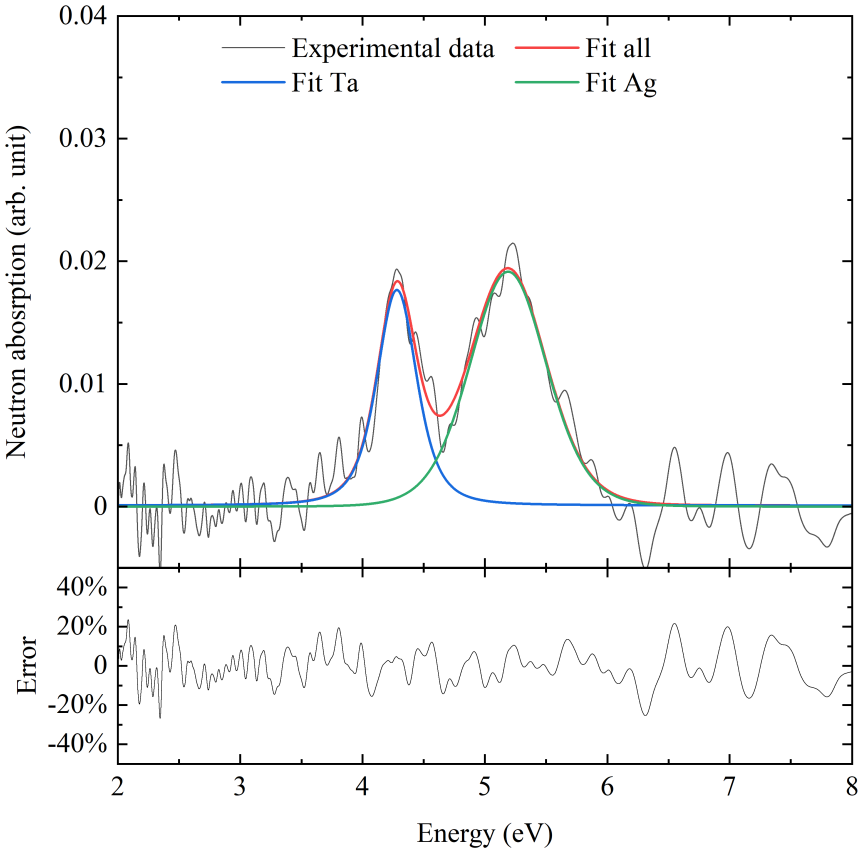


(c) Experimental neutron absorption results and model fitting of Ta and Ag with temperature of 296K[46].

FIGURE 5.6

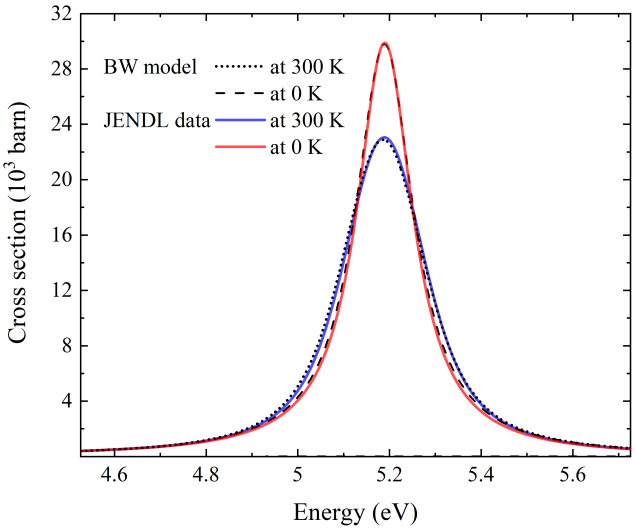


FIGURE 5.7: JENDL cross section data and $\sigma_{BW}(E)$ calculation of a $^{109}$Ag resonance at 5.19 eV[46].

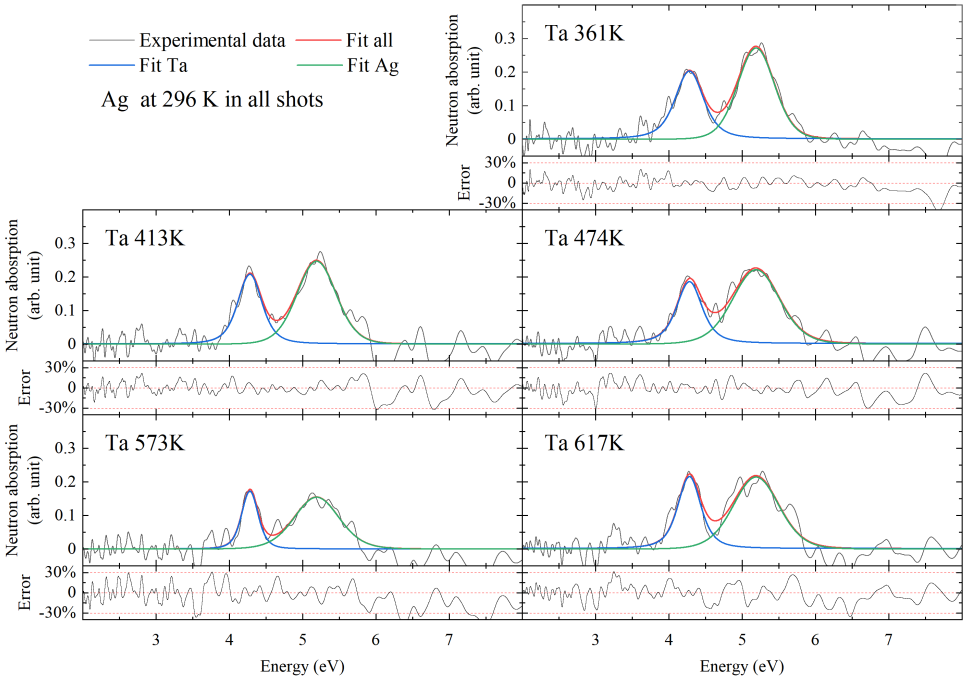


FIGURE 5.8: Experimental neutron absorption results and model fitting by $R_T(E)$. The temperature of Ag was kept at 296K and Ta was heat to T = 361, 413, 474, 573 and 617 K[46].

temperature achievable with the present heating system. The temperature was monitored by a thermocouple, as shown in Fig. 5.1. The Ag sample was kept at room temperature to provide a reference of neutron spectrum and an evaluation of $F(E)$. Here, each measurement was performed by a single pulse of neutrons generated in a single shot of the laser. Although the Ag target was kept at room temperature, it can be seen that the resonance width of Ag varies from shot to shot. This is due to the fluctuation of $F(E)$ caused by statistical processes including neutron scattering on the beamline. Therefore, the Ag resonance serves as a reference to evaluate $F(E)$ for each measurement.

In Fig. 5.9, we plot the Doppler width $\Gamma_D(T)$ obtained by fitting $R_{exp}(E)$ as a function of $T$. The error bars are determined by the least mean square of the difference between the fitted curves and experimental data. The Doppler

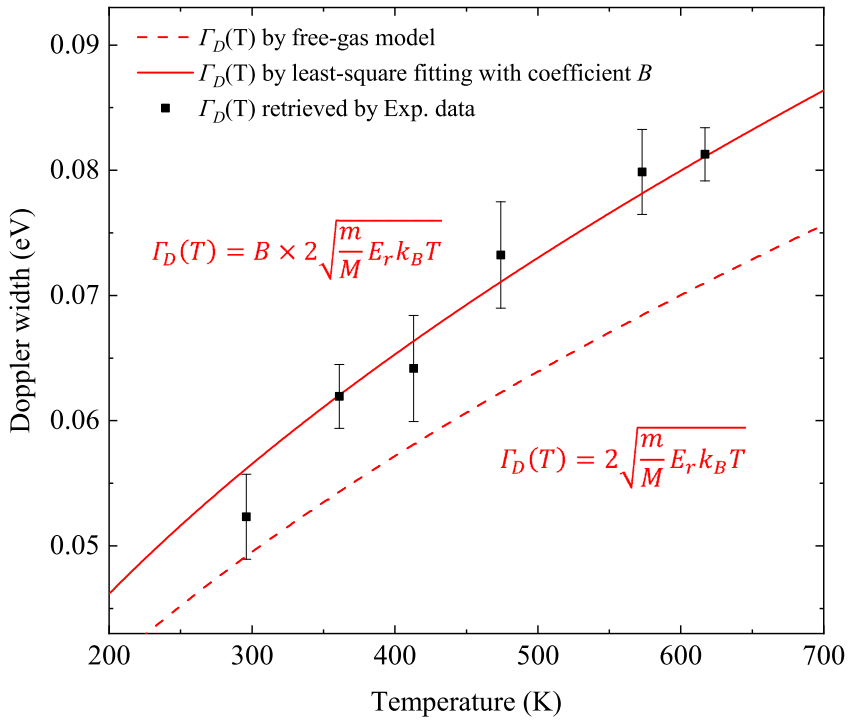


FIGURE 5.9: Theoretical Doppler broadening width and experimental results. The error bars are depended by fitting error and noise level of original signal. The temperature errors are obtained by the propagation of Doppler broadening width errors.

width increases as the square root of $T$, and this result is in agreement with a free gas model by Bethe [5]:

$$\Gamma_D(T) = 2\sqrt{\frac{m}{M}E_r k_B T}, \tag{5.7}$$

where $m$ and $M$ are the masses of the neutron and the target nucleus, respectively, and $k_B$ is Boltzmann's constant (the red dashed line in Fig. 5.9). We also introduce a proportionality coefficient $B$ in the right side of Eq. (5.7) to better reproduce the measured widths. The function obtained by least-square fitting is presented by the red solid line in Fig. 5.9. This model can well reproduce the experimental results.

# Chapter 6

# Conclusion

This study demonstrated that the single-shot NRS can be achieved and the Doppler broadening of neutron resonances can be measured by using a LDNS. The experiments of single-shot NRS was performed at ILE, Osaka Univ., Japan.

The peta-watt laser LFEX was used to shoot a CD (deuterated plastic) foil target as an ion acceleration 'pitcher', and a cylindrical beryllium encased by a high-density polyethylene (HDPE) moderator was used as the neutron source. The resonance peaks in 1∼20 eV region was observed with beamline of 1.8 m, every single laser shot. Three layers resonance absorption sample of Ta, Ag and In with different thickness of 1 mm and 5 mm shown distinguishable differences in neutron signal. This result proved that LDNS is capable for element and content analysis technology. By comparing with calculated neutron signal,the pulse duration of LDNS was estimated to be $\leq$1 $\mu$s in 1∼20 eV energy region, responding to energy resolution of 2∼5%. When using accelerator-driven neutron sources, 10s of metres beamlines are necessary for same energy resolutions. The results are the first experimental demonstration of neutron resonance spectral measurement using LDNS. The results provide experimental supports and foundations for the practical application of LDNS and NRA technologies.

As a further investigation, the temperature dependency of resonances were demonstrated experimentally using the LDNS. The short pulse duration ($\leq$1 $\mu$s) of the epithermal neutrons generated by the miniaturized moderator allows the resonance spectrum to be measured with a 1.8 m beamline to analyze the temperature dependence. We observed the neutron resonance absorption at 4.28 eV for the Ta plate heated up to 620 K. By eliminating the broadening effect caused by the moderator, detector and scattering on the beamline, it was found that the resonance width increases as the square root of the temperature and

this tendency is in agreement with the Bethe model [5]. This result indicates that the temperature of a material can be measured using the NRS obtained with a duration of the single neutron pulse ∼100 ns, which is drastically shorter than the data acquisition time at typical accelerator-based neutron facilities (∼ 1 h).

The low-repetition (2 hours per shot) laser system based on LFEX facility was used in the present experiment to give a proof-of-principle demonstration. However, the repetition rate of measurements can be enhanced by the latest laser systems including ELI-NP facility [98], which delivers 200 J pulses with 0.017 Hz. Pumping laser systems operating at 10−100 Hz [47, 48] will further improve the repetition rate, which indicates that *real-time* isotope-sensitive thermometry at a same frequency of laser measuring the instantaneous increase in the temperature of electronic devices or nuclear fuels becomes possible.

# References


[1] James Chadwick. "The existence of a neutron". In: *Proceedings of the Royal Society of London. Series A, Containing Papers of a Mathematical and Physical Character* 136.830 (1932), pp. 692–708.

[2] Neal Jay Carron. *An introduction to the passage of energetic particles through matter*. CRC Press, 2006.

[3] AM Lane and RG Thomas. "R-matrix theory of nuclear reactions". In: *Reviews of Modern Physics* 30.2 (1958), p. 257.

[4] Gregory Breit and Eugene Wigner. "Capture of slow neutrons". In: *Physical review* 49.7 (1936), p. 519.

[5] Hans Albrecht Bethe. "Nuclear physics B. Nuclear dynamics, theoretical". In: *Reviews of Modern Physics* 9.2 (1937), p. 69.

[6] PH Fowler and AD Taylor. "Temperature imaging using epithermal neutrons". In: *Report of a Workshop on Neutron Resonance Radiography Held at the Los Alamos National Laboratory*. 1987, pp. 46–80.

[7] PH Fowler and AD Taylor. *Rutherford Appleton Laboratory Report*. Tech. rep. RAL-87-056, 1987.

[8] H Hasemi et al. "Quantitative evaluation of nuclide density distribution in a substance by neutron resonance absorption transmission method". In: *Physics Procedia* 60 (2014), pp. 244–253.

[9] Peter Schillebeeckx et al. "Neutron resonance spectroscopy for the characterization of materials and objects". In: *Journal of Instrumentation* 7.03 (2012), p. C03009.

[10] AS Tremsin et al. "Non-contact measurement of partial gas pressure and distribution of elemental composition using energy-resolved neutron imaging". In: *AIP Advances* 7.1 (2017), p. 015315.

[11] AS Tremsin et al. “Spatially resolved remote measurement of temperature by neutron resonance absorption”. In: *Nuclear Instruments and Methods in Physics Research Section A: Accelerators, Spectrometers, Detectors and Associated Equipment* 803 (2015), pp. 15–23.

[12] Takashi Kamiyama et al. “Computer tomography thermometry—an application of neutron resonance absorption spectroscopy”. In: *Nuclear Instruments and Methods in Physics Research Section A: Accelerators, Spectrometers, Detectors and Associated Equipment* 542.1-3 (2005), pp. 258–263.

[13] VW Yuan et al. “Shock temperature measurement using neutron resonance spectroscopy”. In: *Physical review letters* 94.12 (2005), p. 125504.

[14] Niels Bohr. “Neutron capture and nuclear constitution”. In: *Uspekhi Fizicheskikh Nauk* 16.4 (1936), pp. 425–435.

[15] Paul Reuss. *Neutron physics*. 2008.

[16] John RD Copley and Terrence J Udovic. “Neutron time-of-flight spectroscopy”. In: *Journal of research of the National Institute of Standards and Technology* 98.1 (1993), p. 71.

[17] CE Ragan III, MG Silbert, and BC Diven. “Shock compression of molybdenum to 2.0 TPa by means of a nuclear explosion”. In: *Journal of Applied Physics* 48.7 (1977), pp. 2860–2870.

[18] Zechen Lan and Akifumi Yogo. “Exploring nuclear photonics with a laser driven neutron source”. In: *Plasma Physics and Controlled Fusion* 64.2 (2021), p. 024001.

[19] Donna Strickland and Gerard Mourou. “Compression of amplified chirped optical pulses”. In: *Optics communications* 55.6 (1985), pp. 447–449.

[20] Matthew C Asplund, Jeremy A Johnson, and James E Patterson. “The 2018 Nobel Prize in physics: optical tweezers and chirped pulse amplification”. In: *Analytical and bioanalytical chemistry* 411.20 (2019), pp. 5001–5005.

[21] John Nuckolls et al. “Laser compression of matter to super-high densities: Thermonuclear (CTR) applications”. In: *Nature* 239.5368 (1972), pp. 139–142.

[22] EL Clark et al. “Energetic heavy-ion and proton generation from ultraintense laser-plasma interactions with solids”. In: *Physical Review Letters* 85.8 (2000), p. 1654.

[23] Anatoly Maksimchuk et al. “Forward ion acceleration in thin films driven by a high-intensity laser”. In: *Physical Review Letters* 84.18 (2000), p. 4108.

[24] RA Snavely et al. “Intense high-energy proton beams from petawatt-laser irradiation of solids”. In: *Physical review letters* 85.14 (2000), p. 2945.

[25] Akifumi YOGO et al. “Developments of laser neutron source and diagnostics in Japan”. In: *AAPPS-DPP2019, L-I10* (2019).

[26] SR Mirfayzi et al. “Proof-of-principle experiment for laser-driven cold neutron source”. In: *Scientific Reports* 10.1 (2020), pp. 1–8.

[27] KL Lancaster et al. “Characterization of 7 Li (p, n) 7 Be neutron yields from laser produced ion beams for fast neutron radiography”. In: *Physics of plasmas* 11.7 (2004), pp. 3404–3408.

[28] A Yogo et al. “Laser-driven neutron generation realizing single-shot resonance spectroscopy”. In: *Physical Review X* 13.1 (2023), p. 011011.

[29] A Alejo et al. “High flux, beamed neutron sources employing deuteron-rich ion beams from D2O-ice layered targets”. In: *Plasma Physics and Controlled Fusion* 59.6 (2017), p. 064004.

[30] Yasunobu Arikawa et al. “Demonstration of efficient relativistic electron acceleration by surface plasmonics with sequential target processing using high repetition lasers”. In: *Physical Review Research* 5.1 (2023), p. 013062.

[31] M Roth et al. “Bright laser-driven neutron source based on the relativistic transparency of solids”. In: *Physical review letters* 110.4 (2013), p. 044802.

[32] Annika Kleinschmidt et al. “Intense, directed neutron beams from a laser-driven neutron source at PHELIX”. In: *Physics of Plasmas* 25.5 (2018), p. 053101.

[33] DP Higginson et al. “Laser generated neutron source for neutron resonance spectroscopy”. In: *Physics of plasmas* 17.10 (2010), p. 100701.

[34] Seyed Reza Mirfayzi et al. “A miniature thermal neutron source using high power lasers”. In: *Applied Physics Letters* 116.17 (2020), p. 174102.

[35] Marc Zimmer et al. “Demonstration of non-destructive and isotope-sensitive material analysis using a short-pulsed laser-driven epi-thermal neutron source”. In: *Nature Communications* 13.1 (2022), p. 1173.

[36] L Willingale et al. “Comparison of bulk and pitcher-catcher targets for laser-driven neutron production”. In: *Physics of Plasmas* 18.8 (2011), p. 083106.

[37] DP Higginson et al. “Production of neutrons up to 18 MeV in high-intensity, short-pulse laser matter interactions”. In: *Physics of Plasmas* 18.10 (2011), p. 100703.

[38] D Jung et al. “Characterization of a novel, short pulse laser-driven neutron source”. In: *Physics of Plasmas* 20.5 (2013), p. 056706.

[39] Ishay Pomerantz et al. “Ultrashort pulsed neutron source”. In: *Physical review letters* 113.18 (2014), p. 184801.

[40] Satyabrata Kar et al. “Beamed neutron emission driven by laser accelerated light ions”. In: *New Journal of Physics* 18.5 (2016), p. 053002.

[41] MM Günther et al. “Forward-looking insights in laser-generated ultra-intense $\gamma$-ray and neutron sources for nuclear application and science”. In: *Nature Communications* 13.1 (2022), p. 170.

[42] Paul Hill and Yuanbin Wu. “Exploring laser-driven neutron sources for neutron capture cascades and the production of neutron-rich isotopes”. In: *Physical Review C* 103.1 (2021), p. 014602.

[43] Akifumi Yogo et al. “Single shot radiography by a bright source of laser-driven thermal neutrons and x-rays”. In: *Applied Physics Express* 14.10 (2021), p. 106001.

[44] CM Brenner et al. “Laser-driven x-ray and neutron source development for industrial applications of plasma accelerators”. In: *Plasma Physics and Controlled Fusion* 58.1 (2015), p. 014039.

[45] Nevzat Guler et al. “Neutron imaging with the short-pulse laser driven neutron source at the Trident laser facility”. In: *Journal of Applied Physics* 120.15 (2016).

[46] Zechen Lan et al. “Single-shot Laser-Driven Neutron Spectroscopy for Temperature Profiling”. In: *Nature Communications* (2024). to be published.

[47] Martin Divokỳ et al. “150 J DPSSL operating at 1.5 kW level”. In: *Optics Letters* 46.22 (2021), pp. 5771–5773.

[48] Jumpei Ogino et al. “10 J operation of a conductive-cooled Yb: YAG active-mirror amplifier and prospects for 100 Hz operation”. In: *Optics Letters* 46.3 (2021), pp. 621–624.

[49] I Kishon et al. “Laser based neutron spectroscopy”. In: *Nuclear Instruments and Methods in Physics Research Section A: Accelerators, Spectrometers, Detectors and Associated Equipment* 932 (2019), pp. 27–30.

[50] F Mirani et al. “Laser-driven particle acceleration for multipurpose elemental analysis of materials”. In: *Applying Laser-driven Particle Acceleration III: Using Distinctive Energetic Particle and Photon Sources*. Vol. 12583. SPIE. 2023, pp. 7–14.

[51] Atsushi Ogata. “Present and Future of Laser Accelerator 2. Principle of Laser-Plasma Acceleration”. In: *Journal of Plasma and Fusion Research* 81.4 (2005), pp. 245–249.

[52] Andrea Macchi, Marco Borghesi, and Matteo Passoni. “Ion acceleration by superintense laser-plasma interaction”. In: *Reviews of Modern Physics* 85.2 (2013), p. 751.

[53] F Brunel. “Not-so-resonant, resonant absorption”. In: *Physical review letters* 59.1 (1987), p. 52.

[54] WLl Kruer and Kent Estabrook. “J×B heating by very intense laser light”. In: *The Physics of fluids* 28.1 (1985), pp. 430–432.

[55] SC Wilks et al. “Absorption of ultra-intense laser pulses”. In: *Physical review letters* 69.9 (1992), p. 1383.

[56] Paul Bolton, Katia Parodi, and Jörg Schreiber. *Applications of laser-driven particle acceleration*. CRC Press, 2018.

[57] JFL Simmons and CR McInnes. “Was Marx right? or How efficient are laser driven interstellar spacecraft?” In: *American journal of physics* 61.3 (1993), pp. 205–207.

[58] Heinrich Hora. “New aspects for fusion energy using inertial confinement”. In: *Laser and Particle Beams* 25.1 (2007), pp. 37–45.

[59] MM Günther et al. “A novel nuclear pyrometry for the characterization of high-energy bremsstrahlung and electrons produced in relativistic laser-plasma interactions”. In: *Physics of Plasmas* 18.8 (2011), p. 083102.

[60] Yasunobu Arikawa et al. “High-intensity neutron generation via laser-driven photonuclear reaction”. In: *Plasma and Fusion Research* 10 (2015), pp. 2404003–2404003.

[61] JM Yang et al. “Neutron production by fast protons from ultraintense laser-plasma interactions”. In: *Journal of applied physics* 96.11 (2004), pp. 6912–6918.

[62] ST Butler. “On angular distributions from (d, p) and (d, n) nuclear reactions”. In: *Physical Review* 80.6 (1950), p. 1095.

[63] K Ikeda, S Fujii, and JI Funjita. “The (p, n) reactions and beta decays”. In: *Phys. Letters* 3 (1963).

[64] Weston M Stacey. *Nuclear reactor physics*. Vol. 2. Wiley Online Library, 2007.

[65] Ludwik Dobrzynski and Konrad Blinowski. *Neutrons and solid state physics*. Prentice Hall, 1994.

[66] DE Baker. “Graphite as a neutron moderator and reflector material”. In: *Nuclear Engineering and design* 14.3 (1971), pp. 413–444.

[67] M Huerta Parajon, E Abad, and FJ Bermejo. “A review of the cold neutron moderator materials: neutronic performance and radiation effects”. In: *Physics Procedia* 60 (2014), pp. 74–82.

[68] Tatsuhiko Sato et al. “Features of particle and heavy ion transport code system (PHITS) version 3.02”. In: *Journal of Nuclear Science and Technology* 55.6 (2018), pp. 684–690.

[69] H Ohuchi and A Yamadera. “Dependence of fading patterns of photostimulated luminescence from imaging plates on radiation, energy, and image reader”. In: *Nuclear Instruments and Methods in Physics Research Section A: Accelerators, Spectrometers, Detectors and Associated Equipment* 490.3 (2002), pp. 573–582.

[70] DO Golovin et al. “Calibration of imaging plates sensitivity to high energy photons and ions for laser-plasma interaction sources”. In: *Journal of Instrumentation* 16.02 (2021), T02005.

[71] Y Abe et al. “Characterizing a fast-response, low-afterglow liquid scintillator for neutron time-of-flight diagnostics in fast ignition experiments”. In: *Review of Scientific Instruments* 85.11 (2014), 11E126.

[72] FWK Firk, GG Slaughter, and RJ Ginther. "An improved Li6-loaded glass scintillator for neutron detection". In: *Nuclear Instruments and Methods* 13 (1961), pp. 313–316.

[73] CWE Van Eijk, Aurélie Bessière, and P Dorenbos. "Inorganic thermal-neutron scintillators". In: *Nuclear Instruments and Methods in Physics Research Section A: Accelerators, Spectrometers, Detectors and Associated Equipment* 529.1-3 (2004), pp. 260–267.

[74] Irish Valerie B Maggay, Pin-Chun Lin, and Wei-Ren Liu. "Investigation of luminescence properties and the energy transfer mechanism of Li 6 Lu (BO 3) 3: Ce 3+, Tb 3+ green-emitting phosphors". In: *RSC Advances* 5.8 (2015), pp. 5591–5597.

[75] Sei-ichi Komoda and Sin-iti Igarasi. "Neutron cross sections of Li-6". In: *Journal of Nuclear Science and Technology* 15.1 (1978), pp. 79–81.

[76] Keiichi Shibata et al. "JENDL-4.0: a new library for nuclear science and engineering". In: *Journal of Nuclear Science and Technology* 48.1 (2011), pp. 1–30.

[77] KK Hamamatsu Photonics. "Photomultiplier tubes: Basics and applications". In: *Edition 3a* 310 (2007).

[78] Raffaele Bencardino and John E Eberhardt. "Development of a fast-neutron detector with silicon photomultiplier readout". In: *IEEE Transactions on Nuclear Science* 56.3 (2009), pp. 1129–1134.

[79] C Roecker et al. "Design of a transportable high efficiency fast neutron spectrometer". In: *Nuclear Instruments and Methods in Physics Research Section A: Accelerators, Spectrometers, Detectors and Associated Equipment* 826 (2016), pp. 21–30.

[80] Y Abe et al. "A multichannel gated neutron detector with reduced afterpulse for low-yield neutron measurements in intense hard X-ray backgrounds". In: *Review of Scientific Instruments* 89.10 (2018), p. 10I114.

[81] RG Bennett and RP Schwenker. "Performance of a Pulsed 6292 Photomultiplier". In: *Review of Scientific Instruments* 30.9 (1959), pp. 836–837.

[82] Francesco De Martini and Kenneth P Wacks. "Photomultiplier Gate for Stimulated-Spontaneous Light Scattering Discrimination". In: *Review of Scientific Instruments* 38.7 (1967), pp. 866–868.

[83] F De Marco and E Penco. “Pulsed photomultipliers”. In: *Review of Scientific Instruments* 40.9 (1969), pp. 1158–1160.

[84] M Bruce Schulman. “Gating circuit for linear-focused photomultiplier”. In: *Review of scientific instruments* 60.7 (1989), pp. 1264–1266.

[85] Zechen Lan et al. “Development of a Time-Gated Epithermal Neutron Spectrometer for Resonance Absorption Measurements Driven by a High-Intensity Laser”. In: *Quantum Beam Science* 8.1 (2024), p. 9.

[86] Seungeun Lee et al. “Performance of a new accelerating-electrode-equipped fast-time-response PMT coupled with fast LGSO”. In: *Physics in Medicine & Biology* 63.5 (2018), 05NT03.

[87] Michael P Bristow, Donald H Bundy, and Anthony G Wright. “Signal linearity, gain stability, and gating in photomultipliers: application to differential absorption lidars”. In: *Applied optics* 34.21 (1995), pp. 4437–4452.

[88] Glenn C Tyrrell. “Phosphors and scintillators in radiation imaging detectors”. In: *Nuclear Instruments and Methods in Physics Research Section A: Accelerators, Spectrometers, Detectors and Associated Equipment* 546.1-2 (2005), pp. 180–187.

[89] Noriaki Kawaguchi et al. “Neutron responses of Eu 2+ activated LiCaAlF 6 scintillator”. In: *2008 IEEE Nuclear Science Symposium Conference Record*. IEEE. 2008, pp. 1174–1176.

[90] Tohru Ebisawa et al. “Neutron reflectivities of Ni-Mn and Ni-Ti multilayers for monochromators and supermirrors”. In: *Journal of Nuclear Science and Technology* 16.9 (1979), pp. 647–659.

[91] M Hino et al. “Recent development of multilayer neutron mirror at KURRI”. In: *Nuclear Instruments and Methods in Physics Research Section A: Accelerators, Spectrometers, Detectors and Associated Equipment* 529.1-3 (2004), pp. 54–58.

[92] Fredrik Eriksson et al. “Morphology control in Ni/Ti multilayer neutron mirrors by ion-assisted interface engineering and B 4 C incorporation”. In: *Optical Materials Express* 13.5 (2023), pp. 1424–1439.

[93] EJ Maunders. “Effective cadmium cut-off energies in cycindrical geometry for fissile and 1V detectors”. In: *Journal of Nuclear Energy. Parts A/B. Reactor Science and Technology* 19.12 (1965), pp. 959–969.

[94] MR Hawkesworth. "Neutron radiography. Equipment and methods". In: *Atomic Energy Review* 15.2 (1977), pp. 169–220.

[95] AS Tremsin et al. "Non-destructive studies of fuel pellets by neutron resonance absorption radiography and thermal neutron radiography". In: *Journal of Nuclear Materials* 440.1-3 (2013), pp. 633–646.

[96] Michihiro Furusaka et al. "Activity of Hokkaido University neutron source, HUNS". In: *Physics Procedia* 60 (2014), pp. 167–174.

[97] AS Tremsin et al. "Neutron resonance transmission spectroscopy with high spatial and energy resolution at the J-PARC pulsed neutron source". In: *Nuclear Instruments and Methods in Physics Research Section A: Accelerators, Spectrometers, Detectors and Associated Equipment* 746 (2014), pp. 47–58.

[98] KA Tanaka et al. "Current status and highlights of the ELI-NP research program". In: *Matter and Radiation at Extremes* 5.2 (2020).

[99] Jumpei Ogino et al. "10-J, 100-Hz conduction-cooled active-mirror laser". In: *Optics Continuum* 1.5 (2022), pp. 1270–1277.

[100] N Miyanaga et al. "10-kJ PW laser for the FIREX-I program". In: *Journal de Physique IV (Proceedings)*. Vol. 133. EDP sciences. 2006, pp. 81–87.

[101] A Yogo et al. "Boosting laser-ion acceleration with multi-picosecond pulses". In: *Scientific reports* 7.1 (2017), p. 42451.

[102] SR Mirfayzi et al. "Calibration of time of flight detectors using laser-driven neutron source". In: *Review of Scientific Instruments* 86.7 (2015).

[103] SR Mirfayzi et al. "Ultra-short, beamed source of laser-driven epithermal neutrons". In: *Applied Physics Letters* (2019).

[104] SR Mirfayzi et al. "Experimental demonstration of a compact epithermal neutron source based on a high power laser". In: *Applied Physics Letters* 111.4 (2017), p. 044101.

[105] Enrico Perelli Cippo et al. "Imaging of cultural heritage objects using neutron resonances". In: *Journal of analytical atomic spectrometry* 26.5 (2011), pp. 992–999.

# *Accomplishments*

**Papers**

1 Zechen Lan, Yasunobu Arikawa, S. Reza Mirfayzi, Alessio Morace, Takehito Hayakawa, Hirotaka Sato, Takashi Kamiyama, Tianyun Wei, Yuta Tatsumi, Mitsuo Koizumi, Yuki Abe, Shinsuke Fujioka, Kunioki Mima, Ryosuke Kodama and Akifumi Yogo, et al, Single-shot laser-driven neutron resonance spectroscopy for temperature profiling, accepted for publication in *Nature Communications*, 23 May 2024.

2 Zechen Lan, Yasunobu Arikawa, Yuki Abe, S. Reza Mirfayzi, Alessio Morace, Takehito Hayakawa, Tianyun Wei and Akifumi Yogo, Development of a time-gated epi-thermal neutron spectrometer for resonance absorption measurements driven by a high-intensity laser, *Quantum Beam Science*, 2024, **8**(1): 9.

3 Zechen Lan and Akifumi Yogo, Exploring nuclear photonics with laser driven neutron source, *Plasma Physics and Controlled Fusion* **64** 024001 (2022).

4 Akifumi Yogo, Zechen Lan, Yasunobu Arikawa, Yuki Abe, S. Reza Mirfayzi, Tianyun Wei, Takato Mori, Daniil O. Golovin, Takahito Hayakawa, Natsumi Iwata, Shinsuke Fujioka, Mitsuo Nakai, Yasuhiko Sentoku, Kunioki Mima, Masakatsu Murakami, Mitsuo Koizumi, Fumiaki Ito, Jaehong Lee, Tohn Takahashi, Kota Hironaka, Satyabrata Kar, Hiroaki Nishimura, and Ryosuke Kodama, Laser-Driven Neutron Generation Realizing Single-Shot Resonance Spectroscopy, *Physical Review X* **13** 011011 (2023).

5 Yuki Abe, Ayami Nakao, Yasunobu Arikawa, Alessio Morace, Takato Mori, Zechen Lan, Tianyun Wei, Shoui Asano, Takumi Minami, Yasuhiro Kuramitsu, Hideaki Habara, Hiroyuki Shiraga, Shinsuke Fujioka, Mitsuo Nakai, Akifumi Yogo, Predictive capability of material screening by fast neutron activation analysis using laser-driven neutron sources, *Review of Scientific Instruments* **93**(9) (2022).

6 Takato Mori, Akifumi Yogo, Takehito Hayakawa, S. Reza Mirfayzi, Zechen Lan, Tianyun Wei, Yuki Abe, Yasunobu Arikawa, Mitsuo Nakai,

Kunioki Mima, Hiroaki Nishimura, Shinsuke Fujioka and Ryosuke Kodama, Thermal neutron fluence measurement using a cadmium differential method at the laser-driven neutron source, *Journal of Physics G Nuclear and Particle Physics* **49**(6):065103 (2022).

7 Tianyun Wei, Akifumi Yogo, Takehito Hayakawa, Yasunobu Arikawa, Yuki Abe, Maiko Nakanishi, S. Reza Mirfayzi, Zechen Lan, Takato Mori, Kunioki Mima, Shinsuke Fujioka, Masakatsu Murakami, Mitsuo Nakai, Hiroaki Nishimura, Satyabrata Kar and Ryosuke Kodama, Non-destructive inspection of water or high-pressure hydrogen gas in metal pipes by the flash of neutrons and x rays generated by laser, *AIP Advances* **12**(4):045220 (2022).

8 Kunioki Mima, Akifumi Yogo, S. Reza Mirfayzi, Zechen Lan, Yasunobu Arikawa, Yuki Abe and Hiroaki Nishimura, Laser-driven neutron source and nuclear resonance absorption imaging at ILE, Osaka University: Review, *Applied Optics* **61**(9):2398-2405 (2022).

9 Akifumi Yogo, S. Reza Mirfayzi, Yasunobu Arikawa, Yuki Abe, Tianyun Wei, Takato Mori, Zechen Lan, Yuki Hoonoki, Daniil O. Golovin and Keisuke Koga, Single shot radiography by a bright source of laser-driven thermal neutrons and x-rays, *Applied Physics Express* **14**(10):106001 (2021).

10 Takato Mori, Akifumi Yogo, Takehito Hayakawa, S. Reza Mirfayzi, Zechen Lan, Yuki Abe, Yasunobu Arikawa, Daniil O. Golovin, Tianyun Wei, Yuki Hoonoki, Mitsuo Nakai, Kunioki Mima, Hiroaki Nishimura, Shinsuke Fujioka and Ryosuke Kodama, Direct evaluation of high neutron density environment using (n, 2n) reaction induced by laser-driven neutron source, *Physical Review C* **104**(1):015808 (2021).

11 Daniil O. Golovin, S. Reza Mirfayzi, Satoru Shokita, Yuki Abe, Zechen Lan, Yasunobu Arikawa, Alessio Morace, Tatiana Pikuz and Akifumi Yogo, Calibration of imaging plates sensitivity to high energy photons and ions for laser-plasma interaction sources, *Journal of Instrumentation* **16**(02):T02005-T02005 (2021).

12 S. Reza Mirfayzi, Akifumi Yogo, Zechen Lan, Takashi Ishimoto, Akifumi Iwamoto, Mitsuho Nagata, Yasunobu Arikawa, Yuki Abe, Daniil O. Golovin, Yuki Hoonoki, Takato Mori, Kazuki Okamoto, Satoru Shokita, Dave Neely, Shinsuke Fujioka, Kunioki Mima, Hiroaki Nishimura,

Satyabrata Kar and Ryosuke Kodama, Proof-of-principle experiment for laser-driven cold neutron source, *Scientific Reports* **10**:20157 (2020).

13 Satoru Shokita, Akifumi Yogo,S. Reza Mirfayzi, Yuki Hoonoki, Daniil O. Golovin, Takashi Ishimoto, Zechen Lan, Kazuki Matsuo, Takato Mori, Kazuki Okamoto, Hideo Nagatomo, Hiroaki Nishimura, Yasuhiko Sentoku, Kohei Yamanoi and Ryosuke Kodama, Observation of MeV-energy ions from the interaction of over picosecond laser pulses with near-critical density foam targets, *High Energy Density Physics* **36**(2-3):100821 (2020).

**Conferences**

1 Zechen Lan, Yasunobu Arikawa, S. Reza Mirfayzi, et al, シングルショット共鳴分光を実現するレーザー駆動中性子源, レーザー学会学術講演会第 *44* 回年次大会 (2024), 招待講演 **C07-19p-VII-01**.

2 Zechen Lan, Tianyun Wei, Takehito Hayakawa, et al, Neutron resonance spectroscopy using a single pulse of laser-driven neutrons, *7th Asia-Pacific Conference on Plasma Physics* (2023), invited presentation **L-7-I4**.

3 Zechen Lan, Tianyun Wei, Takehito Hayakawa, et al, Nuclear Thermometer using Single Pulse of Laser-driven Neutron Source, *Nuclear Photonics 2023*, poster section.

4 Zechen Lan, Akifumi Yogo, Takehito Hayakawa, et al, High-speed Atomic Thermometer using Single-shot of Laser-driven Neutron Pulse, 日本物理学会 *2023* 年春季大会 (2023) **25aB1-12**, 優秀論文発表賞.

5 Zechen Lan, Akifumi Yogo, Takehito Hayakawa, et al, High-speed Atomic Thermometer using Single-shot of Laser-driven Neutron Pulse, レーザー学会学術講演会第 *43* 回年次大会 (2023) **C06-20a-V-03**, 優秀論文発表賞.

6 Zechen Lan, Akifumi Yogo, S. Reza Mirfayzi, et al, The Development of Laser-Driven Epithermal Neutron Source for Resonance Spectral Diagnostics II, 日本物理学会第 *78* 回年次大会 (2022) **13aB1-11**.

7 Zechen Lan, Akifumi Yogo, S. Reza Mirfayzi, et al, Experimental Demonstration of Neutron Resonance Measurement using Laser-Driven Neutron Source, *Nuclear Photonics* 2021.

8 Zechen Lan, Akifumi Yogo, S. Reza Mirfayzi, et al, レーザー駆動熱外中性子源による中性子共鳴吸収計測, 日本物理学会第 *76* 回年次大会 (2021) **3aB1-11**.

9 Zechen Lan, Akifumi Yogo, S. Reza Mirfayzi, et al, Laser-driven epithermal neutron source for neutron resonance diagnosis, レーザー学会学術講演会第 *41* 回年次大会 (2021) **C02-18a-III-03**, 優秀論文発表賞.

10 Zechen Lan, S. Reza Mirfayzi, Akifumi Yogo, et al, Development of cryogenic-cooled solid hydrogen moderator for laser-driven cold neutron generation, 日本物理学会第 *75* 回年次大会 (2020).

**Awards**

1 日本物理学会 2023 年春季大会優秀論文発表賞.

2 レーザー学会学術講演会第 43 回年次大会 (2023) 優秀論文発表賞.

3 レーザー学会学術講演会第 41 回年次大会 (2021) 優秀論文発表賞.

**Competitive funds**

1 2023 年度日本学術振興会特別研究員 DC2.

2 令和 4 年度 (2022) 大阪大学次世代挑戦的研究者育成プロジェクトに採用.